Forschungszentrum Karlsruhe
in der Helmholtz-Gemeinschaft

Wissenschaftliche Berichte
FZKA 7018

Countercurrent Flow Limitations in Horizontal Stratified Flows of Air and Water

M. Gargallo Gallego

Institut für Kern- und Energietechnik
Programm Nukleare Sicherheitsforschung

September 2004

Forschungszentrum Karlsruhe

in der Helmholtz-Gemeinschaft

Wissenschaftliche Berichte

FZKA 7018

Countercurrent Flow Limitations in Horizontal Stratified Flows of Air and Water

Mireia Gargallo Gallego

Institut für Kern- und Energietechnik

Programm Nukleare Sicherheitsforschung

Von der Fakultät für Maschinenbau der Universität Stuttgart
genehmigte Dissertation (D93)

Forschungszentrum Karlsruhe GmbH, Karlsruhe

2004

Impressum der Print-Ausgabe:

Als Manuskript gedruckt

Forschungszentrum Karlsruhe GmbH
Postfach 3640, 76021 Karlsruhe

Mitglied der Hermann von Helmholtz-Gemeinschaft
Deutscher Forschungszentren (HGF)

ISSN 0947-8620

urn:nbn:de:0005-070184

Countercurrent Flow Limitations in Horizontal Stratified Flows of Air and Water

A dissertation accepted by the Faculty of Mechanical Engineering (University of Stuttgart) for the award of the academic degree of "Doctor of Engineering (Dr.-Ing.)"

Performed by

Dipl.-Ing. Mireia Gargallo Gallego

from Barcelona (Spain)

Referent:	Prof. Dr. -Ing. habil. E. Laurien Faculty of Mechanical Engineering, Chair of Thermofluid Dynamics, University of Stuttgart
Co-Referent:	Prof. Dr. -Ing. T. Schulenberg Institute for Nuclear and Energy Technologies, Forschungszentrum Karlsruhe GmbH
	Exam: 8.12.2003

Fakultät für Maschinenbau, Universität Stuttgart, D93
Institut für Kernenergetik und Energiesysteme (IKE)
Abteilung Thermofluiddynamik (TFD)
Forschungszentrum Karlsruhe GmbH, Karlsruhe
Institut für Kern- und Energietechnik

2004

Abstract

During a postulated Loss-Of-Coolant-Accident (LOCA) in a Pressurized Water Reactor (PWR) it is of vital importance that the reactor core remains properly cooled. The Emergency Core Cooling System (ECCS) in German PWRs compensates the loss of coolant with injection of additional coolant into the cold legs as well as into the hot legs. While the coolant is injected in the cold legs through nozzles, the hot leg injection is performed by means of a secondary pipe placed at the bottom of the pipe of the primary circuit. The subject of this thesis concerns the latter case.

The liquid injected into the hot leg flows directly into the core from its upper part and constitutes a rapid delivery of coolant into the reactor core at high mass flow rate. However, saturated steam is generated in the reactor core due to depressurization of the primary system and flows out of the Reactor Pressure Vessel (RPV) into the hot leg. Therefore, a countercurrent stratified flow of injected coolant and saturated steam occurs along one and a half meter inside the hot leg before the coolant reaches the RPV. This horizontal stratified countercurrent flow of coolant and steam is only stable for a certain range of coolant and steam mass flow rates. Even if the coolant is injected at very high velocities and high Froude numbers, there is always a threshold steam velocity above which the cooling of the reactor core can be reduced or complete interrupted. This phenomenon is known in two-phase flow science as Countercurrent Flow Limitation (CCFL), since there is a limitation of liquid delivery due to the presence of a gas phase flowing countercurrently to the liquid phase.

CCFL in reflux condensation cooling was more investigated than in ECC in the hot leg. For this purpose, the test facility WENKA was built at Forschungszentrum Karlsruhe GmbH (Germany) to investigate for which flow conditions CCFL poses a safety risk during hot leg injection and to provide experimental data to support the analysis of such an accident scenario with CFD - Codes.

The WENKA test facility models a simplified PWR hot leg geometry including the secondary pipeline placed at the bottom of the main coolant line. The countercurrent flow of coolant and saturated steam during injection by means of the ECCS was investigated with air and water in a rectangular test section. The fluid dynamics of the injection process was reproduced for a wide range of flow conditions to identify flow regimes and to derive 1-dimensional models to predict the limits of coolant delivery. On the other hand, a data base of local flow parameters was established to enhance CFD - Codes performance. Experimental local velocities of the liquid film were obtained by means of Particle Image Velocimetry and the liquid film morphology was analyzed depending on the flow regimes.

Flow regime maps were obtained for inlet liquid depths ranging from 3 to 15 mm. Depending on the superficial velocities of liquid and gas and on the Froude number of the liquid film, a stratified countercurrent flow, a partially reversed flow or a totally reversed flow were experimentally observed. The CCFL occurred as a breakdown of the stable countercurrent stratified two-phase flow: The liquid begun to be carried over by the gas and to flow partially or totally in the air flow direction. The new flow regime that set in the hot leg and caused the CCFL was defined as *reversed flow*, because the coolant flowed “reversely”. It was distinguished between *partially reversed flow* and *totally reversed flow*, depending on whether only a fraction of the liquid flowed in the air flow direction or the entire injected liquid did. Experimental observations showed also that a subcritical flow, i.e. a liquid film with Froude numbers less than one, is a necessary condition for the onset of flow reversal. Flow reversal with an initially supercritical flow, i.e. a Froude number of the liquid film greater than one, was only obtained if there was a transition from supercritical to subcritical flow, which did not occur continuously, but in the form of a hydraulic jump in the channel. Therefore, some experiments were focused to study the occurrence of a hydraulic jump with countercurrent flow of

air, and to investigate the influence of the initial water height. A theoretical approach for the onset of a hydraulic jump was derived and experimental data were obtained and compared with the theory.

A new theoretical model to predict CCFL was proposed. This novel criterion predicts the occurrence of reversed flow in the hot leg and is based on the well known Wallis correlation. The Wallis correlation assesses that the occurrence of reversed flow coincides with the flow conditions, for which the sum of the squared root of the dimensionless superficial velocities of liquid and gas is equal to a constant value *C*. However, a supercritical liquid flow was reversed in the test facility for greater values of *C.* There, flow reversal coincided with the transition from supercritical to subcritical flow. Discrepancies with the values predicted by Wallis are due to the fact, that the Wallis correlation neglected the inertia of the fluids. The new theoretical model includes the inertial term and presents two criteria that are fulfilled at onset reversed flow. The first is a criterion to predict the transition to subcritical flow. This criterion was developed analytically and includes the influence of the Froude number of the liquid at the injection point, the channel length, the inlet liquid depth, the liquid Reynolds number and the slip velocity ratio between gas and liquid. The second criterion is based on experimental observations and postulates that reversed flow occurs always a values of *C* larger than 0.7. The new model predicted with good accuracy the occurrence of reversed flow in the WENKA test facility.

And last but not least, liquid delivery rates were measured for a wide range of conditions and an empirical correlation to predict back flow ratios was presented.

Gegenstrombegrenzung in horizontalen geschichteten Strömungen von Luft und Wasser

Kurzfassung

Diese Arbeit beschäftigt sich mit Schichtenströmungen, die bei schweren Unfällen in Leichtwasserreaktoren auftreten können. Diese Form der zweiphasigen Strömung ist auch in vielen anderen industriellen Anwendungen zu finden.

Beim Bruch einer Hauptkühlmittelleitung eines Druckwasserreaktors (in der englischen Literatur als „Loss of Coolant Accident“ bezeichnet) übernimmt das Noteinspeisungssystem die Aufgabe, unterkühltes Wasser in den Reaktordruckbehälter einzuspeisen. In deutschen Reaktoren wird Kühlmittel sowohl in den kalten als auch in den heißen Teil des Kühlkreislaufs eingepumpt. Die Einspeisung von Wasser in den heißen Teil des Hauptkühlkreislaufs erfolgt durch eine sekundäre Rohrleitung, die im Hauptkühlkreislauf eingebaut ist. Bis zum Reaktordruckbehälter muss das eingespeiste Wasser ca. 1.5 m im Primärkreislaufsrohr strömen. Aufgrund der Druckentlastung, die automatisch während eines Unfalls durchgeführt wird, bildet sich im Reaktordruckbehälter gesättigter Dampf. Dieser Dampf strömt entgegen dem vom Noteinspeisungssystem injizierten Wasser im Primärkreislauf.

In Abhängigkeit vom Kühlmittel- und Dampfmassendurchsatz finden verschiedene Strömungsphänomene im heißen Teil des Primärkreises statt: Strömungsinstabilitäten wie ein hydraulischer Sprung oder Strömungsumkehr wurden in vielen auf diesem Gebiet durchgeführten Arbeiten experimentell beobachtet und wurden als Strömungsphänomene erkannt, die den Noteinspeisungsablauf bestimmen.

Zweifellos ist die Notkühlung des Reaktors durch den heißen Strang des Primärkreislaufs wegen des möglichen Auftretens einer Strömungsumkehr begrenzt: für genügend hohe Dampfgeschwindigkeit wird ein Teil des eingespeisten Wassers von der Dampfströmung mitgerissen. Eine Strömungsumkehr bedeutet, dass der Reaktorkern möglicherweise nicht weiter geflutet und gekühlt werden kann, da nur ein reduzierter Teil des Kühlmittels den Reaktorkern erreicht. Darüber hinaus, kann das Auftreten einer Strömungsumkehr zu dem sogenannten *Null-Durchschuss-Zustand* führen, für den das gesamte eingespeiste Kühlmittel vom Dampf transportiert wird. Die gegengerichtete Schichtenströmung von Dampf und Kühlmittel ist nicht mehr möglich wegen des Phänomens der Strömungsbegrenzung, das das Einströmen des Kühlmittels in den Reaktordruckbehälter verhindert.

Die WENKA – Anlage (Wasser und Entrainment Kanal) im Forschungszentrum Karlsruhe wurde konzipiert, um solche Strömungsphänomene zu untersuchen. Der Versuchstand modelliert durch einen rechteckigen Kanal den Reaktordruckbehälter und eine der Hauptkühlmittelleitungen, die zum Dampferzeuger führt. Die Krümmung am Dampferzeuger wird nicht modelliert. Die Einspeisung von Kühlmittel wird mittels einer Wasserströmung unter dem Effekt einer gegengerichteten Luftströmung, die das Ausblasen von Dampf aus dem Reaktorkern darstellt, modelliert.

Je nach Geschwindigkeitsverhältnis werden verschiedene Strömungsformen im Kanal beobachtet:

- *Gegengerichtete Schichtenströmung mit überkritischem Wasserfilm:* Das Wasser wird überkritisch eingespeist, d.h. die Froude – Zahl im gesamten Kanal ist höher als eins. Trägheitskräfte sind dominant. Die Phasengrenze ist relativ glatt und die Filmhöhe ist kleiner als die kritische Filmhöhe, y_C (Filmhöhe für die die Froude – Zahl gleich eins ist). Der Wasserpegel nimmt in Wasserströmungsrichtung progressiv zu. In einer überkritischen Strömung können sich keine Wellen stromaufwärts fortpflanzen.

- *Gegengerichtete Schichtenströmung mit unterkritischem Wasserfilm:* Das Wasser wird unterkritisch eingespeist, d.h. die Froude – Zahl im gesamten Kanal ist kleiner als eins. Die Schwerkraft ist in dieser Art Strömung dominant. Die Phasengrenze ist wellig und die Filmhöhe ist größer als die kritische Filmhöhe. Der Wasserpegel nimmt in Wasserströmungsrichtung progressiv ab. In einer unterkritischen Strömung können sich Wellen stromaufwärts fortpflanzen.

- *Gegengerichtete Schichtenströmung mit einem hydraulischen Sprung:* Das Wasser wird überkritisch eingespeist, aber ein Übergang zur unterkritischen Strömung findet im Kanal in Form einer sprunghaften Änderung des Wasserpegels statt. Ist die Strömung überkritisch im gesamten Kanal, findet der hydraulische Sprung immer am Ende des Kanals statt, sobald die kritische Höhe, $y_{A,C}$ dort erreicht wird.

- *Partielle Strömungsumkehr:* Die Luftgeschwindigkeit ist hoch genug, um eine Strömungsumkehr hervorzurufen. Eine Instabilität bildet sich am Ende des Kanals und nimmt die Form eines hydraulischen Sprungs an, der sich stromaufwärts plötzlich verbreitet. Die Phasengrenze wird gestört und wellig.

- *Totale Strömungsumkehr:* Das ganze Wasser strömt in Richtung der Luftströmung. Für ausreichende hohe Geschwindigkeiten wird Schwallströmung („slug flow“ in der englischen Literatur) mit Wellen mit langen Amplituden beobachtet. Ab diesem Zeitpunkt kann der Wasserdurchsatz erhöht werden, trotzdem strömt aber kein Wasser bis zum Ende des Kanals wegen der Strömungsbegrenzung.

Die Strömungsformen, die in der Anlage stattfinden, wurden in Abhängigkeit der Leerrohrgeschwindigkeiten von der Flüssigkeit und vom Gas in Form von Strömungskarten dokumentiert. Es wurde experimentell beobachtet, dass der Übergang von überkritischer Strömung zur Strömungsumkehr mit dem Auftreten eines hydraulischen Sprungs am Ende des Kanals übereinstimmt. Aus diesem Grund wurde ein theoretischer Ansatz zur Bestimmung des Fließwechsels zwischen überkritischer und unterkritischer Strömung abgeleitet. Dieses Modell beruht auf der Momentumsgleichung eines Wasserfilms mit Gegenstrom von Luft in einem Kanal. Das Auftreten eines hydraulischen Sprungs am Ende des Kanals kann in Abhängigkeit der Kanallänge, der Reynoldszahl der Flüssigkeit, des Schlupfs zwischen Luft und Wasser ($s = u_G / u_L$), der Dichten der Luft und des Wassers und der Froude- Zahl am Eintritt des Kanals (gebildet mit dem Wasserpegel am Eintritt) beschrieben werden. Ein Vergleich mit experimentellen Daten zeigt eine gute Übereinstimmung.

Da ein hydraulischer Sprung auch ohne Strömungsumkehr im Kanal beobachtet wurde, muss es eine zweite Bedingung geben, die beim Auftreten von der Strömungsumkehr erfüllt werden muss. In der Literatur vorhandene Korrelationen zur Bestimmung der Strömungsumkehr wurden untersucht. Fast alle Korrelationen sind Modifikationen der Wallis Korrelation. Die Wallis Korrelation sagt eine Strömungsumkehr vorher, wenn die Summe der Wurzel der dimensionslosen Leerrohrgeschwindigkeiten vom Gas und von der Flüssigkeit gleich einer Konstante C (die sogenannte *Wallis Konstante*) ist.

In der WENKA – Anlage wurde für verschiedene Wassereinlaufshöhen experimentell beobachtet, dass die Strömungsumkehr erst für Werte von $C = 0.7$ stattfindet. Für das Auftreten von Strömungsumkehr müssen damit zwei Kriterien erfüllt werden: Die Flüssigkeit muss unterkritisch fließen und die Wallis Konstante muss gleich oder höher als 0.7 sein.

Die Wasserlieferraten nehmen sprunghaft ab, sobald die Strömungsumkehr auftritt. Eine empirische Korrelation, die sowohl den Einfluss der Froude – Zahl als auch der Leerrohrgeschwindigkeit der Luft berücksichtigt, wurde zur Abschätzung der Wasserlieferraten vorgeschlagen.

Gegenstrombegrenzung in horizontalen geschichteten Strömungen von Luft und Wasser

Zusammenfassung

Einleitung

Unter Schichtenströmung versteht man eine horizontale oder leicht geneigte zweiphasige Strömung, z.B. aus Flüssigkeit und Gas, bei der die Flüssigkeit (bzw. die Phase mit der höheren Dichte) in Form eines Films strömt. Die Wechselwirkungen zwischen beiden Phasen (Masse-, Moment- und Energieaustausch) finden durch die Phasengrenze zwischen Gas und Flüssigkeit statt und sind stark von den relativen Geschwindigkeiten der Phasen abhängig.

Diese Arbeit beschäftigt sich mit Schichtenströmungen die bei schweren Unfällen in Leichtwasserreaktoren auftreten, obwohl diese Form der zweiphasigen Strömung in vielen anderen industriellen Anwendungen zu finden ist.

Beim Bruch einer Hauptkühlmittelleitung eines Druckwasserreaktors (in der englischen Literatur als „Loss of Coolant Accident“ bezeichnet) übernimmt das Noteinspeisungssystem die Aufgabe, unterkühltes Wasser in den Reaktordruckbehälter einzuspeisen. In deutschen Reaktoren wird Kühlmittel sowohl in den kalten als auch in den heißen Teil des Kühlkreislaufs eingepumpt. Die Einspeisung von Wasser in den heißen Teil des Hauptkühlkreislaufs erfolgt durch eine sekundäre Rohrleitung, die im Hauptkühlkreislauf eingebaut ist (Siehe **Abbildung 1**). Bis zum Reaktordruckbehälter muss das eingespeiste Wasser ca. 1.5 m im Primärkreislaufsrohr strömen. Aufgrund der Druckentlastung, die automatisch während eines Unfalls durchgeführt wird, bildet sich im Reaktordruckbehälter gesättigter Dampf. Dieser Dampf strömt entgegen dem vom Noteinspeisungssystem injizierten Wasser im Primärkreislauf.

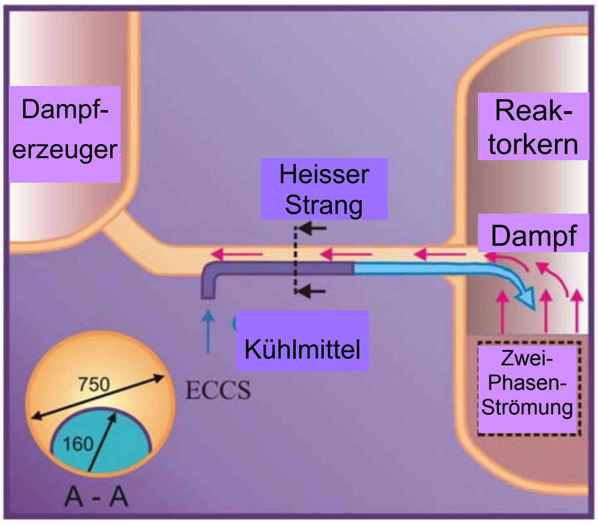

Abbildung 1. Noteinspeisung von Kühlmittel über den heißen Strang.

In Abhängigkeit vom Kühlmittel- und Dampfmassendurchsatz finden verschiedene Strömungsphänomene im heißen Teil des Primärkreises statt: Strömungsinstabilitäten wie ein hydraulischer Sprung oder Strömungsumkehr wurden in vielen auf diesem Gebiet durchgeführten Arbeiten experimentell beobachtet und wurden als Strömungsphänomene erkannt, die den Noteinspeisungsablauf bestimmen.

Zweifellos ist die Notkühlung des Reaktors durch den heißen Strang des Primärkreislaufs wegen des möglichen Auftretens einer Strömungsumkehr begrenzt: für genügend hohe Dampfgeschwindigkeit wird ein Teil des eingespeisten Wassers von der Dampfströmung mitgerissen. Eine Strömungsumkehr bedeutet, dass der Reaktorkern möglicherweise nicht weiter geflutet und gekühlt werden kann, da nur ein reduzierter Teil des Kühlmittels den Reaktorkern erreicht. Darüber hinaus, kann das Auftreten einer Strömungsumkehr zu dem sogenannten *Null-Durchschuss-Zustand* führen, für den das gesamte eingespeiste Kühlmittel vom Dampf transportiert wird. Die gegengerichtete Schichtenströmung von Dampf und Kühlmittel ist nicht mehr möglich wegen des Phänomens der Strömungsbegrenzung, das das Einströmen des Kühlmittels in den Reaktordruckbehälter verhindert.

Das Verhalten des Noteinspeisungssystems bei einem Kühlmittelverlustunfall war eines der wichtigsten Forschungsgebiete für Leichtwasserreaktoren in den letzten Jahren. Trotzdem wurde dem Problem der Noteinspeisung durch den heißen Strang weniger Aufmerksamkeit gewidmet. Die Details der Strömungsphänomene, die bei dieser Variante der Noteinspeisung stattfinden können, sind nicht bekannt. Die Berechnung aller dieser Vorgänge mit numerischen Verfahren (CFD - Codes) ist heutzutage immer noch sehr eingeschränkt; teilweise, weil lokale experimentelle Werte relevanter Parameter in der Literatur kaum zu finden sind.

Aus diesem Grund wurde die WENKA - Anlage im Forschungszentrum Karlsruhe gebaut. Ziel der WENKA - Anlage ist es, eine Datenbank für Schichtenströmungen zu erstellen, in der die Strömungsformen und lokalen Werte der Geschwindigkeiten und der Phasengrenze für einen breiten Bereich von Strömungsbedingungen dokumentiert werden. Im rechteckigen Kanal der Anlage können gegengerichtete Strömungen („countercurrent flow“) mit Wasser und Luft untersucht werden. Die Strömungsbedingungen, für die Strömungsumkehr stattfindet, werden untersucht. Die von der Anlage gelieferten experimentellen Daten werden mit analytischen Korrelationen zur Bestimmung des Auftretens der Strömungsumkehr verglichen.

Versuchsanlage und Strömungsformen

Abbildung 2 stellt das Schema der Versuchsanlage mit ihrem wesentlichen Komponenten dar. Der Versuchstand modelliert den Reaktordruckbehälter und eine der Hauptkühlmittelleitungen, die zum Dampferzeuger führt. Die Krümmung am Dampferzeuger wird nicht modelliert. Die Einspeisung vom Kühlmittel wird mittels einer Wasserströmung unter dem Effekt einer gegengerichtete Luftströmung, die das Ausblasen von Dampf aus dem Reaktorkern darstellt, modelliert.

Der Kern der Anlage ist der Versuchskanal, mit einer Länge von 470 mm und einer rechteckigen Querschnittsfläche von 110 x 90 mm (Breite x Höhe). Wasser und Luft strömen in den Kanal ein und bilden eine gegengerichtete zweiphasige Schichtenströmung. Umgebungsluft wird mit einem Gebläse angesaugt und durch eine Einlaufstrecke bis zur Messstrecke transportiert. Dort kommt die Luft mit dem Wasser in Kontakt. Eine dünne Platte wird an dieser Stelle auf die Wasserhöhe, y_A, eingestellt. Damit ist ein sauberer Übergang für die Luftströmung gewährleistet. Die Wasserhöhe am Eintritt des Kanals, y_0, kann auch eingestellt werden. Werte von y_0 zwischen 3 und 15 mm wurden untersucht.

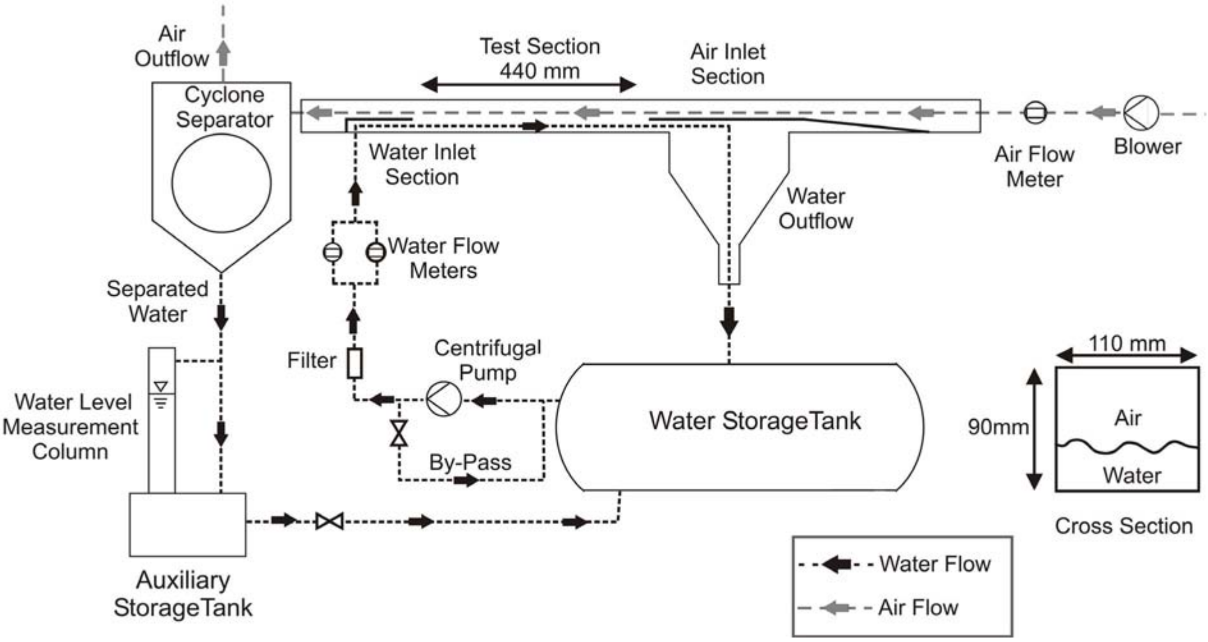

Abbildung 2. Die WENKA – Anlage.

Je nach Geschwindigkeitsverhältnis werden verschiedene Strömungsformen im Kanal beobachtet:

- *Gegengerichtete Schichtenströmung mit überkritischem Wasserfilm: Das* Wasser wird überkritisch eingespeist, d.h. die Froude – Zahl im gesamten Kanal ist höher als eins. Trägheitskräfte sind dominant. Die Phasengrenze ist relativ glatt und die Filmhöhe ist kleiner als die kritische Filmhöhe, y_C (Filmhöhe für die die Froude – Zahl gleich eins ist). Der Wasserpegel nimmt in Wasserströmungsrichtung progressiv zu. In einer überkritischen Strömung können sich keine Wellen stromaufwärts fortpflanzen.

- *Gegengerichtete Schichtenströmung mit unterkritischem Wasserfilm:* Das Wasser wird unterkritisch eingespeist, d.h. die Froude – Zahl im gesamten Kanal ist kleiner als eins. Die Schwerkraft ist in dieser Art Strömung dominant. Die Phasengrenze ist wellig und die Filmhöhe ist größer als die kritische Filmhöhe. Der Wasserpegel nimmt in Wasserströmungsrichtung progressiv ab. In einer unterkritischen Strömung können sich Wellen stromaufwärts fortpflanzen.

- *Gegengerichtete Schichtenströmung mit einem hydraulischen Sprung:* Das Wasser wird überkritisch eingespeist aber ein Übergang zur unterkritischen Strömung findet im Kanal in Form einer sprunghaften Änderung des Wasserpegel statt. Ist die Strömung überkritisch im gesamten Kanal, findet der hydraulische Sprung immer am Ende des Kanals statt, sobald die kritische Höhe, $y_{A,C}$ dort erreicht wird.

- *Partielle Strömungsumkehr:* Die Luftgeschwindigkeit ist hoch genug, um eine Strömungsumkehr hervorzurufen. Eine Instabilität bildet sich am Ende des Kanals und nimmt die Form eines hydraulischen Sprungs an, der sich stromaufwärts plötzlich verbreitert. Die Phasengrenze wird gestört und wellig.

- *Totale Strömungsumkehr:* Das ganze Wasser strömt in Richtung der Luftströmung. Für ausreichende hohe Geschwindigkeiten wird Schwallströmung („slug flow“ in der englischen Literatur) mit Wellen mit langen Amplituden beobachtet. Ab diesem Zeitpunkt kann der Wasserdurchsatz erhöht werden, trotzdem strömt aber kein Wasser bis zum Ende des Kanals wegen Strömungsbegrenzung.

Die Strömungsformen, die in der Anlage auftreten, werden in **Abbildung 3** in Abhängigkeit der Leerrohrgeschwindigkeiten von der Flüssigkeit und vom Gas dargestellt. Die Abkürzungen UK, HS und ÜK werden für Unterkritische Strömung, Hydraulischer Sprung und Überkritische Strömung verwendet.

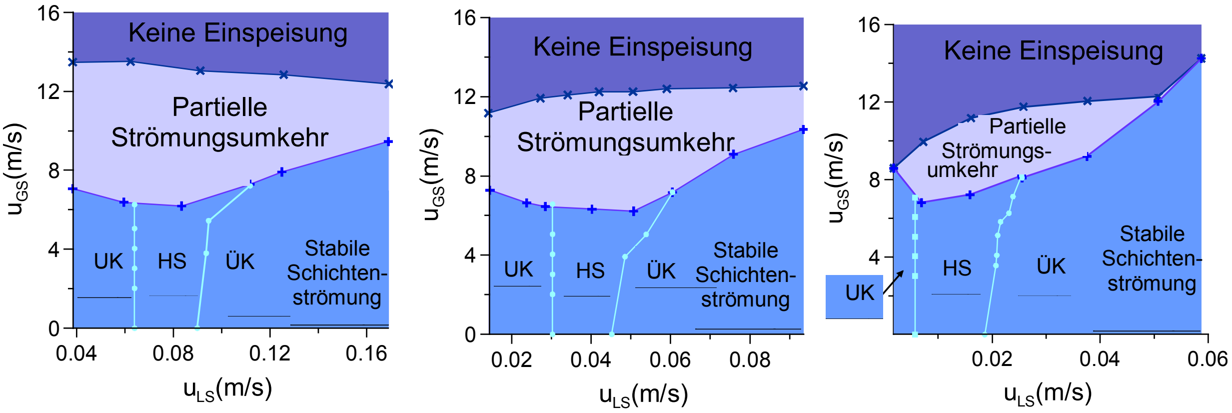

$y_0 = 15$ mm $y_0 = 9$ mm $y_0 = 3$ mm

Abbildung 3. Strömungskarten für Wassereinlaufshöhen zwischen 15 und 3 mm.

Theoretische Modelle

Es wurde experimentell beobachtet, dass der Übergang von überkritischer Strömung zur Strömungsumkehr mit dem Auftreten eines hydraulischen Sprungs am Ende des Kanals übereinstimmt. Aus diesem Grund wurde ein theoretischer Ansatz zur Bestimmung des Fließwechsels zwischen überkritischer und unterkritischer Strömung abgeleitet. Dieses Model berührt auf die Momentumsgleichung eines Wasserfilms mit Gegenstrom von Luft in einem Kanal. Folgende Gleichung

$$\frac{\ell}{y_0} = \frac{8\left(\frac{3}{4}\mathrm{Fr}_0^{\;2/3} + \frac{1}{4}\mathrm{Fr}_0^{-2} - 1\right)}{0.3164\,\mathrm{Re}_L^{\;-1/4} + \frac{\rho_G}{\rho_L}(s+1)^2(0.14\cdot 10^{-5}\,\mathrm{Re}_L + 0.021)} \qquad \text{Gl. 1}$$

wird beim Auftreten eines hydraulischen Sprungs am Ende des Kanals erfüllt. Hierbei sind ℓ die Kanallänge, Re_L die Reynoldszahl der Flüssigkeit, s der Schlupf zwischen Luft und Wasser ($s = u_G / u_L$), ρ_G und ρ_L die Dichten der Luft und des Wassers und Fr_0 die Froude- Zahl am Eintritt des Kanals, gebildet mit dem Wasserpegel am Eintritt, y_0. Diese Gleichung sagt das Auftreten eines hydraulischen Sprungs im Kanal für Einlaufwasserhöhen zwischen 3 und 15 mm voraus. Ein Vergleich mit experimentellen Daten zeigte eine gute Übereinstimmung.

Da ein hydraulischer Sprung auch ohne Strömungsumkehr im Kanal beobachtet wurde, muss es eine zweite Bedingung geben, die beim Auftreten von der Strömungsumkehr erfüllt werden muss. In der Literatur vorhandene Korrelationen zur Bestimmung der Strömungsumkehr wurden untersucht. Fast alle Korrelationen sind Modifikationen der Wallis Korrelation:

$$m u_{LS}^{*\;1/2} + u_{GS}^{*\;1/2} = C \qquad \text{Gl. 2}$$

u^*_{GS} und u^*_{LS} sind die dimensionslose Leerrohrgeschwindigkeiten vom Gas und von der Flüssigkeit, m und C sind zwei Konstanten, die den experimentellen Daten angepasst werden sollen. Diese Korrelation ist empirisch und berücksichtigt nicht die Physik der gegengerichteten horizontalen Strömung, da sie für vertikale Strömung entwickelt wurde. Es existiert eine ähnliche Korrelation, auch von Wallis vorgeschlagen, die für horizontale Strömung analytisch abgeleitet wurde:

$$u_{LS}^{*\,1/2} + u_{GS}^{*\,1/2} = 1 \qquad \text{Gl. 3}$$

Diese Korrelation wurde in mehreren experimentellen Arbeiten überprüft. Alle Autoren waren der Meinung, dass die von der Korrelation vorhersagten Werte zu hoch sind. Richter et al. stellten fest, dass eine breite Palette experimenteller Werte mit folgender Variation der Korrelation

$$u_{LS}^{*\,1/2} + u_{GS}^{*\,1/2} = 0.7 \qquad \text{Gl. 4}$$

dargestellt werden konnte.

Die experimentellen Daten der WENKA – Anlage wurden in einem Diagramm „Dimensionslose Wasserhöhe – Wallis Konstante“ dargestellt.

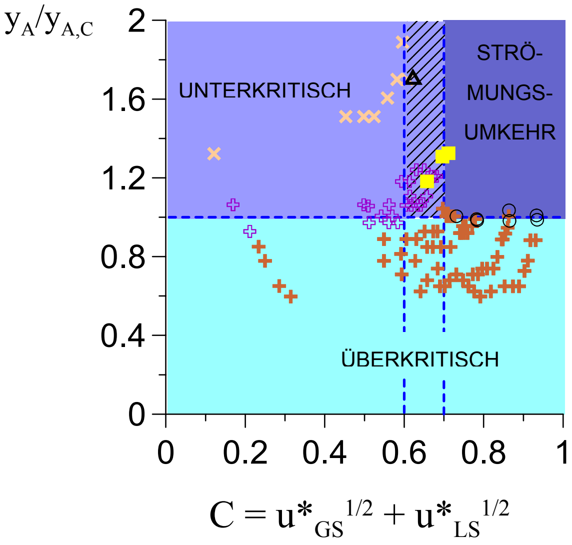

Abbildung 4. Strömungsformen in Abhängigkeit von der Wallis Konstante C und der dimensionslose Wasserhöhe am Ende des Kanals.

Es wurde für verschiedene Wassereinlaufshöhen experimentell beobachtet, dass die Strömungsumkehr erst für Werte von *C* = 0.7 stattfindet. Damit ist das neue Kriterium für das Auftreten von Strömungsumkehr:

$$u_{LS}^{*\,1/2} + u_{GS}^{*\,1/2} \geq 0.7 \quad \text{und} \quad \frac{y_A}{y_{A,C}} \geq 1 \qquad \text{Gl. 5}$$

Wasserlieferungsraten

Die während partieller Strömungsumkehr gelieferte Wassermenge wurde mit einer Füllstandsonde in mehreren Experimenten gemessen. Ein Einspeisungsverhältnis, *b*, wurde definiert als

$$b = \frac{\dot{m}_{L2}}{\dot{m}_{L0}} \qquad \text{Gl. 6}$$

Hier ist $\dot{m}_{L0}$ der Wassermassenstrom, der in den Kanal eingespeist wird und $\dot{m}_{L2}$ der Wassermassenstrom, der von der Luft mitgerissen wird. Es fließt dann ein Wassermassenstrom $\dot{m}_{L1}$ bis zum Ende des Kanals. Es ist klar, dass $0 \le b \le 1$.

Abbildung 5 zeigt die Werte von *b* über die Luftgeschwindigkeit in der Lufteinlaufstrecke $u_{G,IN}$. Diese Geschwindigkeit stimmt mit der Leerrohrgeschwindigkeit der Luft überein.

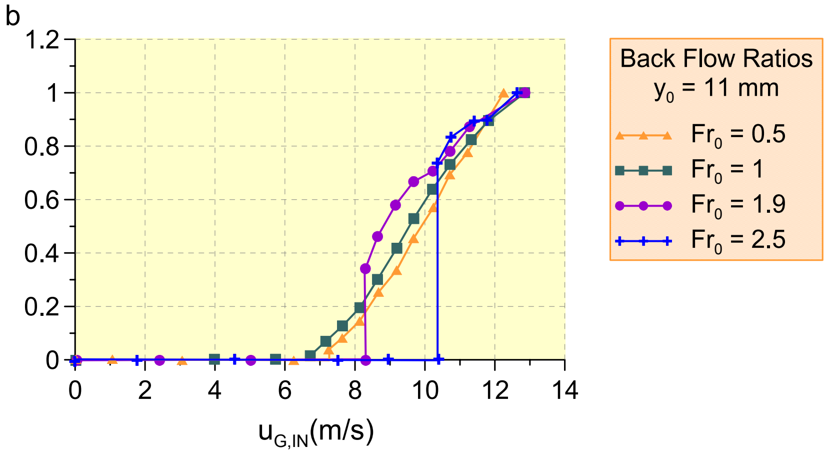

Abbildung 5. Einspeisungsverhältnis für verschiedene Froude – Zahlen.

Die Wasserlieferraten nehmen sprunghaft ab, sobald die Strömungsumkehr auftritt. Hier kann der Einfluss der Froude - Zahl beobachtet werden. Anderseits, wenn die Strömungsumkehr stattgefunden hat, spielt die Froude - Zahl eine untergeordnete Rolle. Eine empirische Korrelation zur Abschätzung der Wasserlieferraten wurde gefunden:

$$b = -1.22 + 0.09 \mathrm{Fr}_0 + 2.88 \times 10^{-5} \mathrm{Re}_{G0} \quad \text{wenn} \quad 0 \le b \le 1 \quad \text{und Gl. 5 ist erfüllt.} \qquad \text{Gl. 7}$$

Diese Korrelation ist von empirischen Charakter und darf nicht extrapoliert werden.

CONTENTS

1 Introduction

Stratified flow is a very common two-phase flow pattern in countless test facilities, devices and industrial applications, and consequently, has been the focus of numerous research programs in the last decades ([19], [43], [74]).

Under *stratified flow* should be understood a horizontal or near horizontal two-phase flow, i.e. of liquid and gas, in which the liquid (or the phase with higher density) flows in form of a film due to the presence of a gravity field and the gas flows at the upper part of the pipe. Interactions between both phases (mass, momentum and energy exchange) occur through the interface between gas and liquid and show strong dependence on the relative phase velocities ([19], [68]). *Countercurrent stratified flow* exists if both phases flow in opposite direction (see Fig. 1.1).

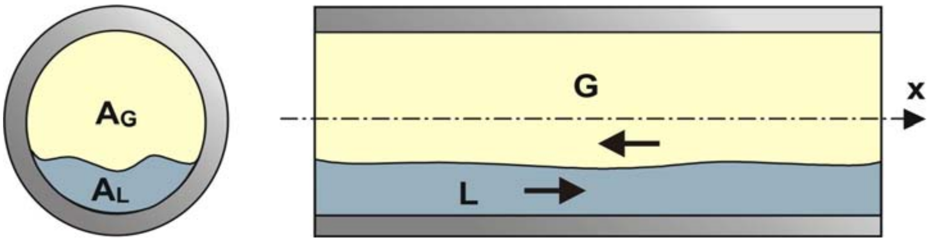

Fig. 1.1. Horizontal countercurrent stratified flow.

In Fig. 1.1 the liquid flows in the positive x direction and occupies a fraction of the total cross sectional area A equal to A_L (cross sectional area of the liquid) whereas the gas flows countercurrently occupying an area A_G. The values of A_L and A_G usually depend on position and time.

The understanding of stratified flows plays an important role in technical applications. By transporting natural gas and petroleum through pipelines, accurate prediction of the pressure losses is necessary ([6], [7]). During the injection phase in Diesel engines in the cold start phase, stratified flow of air and fuel occurs at the inlet port leading to the engine. The behaviour of these stratified flows must be modeled to optimize the generation of toxic gases [24]. In **L**ight **W**ater **R**eactors (LWRs), safety analysis and accident management requires a good knowledge of thermal-hydraulic phenomena of stratified flows [21], [40], [47]. As an example, countercurrent stratified flow of cooling water and saturated steam can happen during emergency core cooling in **Lo**ss of **C**oolant **A**ccidents (LOCAs) if feed water is injected into the core through the hot leg of the primary cooling circuit. Assessment on the transient progress and on the consequences of the accident involves acquaintance with the physics of countercurrent stratified flows.

Although the concept of stratified flow is linked to horizontal flow, there exist some cases, in which vertical stratified flow is possible. In LWRs, during a core melt down accident with subsequent blow-down of the **R**eactor **P**ressure **V**essel (RPV) [50], vertical stratified flow of molten material and steam sets in at the inner wall of the reactor cavity. Hereby, the molten material is driven by the steam and builds up a liquid film that is sustained by the shear stress applied at the interface by the discharged steam. This is a transient state that holds as long as the inertial term is dominant on the gravitational one, and represents one of the few cases, where vertical stratified flow can be observed. Excluding such special situations, stratified flow always deals with horizontal or near horizontal flow.

The main interest of this work is focused to countercurrent stratified flow present in nuclear reactor systems, with specific application to hot leg injection during a LOCA. In the next chapter, explicit details from the technical point of view are presented.

1.1 Technical Background: Emergency Core Cooling in LWRs

1.1.1 The Emergency Core Cooling System as a Main Safety System in LWRs

According to the definition given by the **I**nternational **A**tomic **E**nergy **A**gency (IAEA), *safety systems* are “systems important to safety to assure the safe shutdown of reactor or residual heat removal from the core or to limit the consequences of anticipated operational occurrences or accident conditions” [35]. *Anticipated operational occurrences* are events which are expected during the operation life of a nuclear reactor whereas *accident conditions* are events that occur unexpectedly and are included in future nuclear power plant designs as *design basis accidents*. Thus, design basis accidents are postulated accidents a nuclear plant is planned and built to withstand, without releasing radioactive materials to the outside environment. Usually, a set of design basis accidents is postulated for each type of reactor covering the consequences of all combinations of failures. The safety systems of a nuclear power plant are designed taking into account this given set of design basis accidents.

Nowadays, all light water reactors have some form of emergency makeup water system in case of any accident resulting in a loss of reactor coolant. This main safety system is the **E**mergency **C**ore **C**ooling **S**ystem (ECCS).

The ECCS is designed to secure a safe removal of heat from the reactor core in the event of emergencies involving pipeline ruptures of reactor primary and secondary coolant circuits (LOCAs). Under such accident conditions, a considerable amount of coolant can be lost and the ECCS compensates this with injection of additional coolant. It is of vital importance that the core remains adequately cooled in any situation. Even after a successful shutdown, heat continues to be produced from the decay heat of unstable isotopes in the fuel. The ECCS is needed, on one hand, to remove the decay heat of the reactor’s fuel after reactor shutdown if there is no residual heat removal system available, and on the other hand, to avoid core uncovering or to reflood the core if uncovering already happened. Thus, the ultimate function of the ECCS is to avoid high core temperatures, since fuel temperatures could raise and yield a core melt down accident.

Emergency core cooling in **P**ressurized **W**ater **R**eactors (PWRs) typically comprehends three stages: a high pressure injection, a low pressure injection and a recirculation phase. The accident progress and the behaviour of the ECCS depend strongly on the type of LOCA. We distinguish between large break LOCAs and small break LOCAs.

a) Large-Break-LOCAs

A Loss-of-coolant accident caused by a break in the primary coolant system larger than 464.5 cm² (0.5 ft²) is referred to as **L**arge-**B**reak LOCA (LB-LOCA). The most serious hypothetical LB-LOCA is that occasioned by a complete rupture of a main coolant pipe (double-ended rupture).

High Pressure Injection

LB-LOCAs cause a rapid depressurization of the primary coolant circuit. During pipe rupture, a depressurization wave (between 50 and 100 bar) will sweep through the primary system at speeds of about 1000 m/s [46]. The arrival of this wave front in the vessel will induce vacuum in the downcomer resulting in a stress load on the vessel shell rings and on the core support comparable to the effect of an earthquake, for example. In addition, the control rods mechanisms will be subjected to high lateral stresses.

As soon as the break occurs, a mixture of water and steam flows out through the breach at the speed of sound (critical flow rate). Since the break size is large, the heat is mainly removed by the break flow. Primary system drainage is accompanied by rapid drop in the primary system pressure down to saturation pressure in the hot leg region. The liquid level could reduce rapidly to values below the top of the core and the flow out of the break could be all steam. To prevent the core to uncover, reduced pressure in the reactor automatically causes water to be injected into the core. High pressure injection is performed by the ECCS. High pressure injection system pumps deliver borated water from a storage tank to the reactor pressure vessel. However, the flow rate delivered by the high pressure system pumps is considerably below the rate of discharge at the break. Once the pressure in the system has reduced down to a given pressure, water is injected from accumulators which are pressurized a few bar under this boundary pressure. In some PWR designs, the accumulators discharge pressure is slightly below the system pressure, leading to an almost simultaneous injection by means of the high pressure system pumps and the accumulators. In other designs, the high pressure system pumps provide long duration high-pressure flow until the system pressure decreases to 40 bar. Then, the accumulator tanks empty automatically into the primary system. Independently of the chosen injection configurations, it is a fact that the volume of coolant which can be contained within the accumulators is limited and provision must be made to cool the core after the accumulator supply is exhausted. This is accomplished by the low pressure injection system.

Low Pressure Injection

Low pressure injection system pumps are connected to a large low-pressure reservoir. The pumps are activated by a low-pressure signal (i.e. 30-35 bar) to reflood the core. Hence, the low pressure injection system provides long duration low-pressure flow and can be used to establish long term cooling immediately after the core has been recovered.

Recirculation

The coolant that flows out of the primary circuit through the break accumulates in the containment sump and can be used as an additional reservoir of coolant. Once the liquid level in the low-pressure tank connected to the low pressure injection system reduces considerably or the containment sump achieves 45% of its full capacity, the water collected in the sump is recycled by the low pressure injection system pumps. This phase is called *recirculation* and it takes most of the transient time.

b) Small-Break-LOCAs

The **S**mall-**B**reak LOCA (SB-LOCA) is generally considered to be a LOCA initiated by a primary system rupture with a break flow area of less than 464.5 cm² (0.5 ft²). If a SB-LOCA occurs, the rate at which the reactor depressurizes depends strongly on the size of the break, but this depressurization does not happen rapidly. Thus, often the high pressure injection system is actuated but not the accumulators or the low pressure injection system, so that the consequences of a SB-LOCA are typically mitigated by the high pressure injection system. However, in some scenarios corresponding to a break size near the upper range of the small-break spectrum, the flow rate injected by the high pressure system pumps is no longer sufficient to compensate the loss of coolant and accumulator flow is initiated. On the other hand, for smaller break sizes, heat cannot be removed by the break flow and cooling via steam generators becomes more important as the break size decreases. Thus, heat removal is primarily done by means of natural circulation flow through the steam generators. Forced circulation is not available since the primary coolant pumps are generally tripped shortly after the accident begins.

The duration of the event is much longer than in a LB-LOCA. A portion of the core can be uncovered during accidents in this category. Since the transient can be very slow, the uncovered period may be relatively long and the potential core damage during SB-LOCAs is therefore greater than for large-break ones. Even if there is no core uncovering, SB-LOCAs may be potentially very dangerous, since there exists the possibility of **P**ressurized **T**hermal **S**hock (PTS). A PTS event refers to a transient causing a very rapid cooling of the RPV wall, while the vessel is maintained at high pressure. The concern is that the cooling will bring a substantial portion of the vessel to a temperature where a brittle fracture may occur.

Boiling **W**ater **R**eactors (BWRs) generally have similar provisions for injecting cooling water. However, the high pressure injection is generally performed by use of pumps rather than by use of accumulators.

1.1.2 Injection Location in PWRs

Fig. 1.2 shows possible injection locations in a PWR. In reality, the cold leg and the hot leg are attached to the reactor pressure vessel at the same height but at different radial positions of the vessel. In Fig. 1.2 the hot leg was represented at a lower position in order to facilitate the understanding of the drawing.

In most PWRs water is injected by the ECCS into the primary system through nozzles in the cold legs of all loops (Cold Leg Injection). Water then enters the RPV in the usual manner: it flows downward through the thermal shield and then upward through the core. The procedure is often designated *bottom flooding*. This injection mode is employed by most PWRs in USA and Japan [21].

However, the ECCS in the four-loop German PWRs (PWR, Siemens / KWU) performs *combined injection*: coolant is injected by the ECCS through nozzles in the cold legs as well as in the hot legs. The coolant injected into the hot leg flows directly into the core from its upper part. This is a unique feature of German PWRs.

American Babcock & Wilson PWRs (B&W-PWR) are 2x4 loop designs where ECC injection is performed through nozzles located in the cold legs (high pressure injection) and nozzles located in the downcomer (accumulator and low pressure injections). Some Japanese PWRs also use this injection mode. Similarly, the German plant Mülheim-Kärlich (Brown Boveri reactor, nowadays Westinghouse) performs downcomer injection as well as cold leg injection with two separated ECCS.

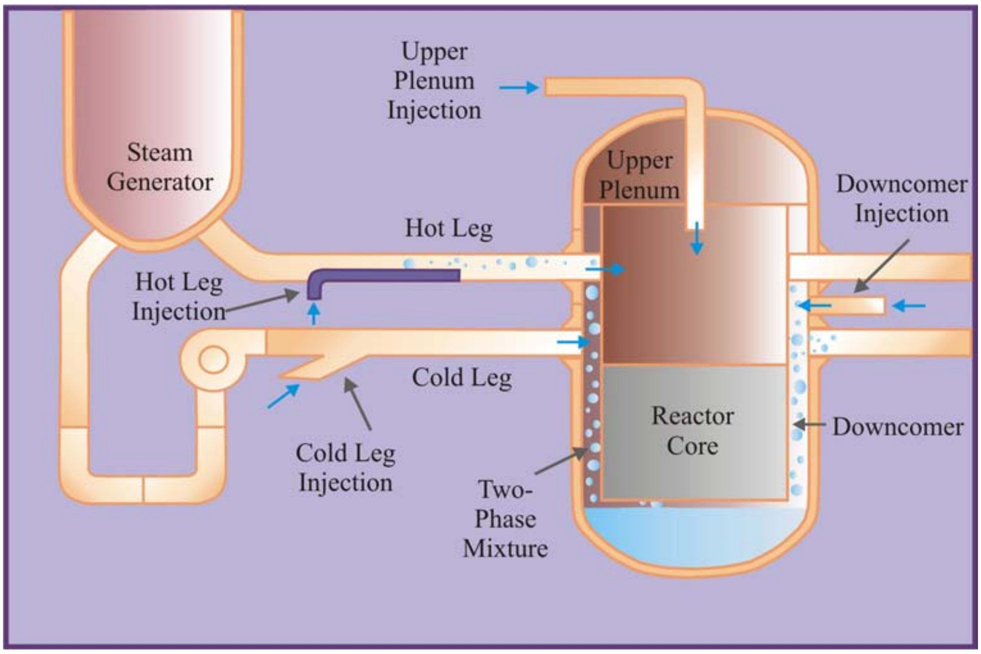

Fig. 1.2. Simplified sketch showing possible injection locations during ECC in PWRs.

In some two-loop PWRs in Japan and the USA the low pressure injection is carried out through the upper plenum instead of through the cold leg as in three and four-loop plants. The coolant injected by the low pressure injection system enters then from the top.

1.1.3 Hot Leg Injection

During a LOCA in a PWR, hot leg injection of cooling water is performed by the ECCS by means of a secondary pipeline placed at the bottom of the feed line of the primary circuit (see Fig. 1.3). It is essential that the injected cooling water reaches the reactor core at a sufficient flow rate, in order to guarantee coolability during the transient.

Typical hot leg diameters range about 750 mm and the equivalent radius of the semi-elliptical secondary pipe is of about 160 mm. These values can vary according to the power plant construction type, but they are quite representative.

Under accident conditions, coolant is injected at a high mass flow rate through the hot leg. The injected mass flow rate depends strongly on the status of the accident and on the peculiarities of the nuclear plant. A realistic injection mass flow rate would be in the range between 150 and 400 kg / s. The corresponding Froude numbers at the injection point (calculated with D = 750 mm and R_{eq} = 160 mm, see Fig. 1.3) are 5 and 14, which are very large values. The concept of Froude number will be introduced in chapter 1.3.1. For the moment, we will say that the Froude number is a dimensionless parameter used as a measure of the inertia of the flow. A large Froude number means in this case, that the liquid film is injected by the ECCS at a high velocity.

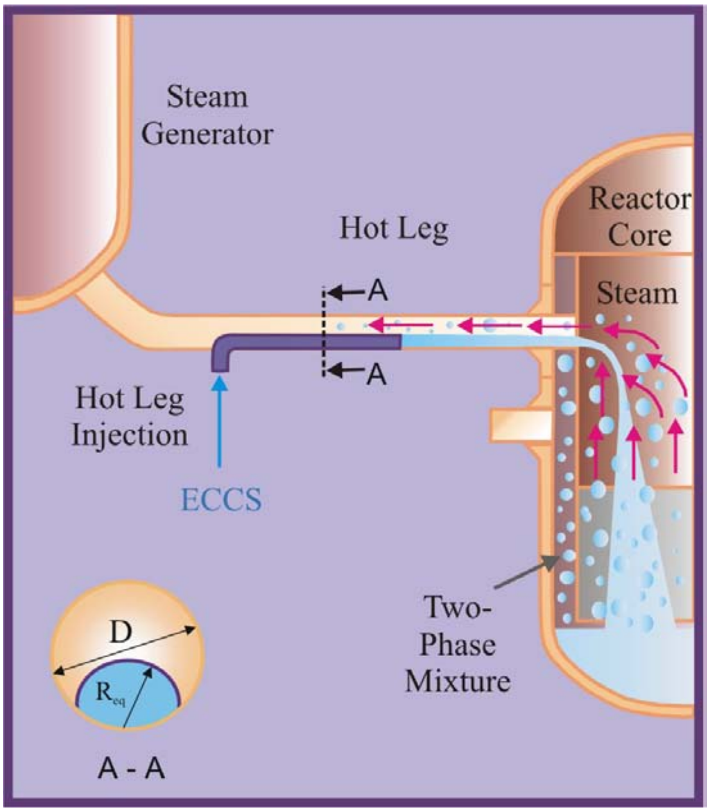

Fig. 1.3. Countercurrent Flow of saturated steam and cooling water in hot leg of PWR during a LOCA.

Since the primary system depressurizes at high temperatures, saturated steam flows out of the RPV into the hot leg (see Fig. 1.3). A countercurrent stratified flow of injected cooling water and saturated steam occurs. Due to the high temperatures typical of such accident scenarios, steam is generated at high flow rates in the reactor core: between 7 and 32 kg/s of steam can flow into the hot leg. If we take into account that the injected coolant must flow inside the hot leg approximately one and a half meter until it reaches the reactor core counter a steam flow with velocities ranging between 8 and 33 m/s (steam Reynolds number ranging between $1 \cdot 10^6$ and $4 \cdot 10^6$), then, it is reasonable to perform a large Froude number injection to assure liquid penetration into the core at high pressure. However, despite these large Froude numbers, flow phenomena like a hydraulic jump or reversed flow can occur in the hot leg depending on the flow rates of steam and water.

The onset of reversed flow (in the literature also defined as *flooding*) determines the flow rates, at which less cooling water penetrates into the core and can lead to the so-called *zero penetration point,* at which no coolant flows into the reactor. This scenario should be avoided, since no safe reactor shutdown can be guaranteed if residual heat of the core cannot be removed.

1.2 Background of the Present Work

The main objective of the present work is to investigate the stability of horizontal countercurrent stratified flow of liquid and gas to understand and predict the behaviour of the ECCS during hot leg injection.

In the following sections of this chapter, some definitions are introduced concerning horizontal stratified countercurrent flow and its stability. After this, a literature survey about investigations done in the last decades in this subject is presented. Finally, the main objectives of this study are presented taking into account the research areas where further investigations are needed.

Chapter 2 describes the test facility WENKA, where new experiments concerning the problem of ECC hot leg injection were performed with air and water in a horizontal channel. Additionally, the experimental procedure employed is described in this chapter.

Furthermore, it will be shown, that prediction of countercurrent flow stability is closely linked to the prediction of occurrence of a hydraulic jump in the pipe. Therefore, a one-dimensional model, based on the momentum equations of the liquid film, will be proposed in chapter 3 to predict the onset of a hydraulic jump in a closed channel under countercurrent flow conditions.

In chapter 1, experimental results are presented as well as a comparison with the predictions given by the theory presented in chapter 3.

Finally, conclusions and an outlook are given in chapter 6.

1.3 Definitions

In order to describe and classify flow phenomena appearing in countercurrent stratified flow, some useful definitions must be introduced.

1.3.1 Froude Number and Flow Regime Classification

The local Froude number of a liquid film at the position x in a horizontal channel of length ℓ is defined as

$$Fr_X = \frac{u_L(x)}{\sqrt{gy(x)}} \tag{1.1}$$

Where x is any position in the channel ($0 < x < \ell$), g is the acceleration of gravity, and $u_L(x)$ and $y(x)$ are the mean liquid velocity and the liquid depth at a position x, respectively.

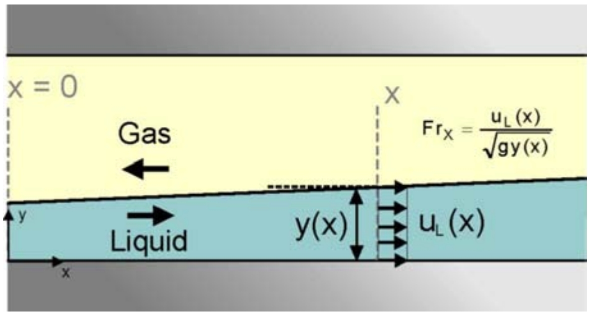

Fig. 1.4. Liquid Froude number in countercurrent stratified flow.

The Froude number is a dimensionless number that represents the ratio of inertial to gravitational forces. The inertial force F_a is represented in a fluid by the expression

$$F_a = m_F \cdot a = m_F \frac{u}{t} = m_F \frac{u}{\delta/u} = \frac{m_F \cdot u^2}{\delta} \tag{1.2}$$

Where m_F is the mass of the fluid, a the acceleration, t the time, u the velocity and δ is a typical length. The gravitational force is given by

$$F_g = m_F \cdot g \tag{1.3}$$

Now the ratio between inertial and gravitational forces can be expressed as

$$\frac{F_a}{F_g} = \frac{m_F \cdot u^2}{\delta m_F g} = \frac{u^2}{g\delta} \tag{1.4}$$

It is clear that the Froude number is just the square root of this expression if the liquid depth y is chosen as typical length δ.

On the other hand, it is known from open channel hydraulics ([15], [26], [31]) that the denominator of the Froude number is the celerity c of an elementary gravity surface wave in shallow water:

$$c(x) = \sqrt{gy(x)} \tag{1.5}$$

According to this, the Froude number can be accounted as a ratio between the velocity of the flow and the celerity of an elementary gravity wave:

$$Fr_x = \frac{u_L(x)}{c(x)} \tag{1.6}$$

This second form of the Froude number leads to some additional interesting conclusions when classifying flow regimes.

Depending on the Froude number and on the flow rates of liquid and gas, the flow regimes observed in horizontal countercurrent stratified flow can be classified as follows:

a) Subcritical Flow

The flow is **S**u**b**critical (SB) in a channel section ℓ if the Froude number is less than unity within this channel section. In a subcritical flow, the mean velocity is relatively low although a subcritical flow always accelerates into the direction of the flow. As it is shown in Fig. 1.5, the liquid depth reduces progressively in the flow direction and therefore, the local velocity increases downstream. In a subcritical flow gravitational forces are dominant.

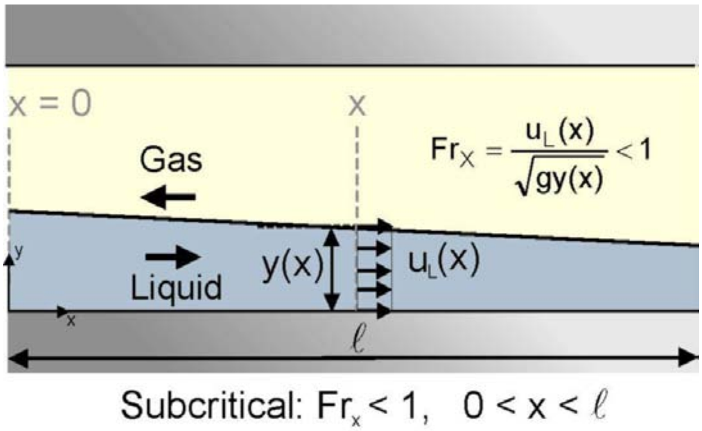

Fig. 1.5. Subcritical countercurrent flow.

Since a Froude number less than unity means that the velocity of the flow is less than the celerity of an elementary gravity wave, surface waves can travel faster than the flow itself. Such a wave can propagate upstream against the flow and upstream areas are in hydraulic communication with downstream areas. Essentially, in a subcritical flow any disturbance influences the upstream conditions, so that surface waves can propagate either upstream or downstream. This is a crucial property of subcritical flows regarding the problem of countercurrent flow stability.

b) Supercritical Flow

The flow is **Sup**ercritical (SP) in a channel section ℓ if the Froude number is higher than unity within the entire channel section. In a supercritical flow, the mean velocity is relatively high and the inertial term is dominant. However, a supercritical flow always decelerates in the direction of the flow and the liquid depth increases progressively in the flow direction (See Fig. 1.6).

In a supercritical flow, only the so-called *supercritical waves* can be observed. These surface waves are generated by means of capillarity. They propagate always in the flow direction and generate a typical oblique interference pattern with small amplitudes and small wavelengths. Unlike subcritical flow, no other surface waves can be generated or propagated in a supercritical flow, since disturbances do not influence the flow conditions upstream. Large amplitude waves or waves which propagate upstream, are not possible in a supercritical flow, since the velocity of the flow is greater than the celerity of an elementary gravity wave. Therefore, such a wave cannot propagate upstream against the flow and the upstream areas of the channel are not in hydraulic communication with the downstream areas.

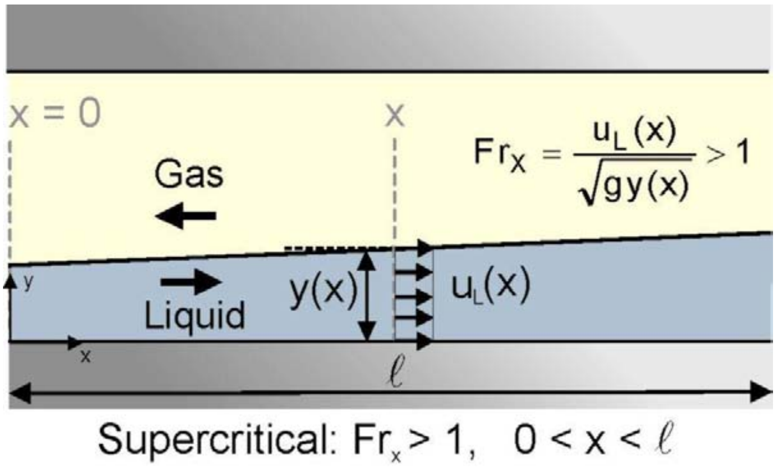

Fig. 1.6. Supercritical countercurrent flow.

c) Hydraulic Jump

A transition from supercritical to subcritical flow does not occur continuously, but in the form of a **H**ydraulic **J**ump (HJ) (see Fig. 1.7). Thus, a hydraulic jump means a sudden increase in liquid depth at a certain position of the channel and a change in the type of waves of the flow. As soon as a hydraulic jump occurs in the channel, surface waves can be generated at the subcritical side of the flow and propagate upstream.

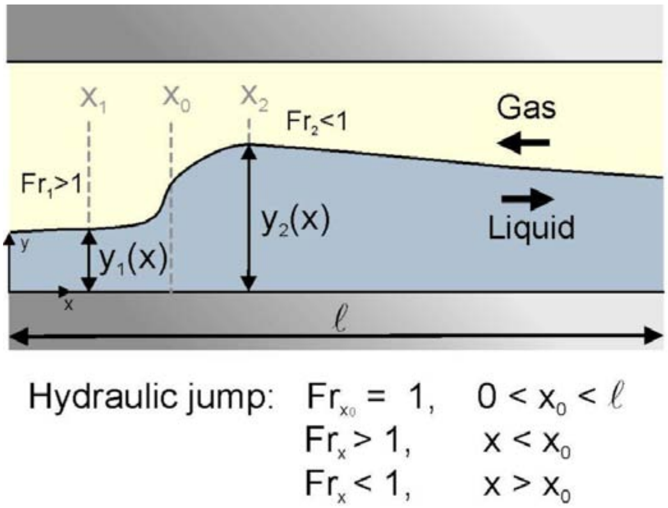

Fig. 1.7. Hydraulic jump in horizontal countercurrent flow.

Readers who are acquainted with gas dynamics, will have noticed something familiar in the preceding definitions. In fact, since subcritical and supercritical flow are defined in relation to a natural wave velocity, they are closely analogous to subsonic and supersonic flow respectively, which are defined in terms of the natural velocity of a small amplitude compression wave in a gas, i. e. the velocity of sound. Therefore, the so-called supercritical waves could be analogous to supersonic waves in gas flows as well as there exists a parallelism between the Froude number for incompressible film flow and the Mach number for compressible flow. In this analogy, the hydraulic jump corresponds to a shock front in gas dynamics.

1.3.2 Reversed Flow

In horizontal, stratified countercurrent flow of gas and liquid, a limit can be reached, at which the liquid flows partially in the gas direction, and therefore liquid delivery in initial direction is reduced. A breakdown of the stable countercurrent stratified two-phase flow occurred. This is often referred to as *flooding* in the literature. Since flooding defines the flow conditions, for which the liquid begins to flow, partially or totally, in the gas flow direction, the terms *reversed flow* and *flow reversal* will be used in this work as an equivalent term to flooding, as the liquid begins to flow *reversely*. The onset of flow reversal defines the maximum rate at which both liquid and gas phase can flow countercurrently. A further increase of the gas flow rate leads to instabilities and the countercurrent flow can not be sustained as a stratified flow: the liquid phase is carried either partly or fully by the gas phase.

Depending on the quantity of liquid that is carried over by the gas, flow reversal can be classified into two different types: *partially reversed flow* or *totally reversed flow*.

a) Partially Reversed Flow

For sufficiently high gas velocities, part of the liquid begins to flow in the gas direction whereas the rest of the liquid still flows in the initial direction (see Fig. 1.8). This phenomenon is referred to as *partially reversed flow.*

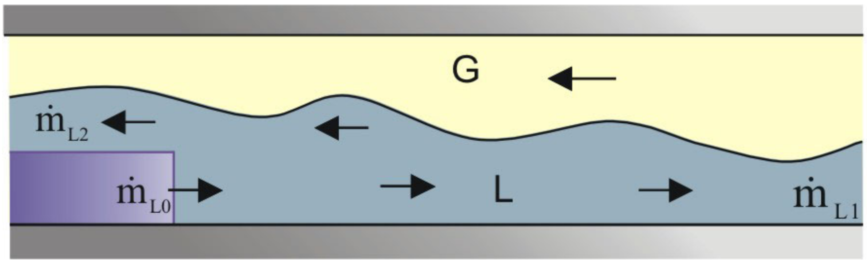

Fig. 1.8. Partially reversed flow.

Under partially reversed flow, a part of the initial mass flow rate $\dot{m}_{L0}$ flows backwards driven by the gas. Thus, there exists a reduced liquid delivery rate $\dot{m}_{L1}$, $0 < \dot{m}_{L1} < \dot{m}_{L0}$, and a back flow rate $\dot{m}_{L2}$. It is useful to define a *back flow ratio* as

$$b = \frac{\dot{m}_{L2}}{\dot{m}_{L0}} \tag{1.7}$$

It is evident that

$$0 \le b \le 1 \tag{1.8}$$

b) Totally Reversed Flow

For much higher gas velocities, the entire liquid is carried over by the gas. This flow regime is defined as *totally reversed flow*. In reactor applications, a totally reversed flow leads to a situation where no liquid is delivered. Therefore, the transition to totally reversed flow is often referred to as *zero liquid penetration point*. It is essential to avoid the occurrence of such a flow regime, since if the zero liquid penetration point is reached, the cooling of the reactor core during the transient cannot be guaranteed.

While a partially reversed flow corresponds to values of b, 0 < b < 1, the boundary b = 1 corresponds to the transition to totally reversed flow: for b equal to unity, the zero liquid penetration point is reached and $\dot{m}_{L1} = 0$. The lower boundary b = 0 represents stable countercurrent stratified flow.

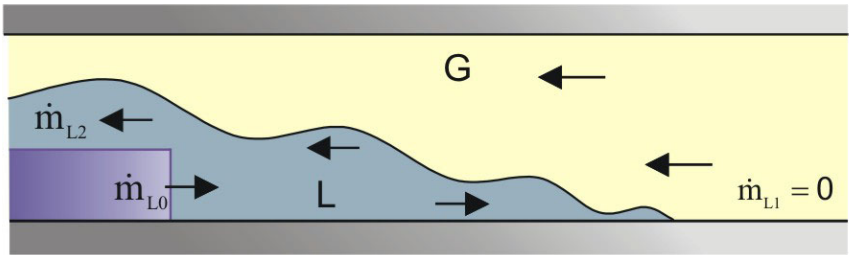

Fig. 1.9. Totally reversed flow.

c) Countercurrent Flow Limitation

Flow reversal represents a natural boundary limit of countercurrent flow, beyond which flow limiting mechanisms play a predominant role. Once reversed flow has set in, it is often impossible to increase the liquid delivery rate in initial direction by increasing the liquid supply. The liquid depth increases considerably due to turbulence and air entrainment caused by the onset of reversed flow. The flow path available for the gas can reduce significantly or even be totally blocked by liquid slugs. This leads to an immediate increase in pressure that results in limitation of the liquid delivery rate, even if the liquid mass flow rate is increased. This mechanism that limits the liquid delivery rate is often referred to as ***C**ounter-**c**urrent **F**low **L**imitation* (CCFL).

1.4 State of the Art: Literature Survey

1.4.1 Characteristics of Flow Regimes in Countercurrent Flow

The flow regimes existing in a two-phase flow usually are represented by means of a flow regime map. Flow regime maps indicate flow patterns present in a two-phase flow and their limits using a pair of independent coordinates. They are usually drawn in terms of the mass flow rates or the superficial velocities of each phase. However, since flow regimes are governed by many variables, a representation by means of only two parameters is always a “limited” representation and it is therefore indispensable to describe which parameters were varied and which ones were set constant when performing a flow regime map. Additionally, it should be emphasized that the validity of a flow regime map is reduced to the conditions it was obtained for. Flow regime maps are not general and should be extrapolated cautiously, as there is experimental evidence of a substantial effect of parameters like pipe diameter or pressure. Nevertheless, if they are used carefully, they are a useful tool to predict flow patterns under similar geometries and flow conditions.

In 1959 Baker was the first who recognized that accurate prediction of pressure drop, void fraction, heat and mass transfer as well as other hydrodynamic parameters was closely bound to the knowledge of flow regime in two-phase flow. He presented the first flow regime map for cocurrent horizontal flow [8].

Over the past forty years many different flow regime maps were presented. However, dimensionless parameters were only used by Taitel and Dukler, [64], who derived a generalized flow regime map for horizontal or slightly inclined pipes based on mathematical modeling. The dimensionless numbers to define a given transition depended on the transition itself, and Taitel and Dukler described all possible transitions for cocurrent flow with four dimensionless parameters. Unfortunately, no similar works could be found for countercurrent flow.

The influence of the Froude number on flow regimes in horizontal flows has been investigated widely in the field of open channel hydraulics. Extensive investigations were performed to study the phenomenon of the hydraulic jump as well as the flow properties of supercritical and subcritical flows ([3], [4], [13], [15], [39], [54], [60]). Since all these investigations were performed for liquids with free surface (stratified flow with stagnant air), the influences of both gas velocity and pressure were not taken into account. The effect of wind is considered in few cases, but the results obtained in these investigations cannot be applied to the case of a hydraulic jump in a closed channel, where, unlike in free surface flows, variations in gas pressure are responsible for the film morphology. Additionally, the effect of interfacial friction is often neglected.

1.4.2 Onset of Reversed Flow

Unlike hydraulic jump phenomena, for which no studies for closed channels with countercurrent flow could be found, there is a considerable amount of work on reversed flow available in the literature.

Bankoff and Lee [9] presented in 1983 a review of the existing literature on reversed flow, and classified the models proposed by different authors in wave stability theories, static equilibrium theories, envelope or limiting operating condition theories and semiempirical correlations. Fig. 1.10 shows the transition from stable annular flow to reversed flow in a vertical pipe as presented in their work. The liquid is introduced through a porous wall inlet at the top of the pipe and it is extracted smoothly at the bottom. The gas is introduced at the bottom of the tube. In this way, stable annular flow can be established (Fig. 1.10a). As the gas flow rate is gradually increased, the liquid interface becomes rough and disturbed and entrainment of droplets can be observed (Fig. 1.10b). This is the *flooding point* for some authors, like for example, for Lee and Bankoff itself. A small fraction of liquid flow is carried by the gas as entrained droplets. However, the liquid delivery rate is approximately the same as the liquid injection rate. A further increase of the gas mass flow rate leads to liquid transport above the injection point, with both climbing and falling film. The transition to this flow regime is defined by other authors as the flooding point (Hewitt and Hall-Taylor [32]) (Fig. 1.10c). This flow regime is characterized by a liquid delivery rate reduction (Fig. 1.10c and Fig. 1.10d), the so-called *countercurrent flow limitation*. The zero liquid penetration point (Fig. 1.10e) is achieved by further increasing the gas flow rate: the whole liquid is carried upwards in form of droplets and film. The transition from state a to state e can also be done reversible by reducing the gas velocity progressively. A state can be achieved, where part of the liquid film begins to flow downwards. This situation is often referred to as *flow reversal point*. Again, a climbing and a falling film exist simultaneously.

The diversity of non-coincident definitions related to reversed flow in vertical pipes is illustrated with this example. Nevertheless, for horizontal flow no different definitions are employed in the literature: the term *flooding* is used to design the break down of stability of countercurrent flow due to liquid carry over by the gas in the gas flow direction. However, to avoid possible confusions in the present work, the end of stability of countercurrent stratified flow will be referred to as *reversed flow*, as already commented in chapter 1.3. Thus, the terms *reversed flow* and *flow reversal* will be used from this point on and it is understood that they are equivalent to the term *flooding* as defined by Hewitt and Hall-Taylor.

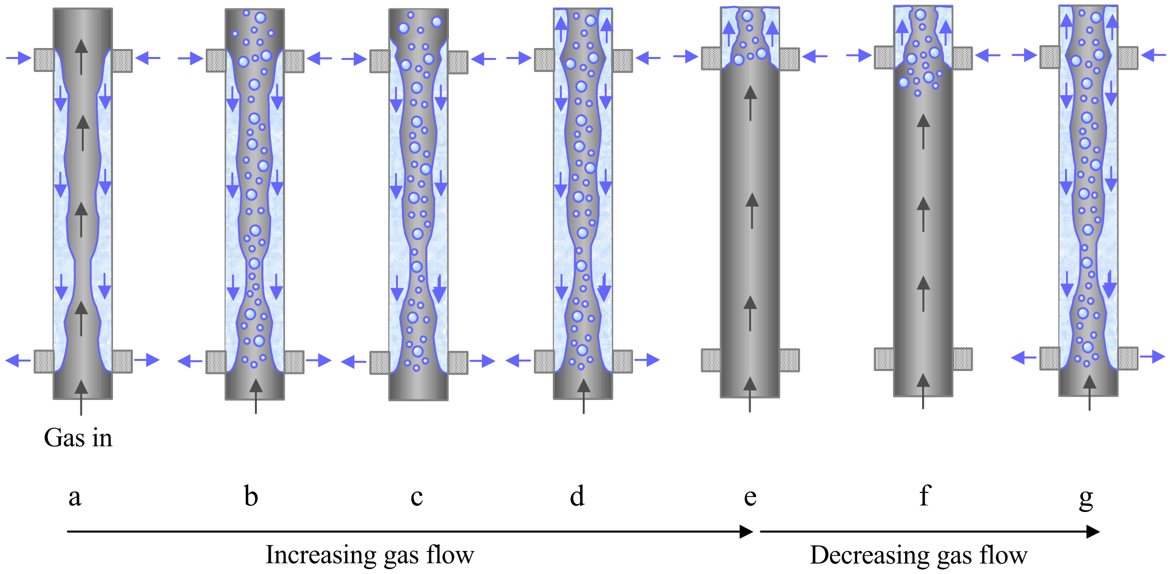

Fig. 1.10. Flooding and flow reversal in vertical flow.

a) Correlations Applied to Predict Occurrence of Reversed Flow in Horizontal Geometries

Over the last decades many correlations where presented to predict the onset of reversed flow (See McQuillan and Whalley, [49]). The work of Bankoff and Lee [9] represents one of the most useful reviews on reversed flow present in the literature. However, most of the work analyzed in their review is related to vertical countercurrent flow, since reversed flow had been studied up to that moment mostly in vertical pipes ([30], [53], [63]). In fact, reversed flow in horizontal geometry received, prior to the Three Mile Island accident (1979, [66]), relatively little attention in the literature, despite its importance concerning safety analysis of light water reactors. During the accident, CCFL prevented cooling water to flow from the pressurizer into the reactor coolant circuit.

Two types of correlations are frequently applied in most studies: Wallis type correlations and Kutateladze type correlations. Since these two types of correlation are well established in the literature additional comments about other correlations will be skipped in this chapter.

Early work for horizontal flow was performed by Wallis in 1969 ([68]). Using a one-dimensional drift-flux model, Wallis provided the region of operation where no waves grew in horizontal ducts. The onset of waves was associated with the occurrence of instabilities, which lead to reversed flow. As a result, Wallis presented a correlation based on the *dimensionless superficial velocities*, u^*, of each phase:

$$u_{GS}^{*} = u_{GS} \cdot \rho_G^{1/2} \left[gH(\rho_L - \rho_G)\right]^{-1/2} \tag{1.9}$$

$$u_{LS}^{*} = u_{LS} \cdot \rho_L^{1/2} \left[gH(\rho_L - \rho_G)\right]^{-1/2} \tag{1.10}$$

Here, u_{GS} and u_{LS} are the *superficial* gas and liquid velocities respectively, H the channel height, g the acceleration of gravity and ρ the density. The subscripts G and L stand for *liquid* and *gas* respectively. Note that the dimensionless superficial velocity represents the ratio inertial force to hydrostatic force. The sum of the square roots of these dimensionless superficial velocities defines a limit, beyond which, flow reversal occurs:

$$u_{LS}^{*\,1/2} + u_{GS}^{*\,1/2} = 1 \tag{1.11}$$

A crucial point here is that Wallis derived this equation only taking into account the hydrostatic pressure of the liquid and the changes in gas pressure due to changes in concentration gradient which appear as a result of wave formation. Wallis did not consider the inertia of the fluids in the momentum equation. We will go back to this point at the end of this chapter, since this is a fact of vital importance that has been ignored over the past years.

The choice of dimensionless superficial velocities as equation parameters was not by chance. Wallis had been studying the problem of reversed flow experimentally using vertical tubes since 1961. He presented the following empirical correlation for the onset of reversed flow in vertical tubes in [67]:

$$m u_{LS}^{*\,1/2} + u_{GS}^{*\,1/2} = C \tag{1.12}$$

Here m ranges between 0.8 and 1.0 and the so-called *Wallis constant*, C, ranges between 0.7 and 1.0. Other investigators used equation (1.12) to correlate experimental data obtained mainly with vertical tubes, as for example Hewitt and Wallis (1963, [34]), Clift et al. (1966, [18]), Hewitt (1977, [33]) and Dukler and Smith (1978, [23]). Usually, values of m = 1 worked for vertical pipes and therefore the Wallis correlation for onset of reversed flow is often known as

$$u_{LS}^{*\,1/2} + u_{GS}^{*\,1/2} = C, \text{ with } C \text{ between 0.7 and 1.0} \tag{1.13}$$

However, these correlations are purely empirical, whereas equation (1.11) was obtained in 1969 *analytically*. It is evident that equation (1.11) is equivalent to equation (1.12) with m = C = 1, and that equation (1.13) is practically equivalent to the analytical Wallis equation (1.11) but permits a “correction” of the constant term.

Parallel to the work of Wallis, Pushkina and Sorokin (1969, [53]) investigated also countercurrent flow stability in vertical tubes and suggested a similar correlation in terms of the Kutateladze number. They correlated experimental data using equation (1.14) with m = 0 and C = 1.79.

$$K_G^{*\,1/2} + mK_L^{*\,1/2} = C \tag{1.14}$$

$$K_G^* = u_{GS}\left[\frac{\rho_G{}^2}{g\sigma(\rho_L - \rho_G)}\right]^{1/4} \tag{1.15}$$

$$K_L^* = u_{LS}\left[\frac{\rho_L{}^2}{g\sigma(\rho_L - \rho_G)}\right]^{1/4} \tag{1.16}$$

Note that the Kutateladze number is calculated with the superficial velocity of the corresponding phase and with the surface tension, σ, (equations (1.15) and (1.16)).

Actually, the relationship between the Kutateladze number and the dimensionless superficial velocity, defined by Wallis as $u_S{}^*$, can be expressed as follows:

$$K^* = D^* u_S{}^* \tag{1.17}$$

Where the *dimensionless diameter* D^* is given as

$$D^* = H \cdot \left[\frac{g(\rho_L - \rho_G)}{\sigma}\right] \tag{1.18}$$

Chung et al. [17] correlated reversed flow data using equation (1.14) with a value of m between 0.65 - 0.8 and C as a function of D^* (Equation (1.18)).

The main difference between these correlations is that, while the Wallis correlation includes the tube diameter, i. e. the channel height, the Kutateladze correlation does not. For tube diameters larger than 50 mm both correlations agree closely when predicting the gas velocity at reversed flow onset. However, for diameters less than 50 mm the predictions diverge. Jayanti et al. [36] performed in 1996 calculations using **C**omputational **F**luid **D**ynamics **C**odes (CFD codes) and concluded that the mechanism of reversed flow is different for small tube diameters than for large tube diameters, and therefore the use of correlations of the Wallis type is recommended. In fact, this result is not surprising, since the Kutateladze correlation was originally obtained to describe vertical thin liquid films, for which capillarity forces are dominant, and should not be used as a general correlation to predict reversed flow in horizontal channels.

b) Correlations to Predict CCFL

Throughout the past 30 years, a number of experimental and theoretical studies have been performed concerning CCFL in horizontal flow. In many experimental facilities, the onset of reversed flow coincides with the onset of slug flow and CCFL. This occurs if the ratio liquid-film-depth to channel-height (or pipe diameter) is small. In this case, for sufficiently high air velocities, wave amplitudes may be in the same order of magnitude as the channel height itself and slugging occurs at the onset of reversed flow. Therefore, special attention was focused on the transition from stratified flow to slug flow and many works intended to predict the onset of CCFL with correlations and theories which predict the transition to slug flow. They usually predict the transition to slug flow in terms of the void fraction and the dimensionless superficial gas velocity. Most of the existing theories and models have been reviewed by Kordyban (1990, [41]).

c) Experimental Studies with Countercurrent Horizontal or Near Horizontal Flow

Some of the first experiments in horizontal ducts can be found in the work of Wallis and Dobson (1973, [27]), who studied the stability of countercurrent flow of air and water. They observed experimentally, that a critical condition could be reached, at which rapid growth of waves occurred. Beyond this point, the liquid flow could no longer be sustained at its previous value, indicating the breakdown of stable countercurrent flow and the onset of reversed flow.

Gardner (1983, [28]) performed experiments with air and water for a wider range of flow conditions using a horizontal tube connected to a water chamber. He derived analytically the Wallis correlation [68] but instead of considering a finite stationary disturbance as Wallis did, he considered a vanishing finite disturbance. A new expression for the dimensionless superficial velocities was obtained:

$$u_{LS}^* = -y_0^2 / \ [y_0+R_d^2(1-y_0)]^{1/2} \qquad (1.19)$$

$$u_{GS}^* = R_d\,(1-y_0)^2 / [y_0+R_d^2(1-y_0)]^{1/2} \qquad (1.20)$$

Here, y_0 is the inlet liquid depth and R_d is the ratio of densities of the fluids employed:

$$R_d = \left(\frac{\rho_L}{\rho_G}\right)^{1/2} \qquad (1.21)$$

Reversed flow occurs if

$$u_{LS}^{*\ 1/2} + u_{GS}^{*\ 1/2} = 1\ ,\ u_{LS}^* \text{ and } u_{GS}^* \text{ obtained with equations (1.19) and (1.20).} \qquad (1.22)$$

This new derived Wallis correlation predicted well Gardner's experimental data and experimental data obtained by Richter et al. [58] as well as by Krolewski [42]. However, these two works were performed in a very different geometry than that used by Gardner: Richter and Krolewski carried out their experiments in a horizontal channel connected to an inclined riser whereas Gardner employed a horizontal tube. Since this correlation was only adopted by Ralph et al. (see below), it is difficult to know if the correlation can predict the onset of reversed flow not only in horizontal tubes but also in more complex configurations. An argument against this correlation is the fact that, in geometries with horizontal tubes connected to inclined risers, the onset of reversed flow occurs at lower superficial gas velocities than i. e. for vertical tubes ([58], [42]). Also the length of the horizontal tube and the inclination angle of the riser have an influence on the superficial gas velocity at onset of reversed flow ([51], [52]). The Wallis correlation succeeds in predicting a wide variety of geometries thanks to the variability of the parameters m and C. Since in equation (1.22) all parameters are fixed, the general applicability of this correlation is questionable.

Andreussi et al. [1] measured liquid hold-up as well as pressure drop in inclined, long tubes with countercurrent flow of air and water. The slope of the 17 m long bench could be adjusted in the range ±7%. The liquid hold-up was measured by conductance cells. They observed experimentally, that the onset of reversed flow is determined by the growth of a hydraulic jump at a certain position of the tube. Moreover, the effect of the inlet liquid height, of the calming section length and of the total tube length was investigated. It is reported that, if the liquid layer at the entrance is wavy, premature reversed flow happens close to the liquid inlet.

In 1987 Ralph et al. [55] investigated horizontal countercurrent flow in a short tube connected to two vessels. The tube length was 500 mm and its diameter 50 mm. Two types of flow reversal are identified: *Low head flow reversal* and *high head flow reversal*. Low head flow reversal occurs, if, in an initial stratified countercurrent flow, the gas flow rate is increased in small steps and a situation is reached, where the liquid discharge rate falls suddenly. The liquid film turns to a wavy film and a head builds up in the liquid supply vessel. From this point on, the initial liquid discharge rate cannot be obtained by reducing the gas flow rate to its previous value: hysteresis is observed. High head flow reversal conditions correspond to those conditions for which stratified flow is restored; the gas flow rate is reduced considerably below its initial value. Other authors termed this situation as *unflooding*. Ralph et al. showed that high head flow reversal experimental data can be predicted with equation (1.22) (presented in [28] by Gardner), whereas a new condition is derived for low head flow reversal based in the growth of a small disturbance:

$$\frac{u_{LS}^{*\,2}}{2A_1^{\,2}} + \frac{(A_2 - A_1)^2 u_{GS}^{*\,2}}{(1 - A_1)^2 (1 - A_2)} = h_2 - h_1 \tag{1.23}$$

Subscript 1 denotes a position situated in the critical flow of the liquid (inlet side of the disturbance) while subscript 2 denotes a position in the disturbance. The height of the gas flow path at position i is represented by h_i, the fractional area of the gas at position i by A_i. The terms h_1 and h_2 are taken from experimental data obtained in [55] and employed to calculate A_1 and A_2 respectively. Once these parameters are calculated, equation (1.23) gives u_{GS}^* as a function of u_{LS}^*. Low head flow reversal data obtained in this report and those obtained by Krolewski [42] are represented in a diagram $u_{LS}^{*\,1/2}$ versus $u_{GS}^{*\,1/2}$ together with the new curve obtained with equation (1.23) and the theory presented by Wallis (equation $u_{LS}^{*\,1/2} + u_{GS}^{*\,1/2} = 1$, u_{LS}^* and u_{GS}^* calculated with (1.9) and (1.10)). Both theories agree for values $u_{LS}^{*\,1/2} < 0.5$. From this value on, the new theory presented by Ralph et al. yields better agreement, although Wallis leads also to acceptable results.

Choi and No [14] carried out experiments in nearly horizontal pipes with air and water. The parameters investigated were pipe diameter, end geometry and inclination angle. The test section, with a length of 2160 mm, was connecting two identical vessels. They observed experimentally the existence of a hydraulic jump-induced flow reversal, as Siddiqui et al. [59] also observed. Reversed flow is initiated by the sudden growth of waves which already exist in the pipe before onset of reversed flow. The explanation given by the authors is that waves are created in the subcritical region by the air shear force and continue to grow until reversed flow occurs at a certain threshold gas flow rate. The transition criterion for reversed flow is approximately consistent with that of slug flow, since once the hydraulic jump occurs, the liquid depth increases suddenly and the authors reported onset of slugging depending on the pipe inclination angle. Experimental data is correlated with the Wallis type equation:

$$0.64 \cdot {u_{LS}^{*}}^{1/2} + {u_{GS}^{*}}^{1/2} = 0.58 \tag{1.24}$$

And the relationship between the void fraction and the critical gas velocity is

$$u_{GS}^{*} = 0.36 \cdot {\alpha_G}^{3/2} \tag{1.25}$$

Nevertheless, for inclination angles higher than 0.69° and high liquid flow rates ($ {u_{LS}^{*}}^{1/2} \geq 0.4$), flow reversal sets in at the liquid entrance without previous occurrence of a hydraulic jump. This is not surprising, since the liquid is accelerated by gravity if the pipe is inclined. As a result, the occurrence of a hydraulic jump is inhibited.

The effect of steam condensation in nearly horizontal flow was investigated by Chun and Yu [16] in two experimental series of 17 tests each (17 tests with water-air and 17 with water-steam). The test section, with a pipe diameter of 0.083 m and a length of 2.2 m, was inclined 0.25° for air-water tests and 0.5° for steam-water tests. All experiments were carried out under atmospheric pressure conditions. It was observed, that the breakdown of stratified flow lead to slug flow and a new criterion to predict the gas velocity at the transition was derived analytically taking into account the effect of condensing steam. The critical velocity $u_{G,crit}$ obtained is given by

$$u_{G,crit} = \sqrt{\frac{\rho_L g H_G \cos\vartheta \cdot C_{P,crit}}{\rho_G}} \cdot \frac{\sqrt{\left(\frac{4}{\pi} + f_i\right) \cdot (1 - C_C) + C_C - 1}}{\left(\frac{4}{\pi}\right) + f_i - 1} \tag{1.26}$$

Where the effect of steam condensation is included in the dimensionless condensation factor C_c defined as

$$C_C^{*} = \frac{\rho_G}{\rho_L} \frac{3.72 \cdot {u_{S,crit}}^2}{g H_G \cos\vartheta \cdot C_{P,crit}} \tag{1.27}$$

The average velocity of the condensing steam, $u_{S,crit}$, can be estimated from heat balance at the interface using the interfacial heat transfer coefficient proposed by Kim (1983, [38]). $C_{p,crit}$ is a geometric factor, equal to unity for duct flow. ϑ is the inclination angle of the pipe, H_G is an equivalent gas height, calculated as if the liquid was in form of a smooth film. g is the acceleration of gravity and ρ_L and ρ_G stand for liquid and gas density respectively. The interfacial friction factor f_i is estimated using the Lee correlation, [45]. It is evident that this model is complex and it can be only solved iteratively. Experimental data obtained with air-water and steam-water is compared graphically together with the predictions by the model presented and those obtained with a Wallis type correlation ($m u_{LS}^{*\,1/2} + u_{GS}^{*\,1/2} = C$, m = 0.60 and C = 0.52, best fit). The criterion derived to predict the onset of slug flow predicts well the experimental data but tends to overpredict the dimensionless superficial velocity of the gas for low liquid velocities, while the Wallis type correlation fits the data in the entire range of flow conditions, even data obtained with steam. In general, for a given water flow rate, the superficial velocity needed for the onset of CCFL is slightly larger for steam than for air, but can be predicted well by a Wallis type correlation, since the predominant effect is the change in density ratio if steam is used instead of air, and the Wallis type correlations take into account the effect of density. Thus, the complexity of this correlation cannot be justified, since acceptable results are obtained with the much simpler Wallis correlation.

d) Behaviour of ECC in Postulated LOCAs in Simulated PWRs

Reflux Condensation Mode

Throughout the eighties, several works were published concerning the reversed flow onset problem in nuclear safety, specifically, concerning the so-called *reflux condensation mode* during a LOCA in a LWR. Hereby, condensation is occurring in the steam generator tubes and a column of liquid builds up in the upper part of the tubes. This water may flow back through the hot legs into the reactor core against the steam flow from the upper plenum and contribute to core cooling and reflooding, provided, no CCFL or reversed flow happens in the hot legs (see Fig. 1.11).

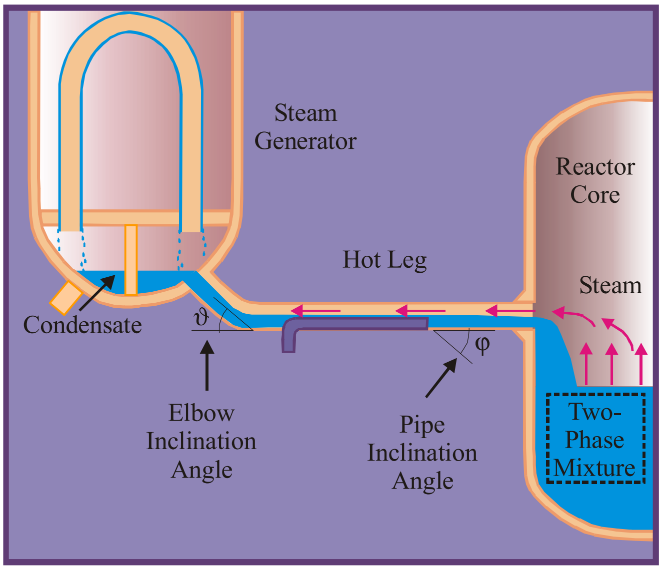

Fig. 1.11. Cooling by means of reflux condensation.

Most of these studies were based on experiments performed in test facilities where the geometric particularities present in nuclear systems were reproduced partly or completely (horizontal hot leg with steam generator and an elbow connected to it). Empirical correlations are often presented in these studies and their validity is argued by comparing with other authors' data. Although they do not have general validity for horizontal countercurrent flow due to the empirical nature of the work done and the specific geometries used, they represent a very interesting contribution for simulated PWR downcomer geometries in reduced scales and the most important works will be summarized within next paragraphs.

In 1978, Richter et al. [58] examined the countercurrent flow of air and water in a scaled down PWR hot leg during reflux phase and correlated reversed flow data with the Wallis correlation

$$u_{LS}^{*\,1/2} + u_{GS}^{*\,1/2} = 0.7 \tag{1.28}$$

They observed no liquid delivery for gas superficial velocities higher than 21 m/s. Richter et al. suggested that the effect of droplet entrainment by the gas should be considered when estimating the dimensionless superficial velocity of the gas and proposed a modified Wallis correlation for the case of considerable liquid entrainment by the gas

$$u_{LS}^{*\,1/2} + u_{GS,E}^{*\,1/2} = 0.825 \tag{1.29}$$

Here the dimensionless superficial velocity of the gas, $u^*_{GS,E}$, includes the effect of the entrained droplets and is defined as

$$u_{GS,E}^{*} = \frac{\left[\alpha_G \cdot \rho_G + (1-\alpha_G)\cdot \rho_L\right]^{1/2} u_{GS}}{\left[g \cdot D(\rho_L - \rho_G)\right]^{1/2}} \tag{1.30}$$

Where α_G is the void fraction, D is the pipe diameter and ρ_L and ρ_G are the liquid and gas density respectively. For the range of conditions studied with entrainment, no liquid was delivered for gas superficial velocities higher than 15 m/s.

Krowlewski (1980) measured flooding limits in air-water countercurrent flows in horizontal tubes connected at the inlet to either 45° or 90° elbows. These experiments showed that the gas velocity necessary to produce flow reversal is much smaller in an elbow than in a vertical tube [42], so that the correlation of Wallis (equation (1.11)) overpredicts the onset of reversed flow. Additionally, hysteresis was observed when intending to return to the initial flow conditions and restore stratified flow by reducing the gas flow rate (*unflooding*).

Siddiqui et al. [59] performed experiments on reversed flow limits with countercurrent air-water flow. The geometry chosen in their work consisted of a horizontal or slightly inclined pipe connected with a vertical leg through an elbow. Visual observations showed, that flow reversal was triggered by the formation of a hydraulic jump leading to wave formation and slugging at the horizontal pipe close to the bend. These experiments were carried out using pipe diameters between 36.5 and 47 mm and ratios of length-to-diameter between 24 and 95. Also the radius of the elbow was varied. The results showed that the Wallis correlation (C = 0.7, eq. (1.13)) leads to overprediction of the dimensionless superficial velocities at flow reversal, due to the presence of the elbow. Neither the correlation proposed by Taitel and Dukler [64] was able to predict the onset of slug flow. On the other hand, from the results obtained it can be concluded that, the longer the horizontal section, the lower the velocities necessary for the occurrence of flow reversal. A larger bend radius of curvature also reduces the gas flow rate at reversed flow. The diameter of the pipe influences slightly the superficial velocities at reversed flow. An empirical criterion for the onset of reversed flow is presented from experimental data:

$$u_{GS}^{*} = u_{GS,C}^{*} \cdot \alpha_G^{3/2} \tag{1.31}$$

α_G is the void fraction at the crest of the hydraulic jump and $u_{GS,C}^{*}$ is a critical gas velocity, with a constant value between 0.2 and 0.5 depending on the geometry used. Additionally, a criterion to predict the onset of totally reversed flow is derived from experimental data obtained with different bend radii of curvature and pipe diameters:

$$\sqrt{u_{GS}^{*\,1/2}} = 0.45 \tag{1.32}$$

The authors observed that, beyond totally reversed flow limit, liquid was still present in the horizontal section but did not flow out of the gas inlet.

Ardron and Banerjee [3] presented a correlation based on a model that assumes that reversed flow coincides with the onset of slugging in the horizontal pipe, close to the bend. They used equation (1.31) to predict the void fraction at the crest of the jump, α_G, assuming $u_{GS,C}^{*} = 0.2$, and introduced this solution into a set of one-dimensional equations derived from momentum balance between gas and liquid. The set of equations was then solved numerically. Since this method is complex, Ardron and Banerjee proposed an empirical correlation that represents with reasonable accuracy the flow reversal curves obtained analytically:

$$u_{GS}^{*\;1/2} = 1.444 - 0.004\lambda - \cosh\left(\lambda^{0.057} \cdot K^{-0.020} \cdot \left(u_{LS}^{*\;1/2}\right)^{0.70}\right) \tag{1.33}$$

Where

$$\begin{aligned} \lambda &= \frac{\ell \cdot \left(\mathrm{Re}^{*}\right)^{-0.2}}{D} \\ \mathrm{Re}^{*} &= \frac{D}{\nu_G}\sqrt{\frac{gD(\rho_L - \rho_G)}{\rho_G}} \\ \mathrm{Fl}_P{}^{*} &= \frac{\nu_G}{\nu_L}\sqrt{\frac{\rho_G}{\rho_L}} \end{aligned} \tag{1.34}$$

ℓ and D are the length and the diameter of the horizontal pipe respectively, ρ the densities and ν the kinematic viscosities of liquid (subscript L), and gas, (subscript G). The data obtained by Siddiqui et al. [59] and that obtained by Krolewski [42] were compared with the model. For the data of Siddiqui et al. only for certain experiments a reasonable prediction was obtained whereas data obtained by Krowleski was overpredicted.

Ohnuki, [52], performed experiments in tubes connected to inclined risers (simulating the shape of a PWR hot leg). The effect of a wide range of geometric parameters, such as tube diameter, horizontal tube length and length of the inclined riser, was tested. The angle of the inclined riser was either 40° or 45°. The Wallis correlation, $m u_{LS}^{*\,1/2} + u_{GS}^{*\,1/2} = C$, equation (1.12), predicted well the experimental data but it was observed, that the Wallis constant C was a function of the geometry employed. Therefore, Ohnuki developed an empirical correlation to estimate the value of C in equation (1.12) including the effect of length-to-diameter ratio in the horizontal tube, H/D, the shape of the upper exit of the riser (elliptical, circular) and the length of the inclined riser, I:

$$C = \begin{cases} \ln\left[(H/D)\cdot(1/I)\right]^{-0.066} + 0.81 & \text{elliptical tube shape} \\ \\ \ln\left[(H/D)\cdot(1/I)\right]^{-0.066} + 0.88 & \text{circular tube shape} \end{cases} \tag{1.35}$$

He correlated experimental data using equation (1.12) with m = 0.75 and C calculated from (1.35). Also, data obtained by Richter et al. [58] was correlated with good agreement. However, no data corresponding unsteady flow with water plugging could be correlated.

Later, Ohnuki et al. [51] investigated scale effects on flow reversal by comparing data obtained in a small-scale experiment and data obtained in the UPTF full-scale experiments [70]. They intended to correlate these flow reversal data sets by means of the Wallis equation (1.12) but calculated C as proposed in [52] (C obtained with equation (1.35), see above). However, the Wallis correlation estimated in this way was not able to predict full-scale data with accuracy, and a new model based in the envelope theory was proposed. The model must be solved numerically and an empirical correlation for the void fraction at the gas inlet and at the gas outlet in the horizontal section is needed.

Lopez de Bertodano (1994) derived a model to be implemented in numerical codes to predict onset of reversed flow and hysteresis effects during reflux core cooling in the hot leg of PWRs. He improved the correlation of Ishii and Mishima for onset of slug flow and proposed that onset of reversed flow occurs if:

$$u_G - u_L > 0.487\left[\frac{\left(\dfrac{\rho_L - \rho_G}{\rho_G}\right)\cdot gD\cos\varphi\cdot\alpha_G}{\dfrac{8}{\pi}\left[\dfrac{y}{D}\left(1-\dfrac{y}{D}\right)\right]^{1/2}}\right]^{1/2} \tag{1.36}$$

Where the subscripts L and G stand for liquid and gas, u is the mean velocity, ρ the density, φ the angle between the horizontal pipe and the bend, α_G the void fraction, y the liquid depth, D the pipe diameter and g the acceleration of gravity. This correlation was combined with a void fraction profile along the pipe obtained with one-dimensional two-fluid model equations [48]. Krolewski's data were used to validate the model and then, the model was used to predict full-scale data used by Ohnuki et al. [51]. A data fitted correlation is proposed by Lopez de Bertodano:

$$0.798 \cdot u_{LS}^{*\ 1/2} + u_{GS}^{*\ 1/2} = 0.619 \qquad (1.37)$$

Furthermore, Lopez de Bertodano pointed out, that hysteresis is not an issue in prototypical refluxing conditions, and that Gardner's correlation for unflooding is therefore not necessary for prototypical conditions.

Wang and Mayinger [69] performed numerical simulations of flow phenomena in the hot leg of PWR during SB-LOCA to show, that numerical simulation of complex thermal-hydraulic processes provides an alternative to the reactor safety study. However, they affirmed, that it is essential to choose a three-dimensional code due to the multidimensional nature of the flow in the hot leg close to the ECC pipe region. Cocurrent and countercurrent flow of air and steam was simulated under the boundary conditions of UPTF Test A2 and Test 11 for natural circulation mode and reflux condensation mode [22]. Hereby, it is taken into account whether the liquid flow regime is subcritical or supercritical and if flow reversal is about to occur. The onset of flow reversal was estimated with the correlation of Richter et al. (equation (1.28), [58]). The interfacial friction factors were calculated with the correlations of Lee and Bankoff [44] and Ohnuki [52]. The results showed good agreement with UPTF experimental data.

Wongwises ([71], [72] and [73]) investigated the effect of horizontal pipe length with air and water on reversed flow. Also different bend angles and water inlet sections (porous inlet and inner pipe inlet) were tested. Liquid hold up was measured by conductance cells in the horizontal pipe (70 mm before the bend). The system pressure was kept constant at 130 kPa. For intermediate water flow rates, the occurrence of a hydraulic jump was observed before flow reversal sets in. For high flow rates, slugs formed at the end of the pipe and were pushed upstream by the air, yielding reversed flow. With increasing horizontal pipe length, the air velocity at which reversed flow occurred decreases for the whole range of water flow rates. A larger inclination angle resulted in acceleration of the liquid by gravity and decrease of the liquid energy with an earlier jump. Therefore, a lower air flow rate was needed to cause flow reversal. The onset of reversed flow happens for low liquid flow rates if

$$u_{GS}^{*} = 0.82 \cdot \alpha_G^{\ 2.75} \qquad (1.38)$$

α_G is the void fraction at flow reversal. Note, that this correlation is empirical and similar to that presented by Siddiqui et al., [59]. Wongwises predicted the void fraction with equation (1.38) and solved iteratively the void fraction dependant one-dimensional equation for two-phase critical flow to determine u_{LS}^{*} and u_{GS}^{*}. However, a comparison with experimental results showed only good agreement for low liquid flow rates, since equation (1.38) cannot be extrapolated to other conditions, for which other mechanisms may lead to onset of reversed flow.

Takeuchi et al. [65] investigated the effect of pipe inclination on reversed flow onset. CCFL in vertical, slightly inclined and horizontal pipes was studied. This kind of pipes is present in typical PWR surge lines connecting the pressurizer to the cold leg. The pressurizer drain rate is determined by the most limiting CCFL location in the surge line. For horizontal sections, the equations presented by Taitel and Dukler [64] to represent cocurrent stratified flow were employed and adapted to the countercurrent case. A force balance equation for the interfacial force was obtained as a function of superficial velocities of liquid and gas and of the void fraction. Eliminating the void fraction, a critical curve for CCFL is obtained. This was done also by Barnea et al. (1986, [11]), but the interfacial friction factor employed was not appropriate for steam. For vertical elbows, a qualitative consideration of the straight pipe with increasing inclination was used considering the gravity force, the centrifugal force and the surface tension to stabilize the stratified flow. For vertical sections, the reversed flow correlation in terms of the Kutateladze number was employed. After several calculations, it is concluded that the limiting CCFL location is the vertical section of the pressurizer surge line, so that the pressurizer drain rate is controlled by the vertical CCFL.

The effect of fluid properties on reversed flow onset was investigated by few authors. One of the most significant works is that reported by Zapke and Kröger, [75]. Experiments were conducted with air, argon, helium, hydrogen, water, methanol, isopropanol and aqueous methanol solutions in a vertical and inclined tube (60°). The findings clearly show that fluid density influences strongly the velocity of gas at the onset of flow reversal. Additionally, the effect of liquid viscosity is higher than that of surface tension and no effect could be observed on flow reversal varying the viscosity of the gas. The Wallis type correlation was improved as follows:

$$m \cdot u_{LS}^{*\,1/2} + u_{GS}^{*\,1/2} = k \cdot Z_L^{\,n} \tag{1.39}$$

Here m, k and n are constant values that depend, on one hand, on the type of gas inlet (sharp-edged or tapered) and on the other hand, on the tube inclination (vertical or inclined at 60°). The parameter Z_L accounts for liquid properties and is defined as

$$Z_L = \frac{\sqrt{D\rho_L\sigma}}{\mu_L} \tag{1.40}$$

Where D is the pipe diameter, ρ_L is the liquid density, σ the surface tension, μ_L the liquid viscosity. For data obtained with water, the authors did not consider the parameter Z_L and correlated data with the classical form of the Wallis correlation ($mu_{LS}^{*\,1/2} + u_{GS}^{*\,1/2} = C$). Values of m between 0.4 and 0.6 were employed together with values of C between 0.8 and 1.0. Furthermore, data obtained by others was correlated with the dimensionless parameters $u_{LS}^{*\,1/2} / Z_L^{\,n}$ and $u_{GS}^{*\,1/2} / Z_L^{\,n}$ (with n = 0.05).

ECC-Injection

The main concern of most of the works presented above is reversed flow in hot leg during reflux core cooling. There are few works dealing with the problem of reversed flow during ECC injection in the hot leg.

Concerning numerical simulations, early work was done in 1981 by Daly and Harlow [20], who derived a computer model to predict complete ECC flow reversal in the hot leg of a typical PWR geometry, (see chapter 1.1.3: Hot Leg Injection). The calculations were performed representing the two-phase pipe flow of the hot leg by two-phase flow in a rectangular channel, as shown in Fig. 1.12.

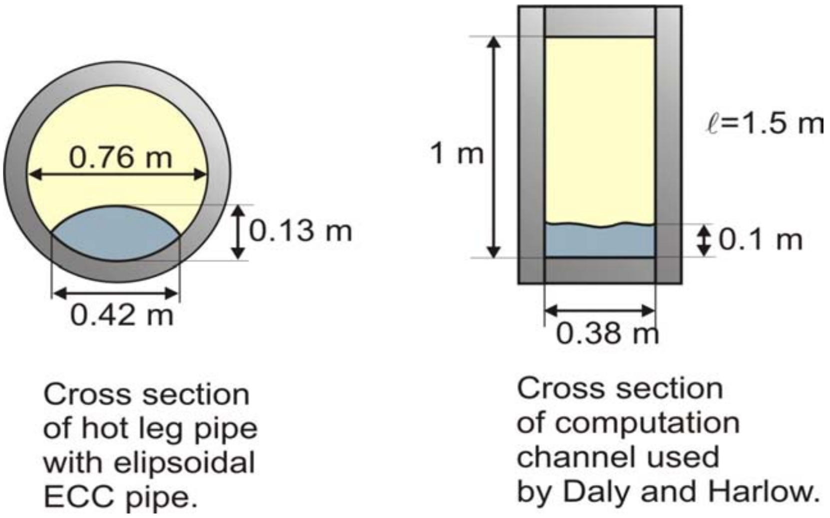

Fig. 1.12. Comparison between typical hot leg pipe geometry and computation channel used by Daly and Harlow [20].

The channel length employed was 1.5 m. Subcooled water at a temperature of 307 K was injected counter saturated steam with a velocity of 7 m/s in the channel. The average pressure in the hot leg was 0.6 MPa (corresponding saturation temperature is 431 K). Under these conditions, Daly and Harlow calculated a maximum incoming steam velocity of 17 to 30 m/s against which, ECC water could penetrate to the upper plenum. Nevertheless, the validity of their results was estimated with a sensitivity analysis but no experimental data supported the calculations.

Full-scaled integral experiments concerning emergency core cooling were performed in the German **U**pper **P**lenum **T**est **F**acility (UPTF). Results are reported in [21] by Damerell and Simons. The tests and analysis covered the following ECCS modes: cold leg injection, combined injection (cold leg and hot leg injection), upper plenum injection and downcomer injection. A commented report concerning calculation of such phenomena with CFD-Codes can be found in [40]. Here, Kolev et al. discuss the use of 2-dimensional codes, since the transient redistribution of the liquid in film and droplets cannot be predicted with accuracy using two velocity fields. Therefore, the use of a computer code dealing with three velocity fields is recommended. It is pointed out, that the analysis of such flow phenomena with numerical codes is limited by the lack of local experimental data on ECC injection in the literature.

The geometry of the hot leg used in these experiments is shown in Fig. 1.13. A secondary pipe is employed to inject saturated water in the core, with a cross section as shown in section A-A. The end of this secondary pipe is positioned at a distance of

1530 mm from the RPV wall. Throughout this distance, water and steam flow countercurrently if stable stratified countercurrent flow can be established. However, UPTF tests showed that water plugs form and collapse periodically in the hot legs, due to steam condensation by the high flow of subcooled water, and that CCFL occurs. Consequently, ECC delivery to the upper plenum through the hot leg fluctuates strongly. At high steam flow rates, the countercurrent flow of water and steam is partially reversed and water is carried over by the steam to the steam generator, where it is evaporated by heat transfer from the secondary side. Also, steam-ECC interaction in the hot leg can influence behavior in the cold leg and vice versa.

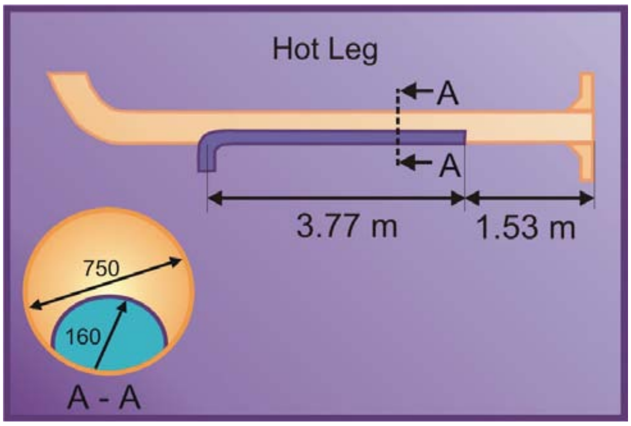

Fig. 1.13. Hot leg injection arrangement employed in the UPTF experiments.

Comparison of UPTF results and CCFL correlations obtained from small-scale facilities indicated that downflow was significantly higher at the full-scale UPTF than at a small-scale facility. This beneficial effect at large-scale is explained by multidimensional water distribution and flow patters, i. e., distinct breakthrough zones.

Since assessment of existing reversed flow onset correlations from literature using UPTF experimental results revealed that extrapolation to full-scale is not appropriate, [62], a new equation was developed, [29]. This correlation is an addition of a Wallis-type correlation and a Kutateladze-type correlation. However, the correlation is just used to predict CCFL at the tie plate.

1.4.3 Summary

In chapter 1.4.1 and 1.4.2 the most significant works dealing with properties and stability of stratified countercurrent flow done in the past were presented. The following conclusions can be extracted from the literature review:

- Stratified countercurrent flow of liquid and gas in horizontal pipes or channels is only possible for a given range of liquid and gas flow rates.

- For a given liquid mass flow rate, there exists a threshold gas mass flow rate that causes the transition from stratified countercurrent flow to reversed flow. Once reversed flow sets in, a reduced liquid delivery rate is observed and an increase of liquid mass flow rate does not increase liquid delivery due to CCFL. In some studies a hysteresis effect was observed when reducing the gas flow rate to restore stratified countercurrent flow.

- Several authors observed wavy flow before the transition to reversed flow occurs. Also onset of atomization in the region where reversed flow occurs was remarked in many cases.

- Moreover, it was reported by many authors that a hydraulic jump occurs somewhere in the flow right before reversed flow sets in. The term *hydraulic jump-induced reversed flow* is even used by some authors.

- The conditions for which wavy flow or hydraulic jump occurs in horizontal flow was only investigated for free surface flow. There are no flow regime maps for horizontal countercurrent flow in closed channels or pipes that take into account these possible transitions, although there is clear experimental evidence of their existence.

- Regarding prediction of reversed flow, two types of correlations are used: Wallis type correlations and Kutateladze number type correlations. Since there is verification that the Kutateladze correlation cannot predict with accuracy reversed flow onset in small pipe diameters, the most used correlation to predict the transition to reversed flow is the Wallis correlation. Different versions of this correlation can be found in the literature. Some of them are absolutely empirical whereas others are based on one-dimensional momentum and energy equations for countercurrent stratified flow. However, the latter usually need significant assumptions or empirical relationships, for example between the void fraction and the superficial velocity of the gas at reversed flow onset. Furthermore, the solution of these sets of equations can often only be obtained iteratively.

- The limitations of the Wallis correlation have been ignored throughout the literature: the Wallis correlation was obtained for stratified horizontal flow of two fluids without considering the inertia of these fluids. This means, that the correlation can only be applied to subcritical flows, where the inertial term is negligible. The work presented here will analyze, for the first time, the Wallis correlation taking into account this requisite.

- There exist also correlations which account for the effect of pipe geometry (horizontal, inclined, vertical, pipe length, pipe diameter, etc). However, most of these correlations fail in predicting full-scale data.

- The effect of fluid properties or steam condensation was less studied. Concerning ECC hot leg injection, this is a field, where further work is needed.

- Other studies observed that the transition to reversed flow occurs in the form of slug flow leading to CCFL. It seems that in these cases, waves grow with amplitudes of the same order of magnitude like the channel height (or pipe diameter). This fact leaves open the question, whether the ratio liquid-depth to channel-height influences the onset of reversed flow.

- In view of the fact, that slug flow is observed during the transition from stratified countercurrent flow to reversed flow, some authors intended to predict the onset of reversed flow by means of correlations that predict the transition from stratified to slug flow. There is no evidence, that these correlations predict the onset of reversed flow much better than the Wallis correlation.

- The thermal-hydraulic response of a PWR primary coolant system to a LOCA and the performance of the ECCS have been areas of research interest for two decades. The number of works related to reversed flow onset in geometries similar to that of a PWR hot leg has enormously increased. However, experimental work has focused mainly on the scenario reflux condensation mode. Hot leg injection by means of the ECCS was less investigated. The only data available on reversed flow during hot leg injection were those obtained in the UPTF experiments. Since only integral experiments were carried out in the test facility, no detailed information about flow regimes in the hot leg and their influence on water delivery rates is available in the literature. Additionally, no analytical work was performed from the point of view of prediction of reversed flow in the hot leg.

- Estimation of flow regimes and flow stability in the hot leg during ECC injection by means of CFD-Codes is still very limited, partly, due to the lack of experimental work with local measurement of flow parameters to provide data for model development and validation.

1.5 Thesis Objectives

As it turned out, there exist plenty of studies concerning stability of horizontal and horizontal to inclined countercurrent flow. However, most of the works mentioned above have concentrated on special geometries (horizontal flow connected to an elbow and inclined riser), and since they are predominantly empirical, their general application is questionable. Few works investigated horizontal countercurrent flow in pipes and ducts and there is a lack in understanding the physical mechanisms that yield flow reversal. Results of similar experiments deviate considerably from author to author, partly, because the Wallis correlation is applied without considering its real range of applicability, i. e. subcritical flow.

For this reason, the WENKA test facility was built at Forschungszentrum Karlsruhe GmbH (Germany). The name **WENKA** is an acronym for the german expression ***W**asser und **En**trainment* **Ka**nal, what means *Water and Entrainment Channel*. Horizontal stratified countercurrent flow is investigated, mainly focusing on the problem of stability during hot leg injection. The principal objective of WENKA is to provide and experimental data base to derive physical models. Additionally, local experimental data can be integrated in advanced computer codes to enhance them for their application to the reactor case. As mentioned before, there are up to now no investigations on hot leg injection providing such experimental data. Neither the flow regimes nor their influence on coolant delivery are well known.

Experiments are carried out to investigate the fluid dynamics of horizontal countercurrent flow and its stability. The geometry chosen is analogous to that of a PWR hot leg: a horizontal channel with a parallel plate to model the secondary pipeline used to perform hot leg injection. The inclined riser leading to the steam generator is not modeled. Neither the effect of temperature and pressure are considered in this experimental series, since the main objective is to get acquainted with physical mechanisms yielding reversed flow. Therefore, water and air are employed in this study as cold simulants.

The experimental program in the framework of the WENKA project can be divided in two parts, a series of integral measurements to obtain an overview of the flow phenomena and a series of local measurements to obtain an experimental data bank and to support the conclusions extracted from the integral experiments.

a) Integral Measurements

- Extreme flow conditions are present in nuclear accident scenarios and the effect of having countercurrent gas cannot be neglected if accurate estimations about flow regimes are desired. Consequently, the results obtained in the last decades for open channel flow regarding the transition from supercritical to subcritical flow in form of a hydraulic jump, will be extended to the case of stratified countercurrent flow of liquid and gas in closed horizontal channels. Identification of flow regimes in countercurrent flow and their limits of stability will be assessed. Flow phenomena at the transition points will be studied.

- The onset of reversed flow will be investigated for a wide range of flow conditions. The effect of the ratio water-depth to channel-height will be taken into account. Flow parameters that can be used to predict, in an either empirical or analytical way, the transition to reversed flow will be identified.

- The effect of CCFL will be investigated by measuring liquid delivery rates for different reversed flow conditions. Correlations to predict coolant delivery for an extensive range of conditions will be proposed.

b) Local Measurements

- Measurement of air and liquid velocity profiles will be performed by means of **P**article **I**mage **V**elocimetry (PIV) for selected experiments.

- The liquid depth along the channel and the interface morphology will be measured for selected experiments by means of digital recording of the flow conditions and posterior digital analysis of the images. With these digital techniques and special software, the position of the interface throughout the channel will be obtained. Furthermore, the morphology of wavy flow will be analyzed. Assessment of wave velocities will be performed.

2 Description of the Test Facility and Flow Regimes Observed

2.1 Experimental Set Up

The test facility is basically designed to establish countercurrent flow of air and water in an experimental channel with conditions similar to those present in a PWR during hot leg injection. Principally the set up consists of a closed water loop and an air supply line (see Fig. 2.1).

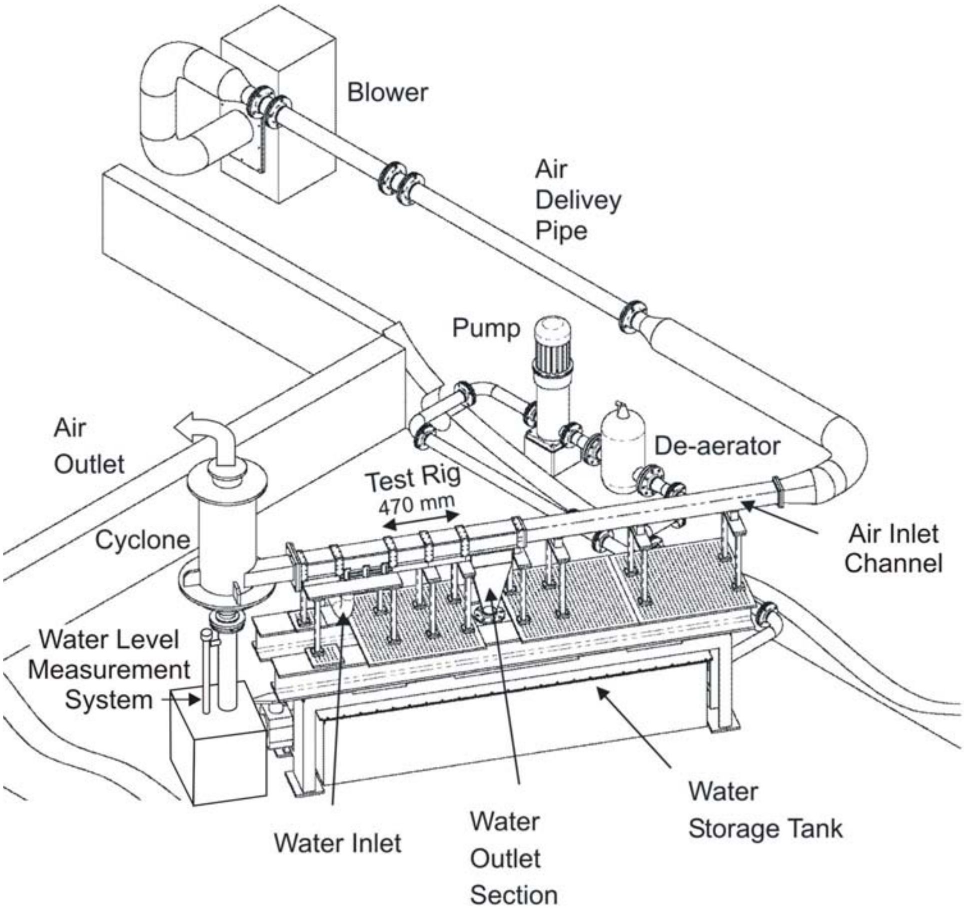

Fig. 2.1. General view of the WENKA test facility.

Demineralized water is employed. The water is de-aerated and filtered using a filter with a mesh fineness of 5 μm. Instead of saturated steam, ambient air is employed. The air is filtered before being delivered to the test section.

A centrifugal pump delivers up to 150 l/min of liquid to a water inlet apparatus that models the ECC secondary pipe in a PWR hot leg. At the inlet, the water is injected into the test section countercurrently to the air. At the end of the test section, the water is dumped to a water outlet section that models the reactor core (see Fig. 2.2).

Air is supplied by a blower with an air operation range of 0.26 kg/s and an operation pressure of up to 0.8 bar. The air passes through an eddy flow meter and enters into an inlet channel with a length of 1.655 m. The cross section of this inlet channel is identical to that of the test section. The air inlet channel is designed to ensure unperturbed air flow entering into the test section, and therefore a length-to-height ratio of 20 was chosen. Additionally, a honeycomb-like assembly is placed at the entrance of the inlet channel to uniform the air flow and break possible turbulence eddies.

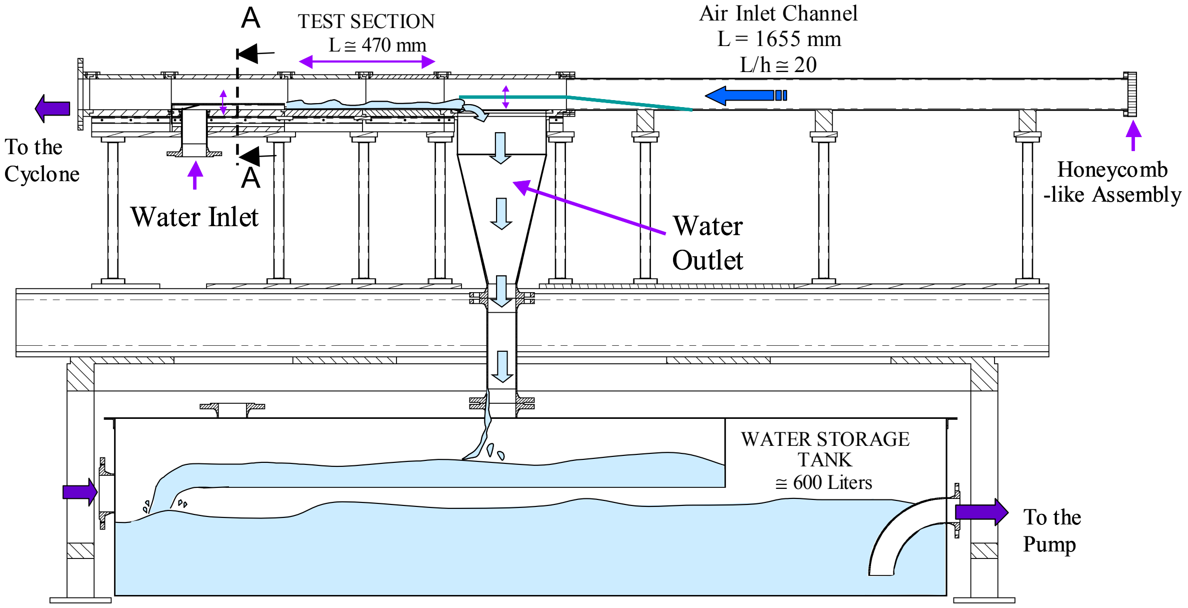

Fig. 2.2. Detail of test section with water inlet and outlet and air inlet.

The air is injected countercurrently to the water at the end of the inlet channel. A this position there is a second plate that can be adjusted manually to the water height. In this way, the air flows into the test section smoothly.

After having passed the test section, the air flows into the cyclone before being released to the atmosphere. If water is carried over by the air throughout the test section in form of entrained droplets or if reversed flow sets in, the mixture of air and water is separated in the cyclone. For selected experiments, the mass flow rate of separated water was measured and then the water was delivered back to the storage tank. For all other experiments the separated water was sent directly to the storage tank.

The test section, with a length of 470 mm and a cross section of 110 x 90 mm, consists of a rectangular channel made of transparent glass to permit visual observation of the flow pattern and measurements with laser based techniques. Water is pumped from a storage tank to the water inlet section, flows through the test section and at the end of it, is dumped back to the storage tank.

Fig. 2.3 shows a cross sectional view of the water inlet section at position A-A (given in Fig. 2.2).

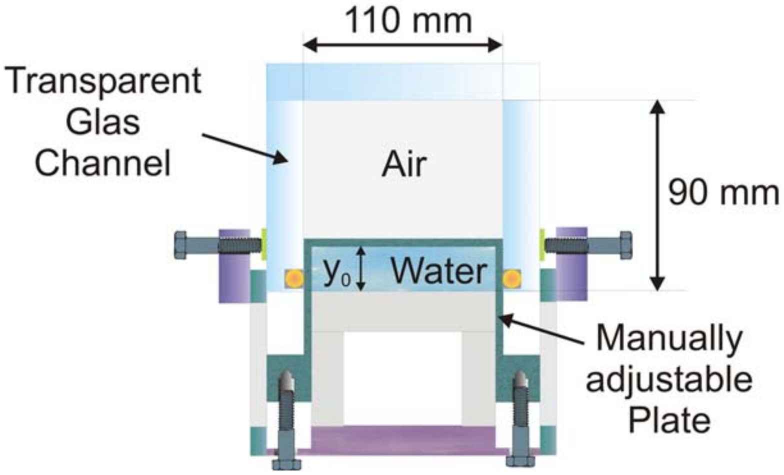

Fig. 2.3. Water inlet depth adjustment (cross sectional view).

The water inlet section is provided with a manually adjustable plate to set the inlet liquid depth in the channel, y_0, by adjusting a set of screws placed at the bottom of the channel. In this way, the influence of the ratio liquid-depth to channel-height, y_0 / H, can be investigated. Water film heights from 2 to 20 mm can be studied corresponding to ratios liquid-depth to channel-height ranging from 0.022 to 0.22.

2.2 Experimental Procedure

2.2.1 Measurement of Flow Parameters

A schematic diagram of the test facility is shown in Fig. 2.4 . During the experiments, several flow parameters were acquired, as for example the water volumetric rate flowing through the channel, the air volumetric flow rate injected into the channel, air pressure and temperature at different positions as well as water temperature. The data acquirement system measured each flow parameter with a sampling rate of 1 kHz. From the measured values, a mean value was averaged and values differing more than permitted by the Chauvenet's criterion [56] were rejected. After this procedure, a new mean value was calculated and recorded, together with the number of accepted values and the resulting standard deviation.

a) Pressure and Temperature

Pressure transducers and thermocouples were positioned at different locations of the test facility. These positions are indicated in Fig. 2.4 by P and T respectively. The subscripts G and L denote measurement of air and liquid respectively. The subscript K denotes measurement of a parameter in the channel.

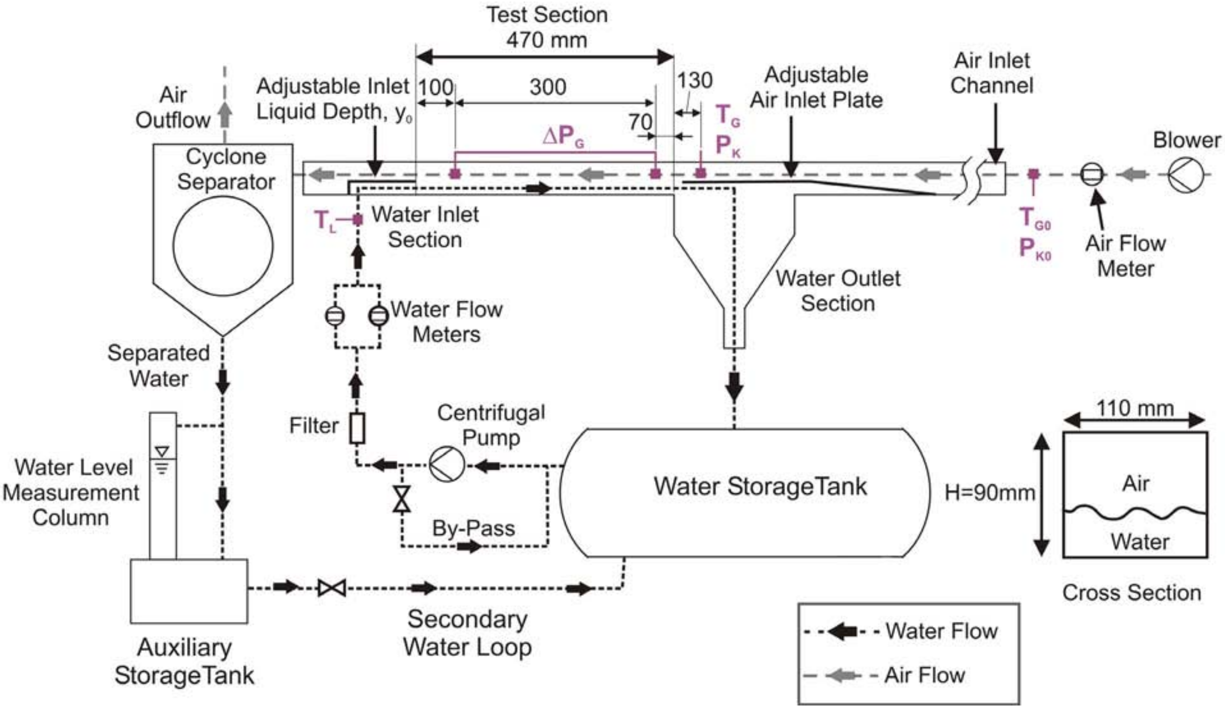

Fig. 2.4. Schematic diagram of the WENKA test facility with designation of measurement systems positions. All dimensions given in millimetres.

The following positions were acquired:

T_L: Water temperature at the liquid inlet section. Measured with a Ni-Cr-Ni thermocouple.

T_{G0}: Air temperature measured immediately downstream the air flow meter with a Ni-Cr-Ni thermocouple.

P_{K0}: Channel pressure measured immediately downstream the air flow meter by means of a piezo-resistive pressure transducer.

T_G: Air temperature at the entrance leading to the test section. Measured with a Ni-Cr-Ni thermocouple.

P_K: Channel pressure measured at the entrance of the test section with a membrane pressure transducer.

ΔP_G: Pressure difference in the test section. Measured with a membrane differential pressure transducer.

b) Liquid Volumetric Flow Rate

Liquid volume flow rate was measured alternatively by means of two electromagnetic flow meters, optimized for high to medium and for low flow rate ranges respectively (see

Fig. 2.4). A minimum conductivity of 20 µS/cm is required for measuring demineralized water. This was achieved by adding a small quantity of saline solution in the water storage tank.

Faraday's law of induction states that a voltage is induced in a conductor moving in a magnetic field. In an electromagnetic flow meter, the flowing medium corresponds to the moving conductor. A constant magnetic field is generated by a switched direct current of alternating polarity. Water flows through the device and induces a voltage that is proportional to the flow velocity. This induced voltage is detected by two measuring electrodes and transmitted to the amplifier. The volumetric flow rate is computed on the basis of the pipe's diameter with a measurement uncertainty less than 0.2%. The liquid mass flow rate is calculated with the measured liquid temperature and the corresponding density at 1 bar.

c) Air Volumetric Flow Rate

The air volumetric flow rate delivered by the blower was measured with a vortex flow meter. Vortex flow meters operate according to Karman's vortex street principle. Vortices are created and alternate behind a bluff body. The number of vortices shed per time unit, the vortex frequency, is directly proportional to the air flow rate. The measurement uncertainty is less than 1%. The corresponding air mass flow rate was calculated using the air density at the pressure and temperature measured immediately after the flow meter (T_{G0} and P_{K0}, position given in Fig. 2.4).

Air volumetric flow rate at the test section inlet was determined using the air mass flow rate delivered by the blower and the air density at the pressure and temperature measured at the air inlet position, T_G and P_K.

2.2.2 Measurement of Inlet Water Depth, y_0

As will be shown later, one of the most significant parameters concerning flow regimes in horizontal countercurrent flow is the inlet liquid depth, y_0, that is to say, the liquid depth at channel position $x = 0$ mm. The inlet water depth was set by adjusting the height of the parallel plate at the water inlet section. This was done manually using screws placed at the bottom of the liquid inlet section (see chapter 2.1 Experimental Set Up) and measuring the displacement of the plate with a folding rule. With this simple method a resolution of 0.5 mm can be assured.

2.2.3 Measurement of Outlet Water Depth, y_A

The water depth at the end of the test section, y_A, (channel position, $x = 470$ mm), was needed in several experiments and was measured also with a folding rule.

2.2.4 Determination of Flow Regime Maps

a) Flow Patterns and Limits of Flow Regimes

Table 7 presents the initial flow conditions for which flow regime maps were performed in the WENKA test facility. Five series of experiments were carried out for initial water depths y_0 ranging between 3 and 15 mm. In each series, a constant inlet water depth y_0 was set. Given an inlet water depth, different liquid volumetric flow rates, $\dot{V}_L$, (or mass flow rates, $\dot{m}_L$) were investigated. Once y_0 and $\dot{m}_L$ are set, the liquid velocity at the inlet, u_{L0}, and the Froude number at the inlet, Fr_0, are set as well. It can be concluded that, if y_0 is kept constant, the inlet liquid velocity and the inlet Froude number can only be changed by changing the mass flow rate.

To identify the different flow regimes in WENKA, the following steps were performed:

First of all, y_0 was set. Then, the lowest possible volumetric flow rate of liquid was set by controlling the rotational speed (r.p.m.) of the centrifugal pump. The lowest possible liquid volumetric flow rate was that able to fill the gap between the parallel plate and the channel bottom. In this way, the inlet water depth y_0 could be guaranteed. This value corresponds to the lowest value of $\dot{m}_L$ and $\dot{V}_L$ given for each y_0 in Table 7.

Once y_0 and $\dot{m}_L$ were set, the flow regime of liquid with stagnant air was studied. Normally, a subcritical liquid film was observed. The flow regime type was noted and then the blower was switched on at its minimum rotational speed. This was approximately a value around 20 l/s. Again, the flow regime was studied and classified. The air flow rate was increased gradually in several steps while the liquid flow rate and the inlet water depth were kept constant. After each increase of air flow rate, the changes in flow regime were noted. Depending on the air and water velocities, different flow patterns could be identified: stratified horizontal flow (with subcritical, critical and supercritical liquid layer), partially reversed flow and totally reversed flow.

For low air and liquid flow rates, stratified wavy flow was observed. The liquid film was subcritical and numerous 3-dimensional wavelets were generated at the interface as a result of having countercurrent flow of air. These wavelets were stationary for very low air velocity. At higher air velocities the small amplitude waves propagated upstream. If the air velocity was further increased, the air flow caused a disturbed wavy interface, with 2-dimensional, large amplitude waves propagating upstream. From this point on, the air velocity could not be increased anymore until a velocity was reached, at which wave amplitudes were large enough to flow over the liquid inlet plate. As soon as this happened, the flow conditions were written down. This was the onset of partially reversed flow for the given y_0 and $\dot{m}_L$. Changing $\dot{m}_L$ and repeating the experiment, the different points of the partially reversed flow line for y_0 were obtained.

For medium-high liquid mass flow rates, a hydraulic jump was observed in the liquid film even without countercurrent air flow. The jump occurred always at the end of the test section (x = 470 mm) and progressed in the air flow direction stabilizing at a certain position of the channel. The higher the air velocity, the closer was the hydraulic jump position to the water inlet, since the air flow pushed the jump towards the water inlet with a larger drag force. If the air flow rate was increased sufficiently, the hydraulic jump was moved by the air flow beyond the liquid inlet plate and partially reversed flow set in.

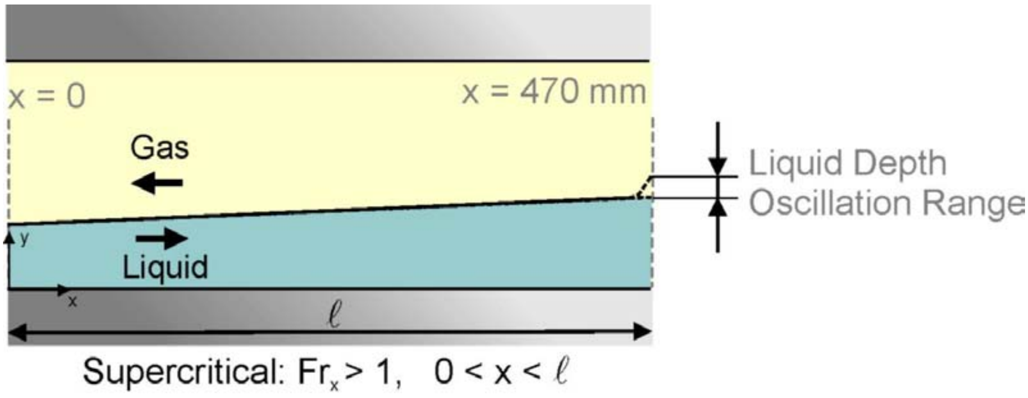

Fig. 2.5. Unstable oscillating interface in supercritical flow.

For high liquid mass flow rates the liquid film was supercritical and the interface between air and water was rather smooth, even at high air velocities. Only the so-called supercritical waves were observed. These surface waves are caused by capillarity and therefore their amplitudes and wavelengths are small compared to the liquid depth, although they increase if either the gas or the liquid velocity is increased. As the air mass flow rate was increased, the interface between air and water began to be unstable and to oscillate rapidly between a high and a low liquid depth value at the end of the test section (see Fig. 2.5). Liquid depth oscillation ranges of several millimeters were observed, especially at high air velocities and right before a transition to subcritical flow in form of a hydraulic jump occurred.

With an initial supercritical flow, the onset of partially reversed flow occurred at relatively high air velocities in the form of a hydraulic jump that was generated suddenly at the end of the test section and propagated very quickly in the air flow direction setting reversed flow.

Once partially reversed flow was achieved, the air flow rate was increased further keeping all other parameters constant until totally reversed flow was observed.

The experimental procedure was repeated using a new value of y_0 that was kept constant for a new set of liquid mass flow rates and different gas flow rates.

Since flow regime maps in terms of the superficial velocities of each phase are very popular in two-phase flow, these flow parameters will be also employed in this study to represent the flow regimes observed experimentally.

The flow conditions investigated in WENKA were specifically chosen to cover extensively the flow conditions typical of a LOCA scenario with ECC hot leg injection. These are basically supercritical flows with countercurrent flow of gas. Since the small Froude number range, and specially the hydraulic jump range with countercurrent flow of gas, was not yet investigated, the experimental matrix was extended to subcritical flows. Table 8 presents a comparison of the flow conditions investigated in WENKA and those typical of the reactor case. Discussion about similarity between the reactor case and the flow regimes investigated in WENKA follows in chapter 5.3.

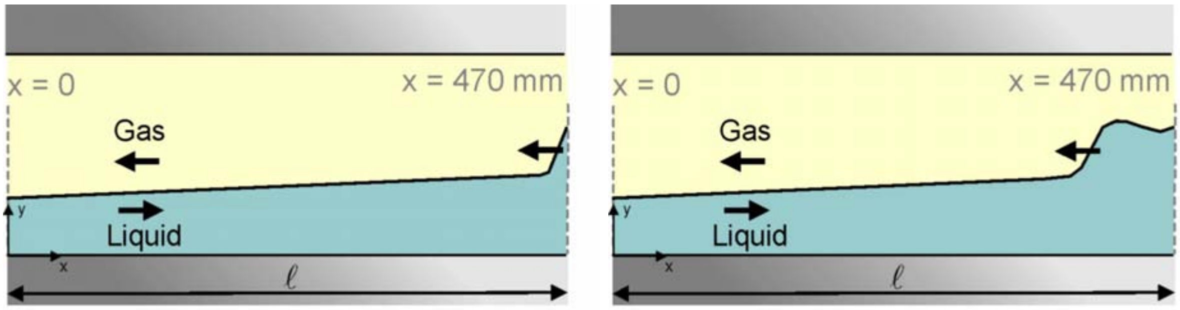

Transition from SP to SB flow: a Hydraulic Jump generates at the end of the test section

Hydraulic Jump Propagation: the hydraulic jump moves in the air flow direction

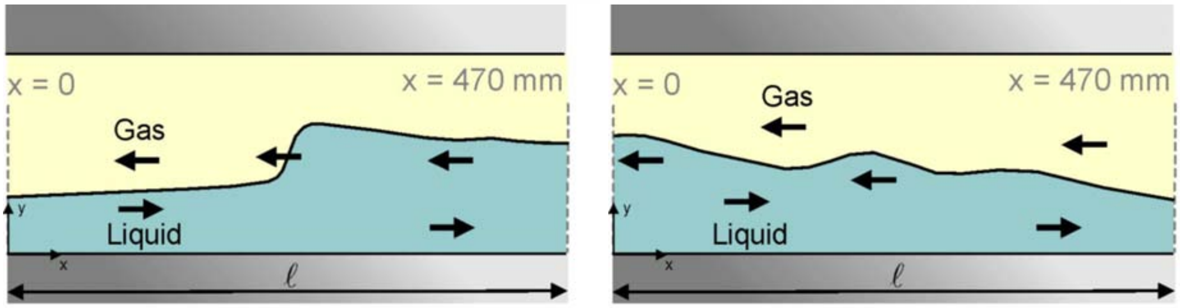

Hydraulic Jump Propagation: the hydraulic jump moves in the air flow direction

Onset of Partially Reversed Flow: The wave front of the hydraulic jump reaches the liquid injection point

Fig. 2.6. Onset of Partially Reversed Flow mechanism in supercritical flows: Hydraulic jump propagation.

b) Occurrence of a Hydraulic Jump

For initial supercritical liquid flow, a hydraulic jump was always observed in the test section before reversed flow occurred. It can be concluded that a transition to subcritical flow is a necessary condition for the onset of flow reversal in supercritical flow. For this reason, some experiments were focused to study the occurrence of a hydraulic jump with countercurrent flow of air. In addition, the influence of the inlet water depth on the flow conditions for which hydraulic jump occurs was investigated.

The onset of a hydraulic jump in the channel was investigated experimentally for inlet water depths of 3, 7, 9, 11 and 15 mm and for gas velocities of up to 9 m/s. Water was injected with a large Froude number (supercritical flow), and with a constant inlet water depth y_0, counter a constant air flow rate. The water depth at the end of the test section, y_A, was measured with a folding rule. With this water depth and the corresponding liquid velocity, u_{LA}, the Froude number Fr_A was calculated. This Froude number was larger than unity as long as the flow remained supercritical. The liquid volumetric flow rate was slightly reduced and y_A was measured again to obtain new values for u_{LA} and Fr_A. This procedure was performed until the transition to subcritical flow was observed, always as the value $\mathrm{Fr}_A = 1$ was reached. This liquid volumetric flow rate was written down as the liquid volumetric flow rate at the onset of a hydraulic jump. The complete procedure was repeated with a new constant value of air flow rate.

First measurements corroborated that the liquid volumetric flow rates for which a hydraulic jump occurs in the test section are very sensitive to the channel inclination angle. A deviation from the horizontal of 0.2° leads to very different results. This phenomenon was also observed by Chun and Yu [16] (see page 20). Therefore, the test section inclination angle was set with a high precision water level to 0° ± (30 µm / 500 mm).

Experimental observations corroborated that the transition from supercritical to subcritical flow occurs with the onset of a hydraulic jump at the end of the test section. Based on this fact, a theoretical approach for the onset of a hydraulic jump was derived (See chapter 3, *Theoretical Model*). Finally, experimental data were obtained and compared with the theory (Presented in Chapter 4).

c) Occurrence of Reversed Flow

In view of the fact, that a stable hydraulic jump can be observed in the channel without causing a flow reversal, it can be assessed that subcritical flow is a necessary but not sufficient condition for the onset of reversed flow. Therefore, an additional criterion for the onset of partially reversed flow was investigated. This criterion is presented in chapter 4.1.

The experimental procedure employed is similar to that described in the previous chapter. Water was injected with a constant volumetric flow rate and a given inlet water depth. An air flow rate was set in the test section. The water depth at the end of the test section was measured and the air flow rate was increased in small steps, each time with measurement of the water depth y_A, until onset of reversed flow was observed. The flow conditions for which this happened were written down.

2.2.5 Determination of Back Flow Ratios

The flow rates of liquid carried over by the gas during partially reversed flow were studied for numerous experiments. For these experiments, the valve situated between the auxiliary water tank and the main storage tank was closed and partially reversed flow was set in the channel. Water flowing in the air direction was separated by the cyclone and filled the auxiliary storage tank. The progressive change in water level in the auxiliary water tank could be measured for a given period of time using a transparent column with a capacitive level probe.

Experiments were performed for inlet water depths ranging from 7 to 11 mm. The liquid level measurement was repeated for each experiment six times and then an average of the liquid volumetric flow rate was calculated. Some experiments were also performed under totally reversed flow. In this case, the liquid volumetric flow rate must coincide with the injected volumetric flow rate. Comparison of the measured liquid carry-over with the injected liquid volumetric flow rate showed that the uncertainty of the measurement was less than 5%.

2.2.6 Measurement of Local Velocities

Local flow velocities were performed in the test section for selected experiments using PIV. This technique permits to obtain an entire velocity field within a selected region of the flow that is illuminated by a laser sheet. The flow is seeded with tracer particles, which are illuminated by the laser sheet in the plane of the flow direction. The light scattered by the particles is recorded in two different frames by a CCD camera within a short time interval. Each frame is divided in cells, generally of 32x32 pixels. It is supposed, that all particles inside a cell move in the same direction with the same velocity and that their velocity is the same velocity as that of the flow, without slip. By means of statistical methods like the cross-correlation, the most probable distance traveled by the particles situated inside a cell as well as the mean travel direction are estimated. The corresponding displacement vector is obtained. Since the time between the two frames dt is known, the velocity vector associated to each cell can be calculated dividing the displacement vector by this known time. This procedure is performed for each cell by special software and as a result, a whole velocity field of the flow can be obtained.

A 640x480 pixel CCD camera was used together with an Nd:Yag pulsed laser with a wavelength of 532 nm. The pulse duration was 5 ns. The cell size was chosen between 32x32 and 16x16 pixel. This cell size yielded the best statistical solutions obtained by means of cross-correlation and a good spatial resolution.

To investigate entrance effects in the test section, velocities of single-phase air flow were first obtained. Secondly, velocity profiles for liquid film, with and without countercurrent flow of air, were measured.

a) Air Velocity Measurement

An experimental series was performed without water in the channel to investigate air entrance effects in the test section. Single-phase air flow velocities were measured at different positions in the test section with PIV to obtain velocity profiles of the complete cross section. Deviations from the typical fully developed form of a velocity profile were subsequently analyzed. To perform these measurements without water, the liquid inlet plate was placed at its minimum position, i.e. 2 mm, and the air entrance plate was set at a height of 6 mm, corresponding to the lowest possible plate height.

The injection of the particles has to be done without significantly disturbing the flow, but in a way and at a location that ensures homogeneous distribution of the tracers. A number of techniques are used to generate and supply particles for seeding gas flows. In case of measurements in air flows, a well established technique is the use of Laskin nozzle generators to produce oil particles.

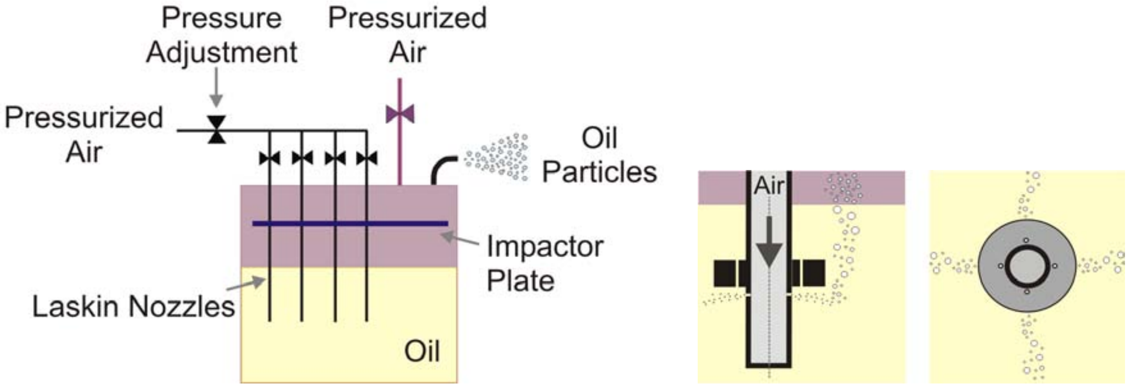

Fig. 2.7. Laskin Nozzle Generator.

The aerosol generator consists of a closed cylindrical container filled with oil, with two air supply pipes and one aerosol outlet (see Fig. 2.7). The air inlet flow rate can be regulated by valves. Four Laskin nozzles, 1mm diameter, are equally spaced in one of the inlet pipes. A horizontal circular impactor plate is placed inside the container, so that a small gap of about 2 mm is formed by the plate and the inner wall of the container. Compressed air with 0.5 to 1.5 bar pressure difference with respect to the outlet pressure is applied to the Laskin nozzles and creates air bubbles in the liquid. Due to the shear stress induced by tiny sonic jets, small oil drops are generated and carried inside the bubbles towards the oil surface. Big particles are retained by the impactor plate; small particles (less than 10 µm) escape through the gap and reach the aerosol outlet. The number of particles can be controlled by the four valves at the nozzle inlets.

The seeding particles were introduced at the entrance of the air inlet channel by means of a nozzle positioned at the center of the channel cross section to provide a homogeneous mixing all the way through the air inlet channel. An impactor plate was placed at the channel entrance in order to homogenize better the mixture. Homogeneous seeding is a prerequisite to get good PIV results.

The air flow was illuminated by a laser sheet from the top. The position of the area of interest measured is shown in Fig. 2.8. Velocities within a region of 68x90 mm were measured. The region of interest begins at a distance of 110 mm of the water inlet plate edge.

In order to get good results with PIV, it is essential to avoid reflections of the laser light on surfaces which are within the recorded region. Otherwise, the CCD-chip can be overexposed and this could lead to destruction of several pixels. For this reason, the bottom of the channel was painted using fluorescent dye. This special paint is excited by a light with a wavelength of 532 nm and emits fluorescent light with a different wavelength. A special camera filter, that blocks the reflected fluorescent light and passes the light scattered by the tracer particles (532 nm), was mounted in the CCD camera. Additionally, anti-reflecting spray was applied at the top of the channel. Only a small gap was let free to introduce the laser sheet into the test section. Finally, the back wall of the test section, where the area of interest was chosen, was painted in black mat, since homogenous background leads to better PIV results.

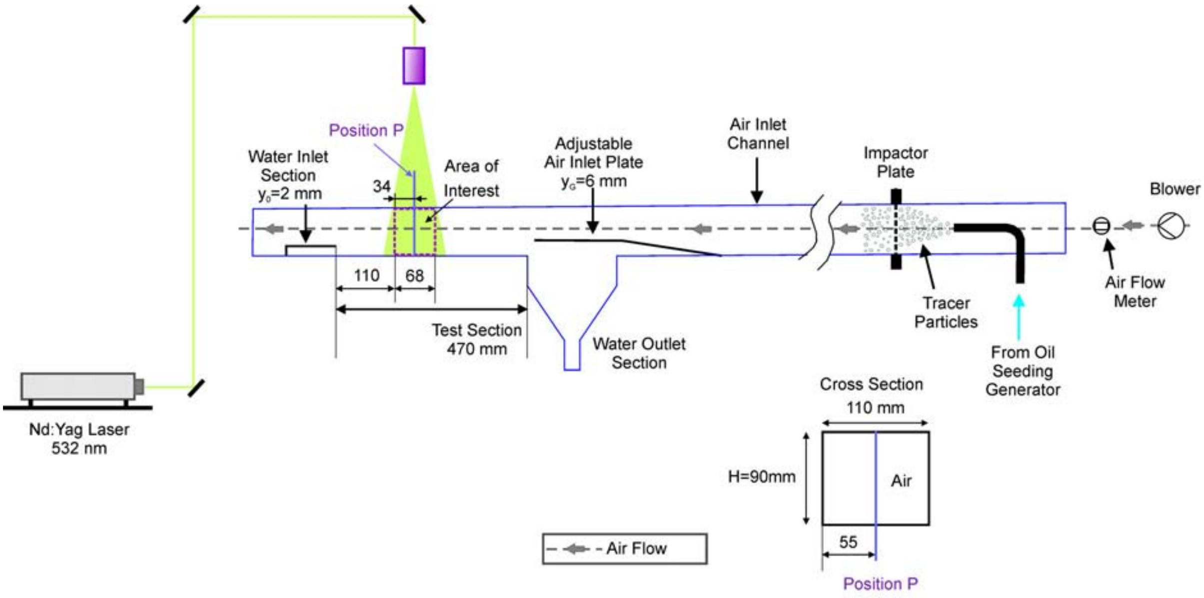

Fig. 2.8. Set up of PIV measurements for single-phase air flow.

Air velocity profiles were obtained always at a distance of 144 mm from the liquid inlet plate edge, in the center of the area of interest (*Position P* in Fig. 2.8). Measurements were carried out for mean gas velocities ranging between 5.6 and 18 m/s. Tracer particles were injected at 0.5 bars into the air inlet channel. To investigate the influence of the aerosol velocity as a secondary flow on the air velocity profile, measurement of tracer particles injected at 0.5 bar was also performed.

b) Liquid Film Velocity Measurement

To investigate the effect on liquid velocities caused by the countercurrent flow of air, PIV measurements of liquid film flow with and without air flow were carried out using water inlet depths ranging between 8 and 16 mm. Liquid film velocity profiles were obtained at three different positions, namely at a distance of 136, 144 and 152 mm from the liquid inlet plate edge. These positions are represented in Fig. 2.9 as Position P1, P2 and P3 respectively.

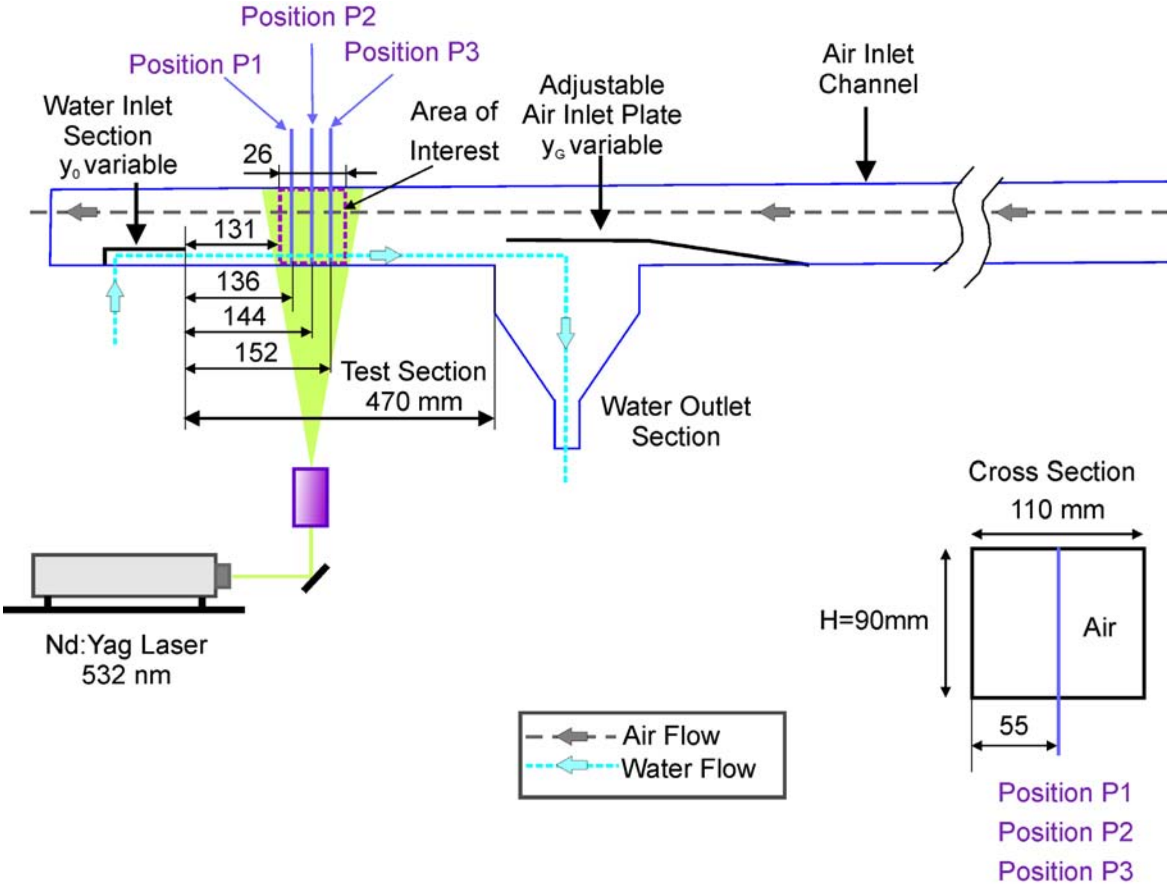

Fig. 2.9. PIV set up for liquid measurements.

Liquid velocity profiles were obtained by illuminating the flow from the bottom with the laser sheet. First tests had shown, that light coming from the air side was strongly reflected at the interface and this fact yielded two serious technical problems: first, only a small fraction of the incident laser light could penetrate the liquid film and several dark regions were observed in the PIV recordings, since light intensity was not strong enough to see the seeding. Second, the incident laser light was reflected by the liquid film with high intensity. Thus, the liquid film was illuminated from the channel bottom to avoid reflection of the laser light at the liquid surface, which could lead to overexposure of the CCD-chip. As seeding, glass tracer particles with a diameter of less than 50 µm were employed. These particles have a good particle-to-fluid density ratio for water and are, therefore, frequently used for PIV measurements in water. In the first experimental series, liquid film velocities were measured for inlet velocities between 0.1 and 0.8 m/s, first with stagnant air, and afterwards, with countercurrent flow of air at air velocities ranging between 6 and 8 m/s.

2.2.7 Liquid Film Morphology

The characteristics of the liquid film under countercurrent flow conditions were investigated for a certain set of experiments. Particularly, the liquid depth and wave properties of the wavy film were analyzed.

The form of the interface was studied for three different transitions: the transition from supercritical flow to hydraulic jump flow, the onset of partially reversed flow and the onset of totally reversed flow. The experiments were recorded with a high-speed camera at 500 frames/s and with a digital photographic camera with a resolution of 3 Million pixels. The high-speed pictures were developed and digitized with a resolution of 768 x 574 pixels (24 bit). The image processing software Optimas ® was employed to perform macros that filtered the digital images and recognized automatically the interface as a curve with approximately 410 points separated 1 mm each. The Cartesian coordinates (x, y) of these points were obtained by means of an accurate scaling system.

3 Theoretical Program: Prediction of the Onset of a Hydraulic Jump from an Initial Supercritical Film Flow

3.1 Momentum Equations for the Supercritical Liquid Film

Consider a one-dimensional two-phase flow of liquid with a countercurrent flow of gas in steady state. The liquid flows in form of a film in a horizontal channel of length ℓ. The channel has a rectangular cross section of height H and width Z (shown in Fig. 3.1).

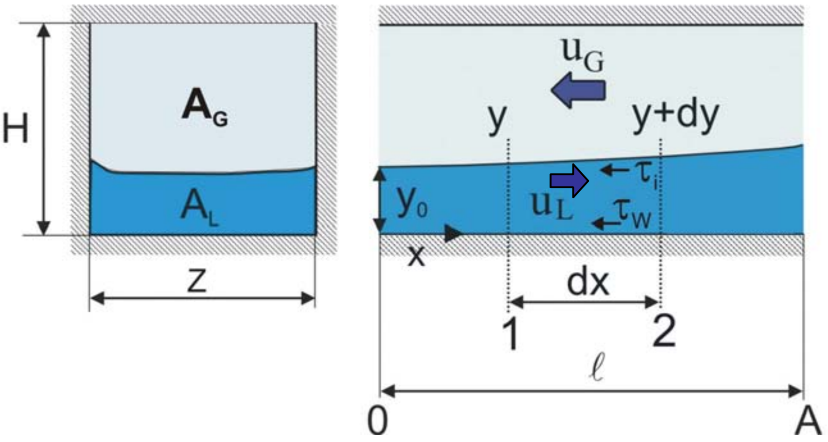

Fig. 3.1. Supercritical liquid film flow with countercurrent gas flow.

Water enters at the left side with a liquid depth y_0 and is dumped at $x = \ell$ on the right side. The subscripts w and i are used to represent values at the wall and at the interface respectively.

Initially, the liquid film is assumed to flow supercritically, that is to say, the local Froude number of the liquid film, is greater than unity for the entire channel length and the interface between gas and liquid is rather smooth. Variations in gas pressure shall be small compared with the hydrostatic pressure in the liquid. This simplification is only valid if the liquid flow is supercritical, when the momentum forces are dominant. A wavy, subcritical flow, however, would have to include static pressure variations in the gas phase.

If the hydrostatic pressure in the liquid, the wall and interfacial friction terms and the inertial term of the liquid are taken into account, the one-dimensional momentum equation for the liquid film between position 1 (liquid film depth y) and position 2 (liquid film depth y +dy) can be obtained as follows:

$$\left(\rho_L u_{L1}^2 + p_1\right) yZ - \tau_w dxZ - \tau_i dxZ - \left(\rho_L u_{L2}^2 + p_2\right)(y + dy)\, Z = 0 \qquad (3.1)$$

Where u_{Lj} is the liquid velocity at the position j, ρ_L the liquid density and p the hydrostatic pressure.

The average hydrostatic pressures in the liquid at position 1, p_1, and at position 2, p_2, are given as

$$p_1 = \frac{1}{2}\rho_L g y; \quad p_2 = \frac{1}{2}\rho_L g(y + dy) \tag{3.2}$$

The wall shear stress, τ_w, is proportional to the liquid density, to the wall fanning friction factor, λ_w, and to the squared liquid velocity. On the other hand, the interfacial shear stress depends on the interfacial fanning friction factor λ_i, the gas density and the squared sum of the gas and the liquid velocity.

$$\tau_w = \lambda_w \frac{\rho_L}{2} u_L{}^2; \qquad \tau_i = \lambda_i \frac{\rho_G}{2}(u_G + u_L)^2 \tag{3.3}$$

Introducing these terms in the momentum equation yields

$$\left(\rho_L u_{L1}^2 + p_1\right) yZ - \lambda_w \frac{\rho_L}{2} u_L{}^2 dxZ - \lambda_i \frac{\rho_G}{2}(u_G + u_L)^2 dxZ - \left(\rho_L u_{L2}^2 + p_2\right)(y + dy)Z = 0 \tag{3.4}$$

If the average liquid flow velocity is expressed by the liquid mass flow rate $\dot{m}$ as

$$u_L = \frac{\dot{m}_L}{\rho_L y Z} \tag{3.5}$$

The momentum equation can now be rewritten as

$$\begin{aligned}&\left(\frac{\dot{m}_L{}^2}{\rho_L y^2 Z^2} + \frac{1}{2}\rho_L g y\right) y - \lambda_w \frac{\rho_L}{2} \frac{\dot{m}_L{}^2}{\rho_L{}^2 y^2 Z^2} dx - \lambda_i \frac{\rho_G}{2}\left(\frac{u_G}{u_L} + 1\right)^2 \frac{\dot{m}_L{}^2}{\rho_L y^2 Z^2} dx - \\ &-\left(\frac{\dot{m}_L{}^2}{\rho_L (y + dy)^2 Z^2} + \frac{1}{2}\rho_L g(y + dy)\right)(y + dy) = 0\end{aligned} \tag{3.6}$$

The new momentum equation depends on the ratio of the gas to the liquid velocity, so it is convenient to define a slip velocity ratio, s.

$$s = \frac{u_G}{u_L} \tag{3.7}$$

Neglecting second order terms of dy yields the following differential equation for the liquid depth y:

$$\frac{\dot{m}_L{}^2}{\rho_L^2 g Z^2} dy - y^3 dy - \frac{\lambda_w}{2} \frac{\dot{m}_L{}^2}{\rho_L{}^2 g Z^2} dx - \frac{\lambda_i}{2} \frac{\rho_G}{\rho_L}(s + 1)^2 \frac{\dot{m}_L{}^2}{\rho_L^2 g Z^2} dx = 0 \tag{3.8}$$

3.2 Dimensionless Momentum Equations

The typical length scale is the liquid depth at which Fr = 1, defined as critical depth, y_C:

$$\mathrm{Fr} = \frac{u_L}{\sqrt{gy}} = \frac{\dot{m}_L}{\rho_L y Z \sqrt{gy}}; \qquad {y_C}^3 = \frac{{\dot{m}_L}^2}{{\rho_L}^2 Z^2 g} \tag{3.9}$$

Rewriting equation (3.8) in terms of the critical depth, we obtain

$$\left({y_C}^3 - y^3\right) dy - \frac{1}{2}\lambda_w {y_C}^3 dx - \frac{1}{2}\lambda_i \frac{\rho_G}{\rho_L}(s+1)^2 {y_C}^3 dx = 0 \tag{3.10}$$

Now, equation (3.10) can be transformed into a dimensionless equation using the following parameters:

$$\eta = \frac{y}{y_C}; \;\; \xi = \frac{x}{y_C} \qquad \eta_0 = \frac{y_0}{y_C}; \;\; \xi_0 = 0 \qquad \eta_A = \frac{y_A}{y_C}; \;\; \xi_A = \frac{\ell}{y_C} \tag{3.11}$$

Position 0 stands for the x-position at the liquid entry, which is the begin of the channel (x = 0) and the subscript A denotes parameter at the end of the channel ($x = \ell$). Using this dimensionless parameters, a supercritical flow has a dimensionless depth $\eta < \eta_C \equiv 1$.

In this way, the dimensionless momentum equation can be presented as

$$\int_{\eta_0}^{\eta_A} \left(1 - \eta^3\right) d\eta = \int_0^{\xi_A} \frac{\lambda_w}{2} d\xi + \int_0^{\xi_A} \frac{\lambda_i}{2} \frac{\rho_G}{\rho_L} (s+1)^2 d\xi \tag{3.12}$$

This equation can be solved once the corresponding fanning friction factors, λ_W and λ_i, are chosen.

3.3 Fanning Friction Factors

3.3.1 Wall Friction Factor

The wall friction factor was derived from the Blasius correlation ([12], [57]) for hydraulically smooth surface and turbulent flow:

$$\lambda_B = \frac{0.3164}{\mathrm{Re}_L^{0.25}} \qquad \text{if } 2320 < \mathrm{Re}_L < 10^5 \tag{3.13}$$

λ_B is the friction factor used to estimate pressure loses of a liquid film with a depth y, in a channel with a width Z and a length dx (see Fig. 3.2):

$$\Delta p = \lambda_B \frac{dx}{d_H} \frac{\rho}{2} u^2 \tag{3.14}$$

Where ρ is the density of the fluid, u the fluid velocity and d_H the hydraulic diameter calculated as

$$d_H = 4\frac{A}{S_L} = \frac{4Zy}{2y+Z} = \frac{4y}{2\frac{y}{Z}+1} \tag{3.15}$$

A is the cross sectional fluid area and S_L is the wetted perimeter of this area. If the liquid film depth y is much smaller than the channel width Z, we can simplify

$$Z >> y \Rightarrow d_H \approx 4y \tag{3.16}$$

The fanning friction factor λ_W is necessary to calculate the wall shear stress on the liquid film:

$$\tau_W = \lambda_W \frac{\rho_L}{2} {u_L}^2 \tag{3.17}$$

Establishing in a fluid element a force balance between pressure and shear, λ_W can be estimated as a function of λ_B. Consider a fluid element with a liquid depth y in a rectangular channel of width Z and the forces of hydraulic pressure F_P and friction F_τ acting on it (see Fig. 3.2).

The hydraulic force acting on the fluid element will be

$$F_P = \Delta P Z y = Z y \lambda_B \frac{dx}{4y} \frac{\rho}{2} u^2 = \frac{\lambda_B}{8} dx \rho u^2 Z \tag{3.18}$$

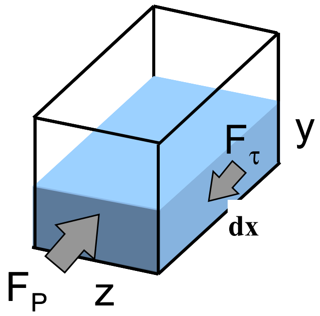

Fig. 3.2. Forces acting in a fluid element in a rectangular channel.

On the other hand, the frictional force due to shear, F_τ, can be expressed in terms of the fanning friction factor λ_W:

$$F_\tau = \tau_W (dx\,Z + 2dx\,y) = \lambda_W \frac{\rho}{2} dx\,u^2 Z \tag{3.19}$$

If the pressure losses in the fluid element are just due to friction, equations (3.18) and (3.19) can be equaled, giving the relationship between λ_W and λ_B :

$$\lambda_W = \frac{\lambda_B}{4} \tag{3.20}$$

For this reason, if the Blasius equation is applied to estimate the fanning friction factor present in the shear stress equation (equation (3.17)), the Blasius friction factor must be divided by 4. We obtain

$$\lambda_w = \frac{0.3164 \mathrm{Re}_L^{-0,25}}{4} \qquad \text{if } 2320 < \mathrm{Re}_L < 10^5 \tag{3.21}$$

Here, the liquid Reynolds number is defined as

$$\mathrm{Re}_L = \frac{u_L y}{\nu_L} = \frac{\dot{m}_L}{\rho_L Z \nu_L} \tag{3.22}$$

Where ν_L is the kinematic viscosity of the liquid. Note that the liquid Reynolds number remains constant along the channel: changes in Reynolds number could only be caused by a change in mass flow rate. However, assuming steady state conditions keeps $\dot{m}$ constant, and so the Reynolds number is constant as well.

3.3.2 Interfacial Friction Factor

The interfacial friction factor λ_i is needed to estimate the interfacial shear stress:

$$\tau_i = \lambda_i \frac{\rho_G}{2}(u_G + u_L)^2 \tag{3.23}$$

The interfacial friction factor was estimated by using existing correlations. Three different assumptions were checked out.

First, the interfacial friction factor was neglected as for the case of liquid flow with stagnant air flow ($\lambda_i \cong 0$).

The second model assumed that the interfacial friction factor is similar to that between a gas and a smooth wall as supposed by Fabre et al. [25], where the interfacial friction factor is calculated from a modified Blasius correlation. This type of correlation was applied by Stevanovic and Studovic for the case of smooth liquid film [61].

$$\lambda_F = \frac{C_f}{\mathrm{Re}_G^n} \qquad \begin{array}{lll} \text{Turbulent Flow}: & C_f = 0.0046, & n = 0.2 \\ \text{Laminar Flow}: & C_f = 16, & n = 1 \end{array} \tag{3.24}$$

The values $C_f = 0.0046$ and $n = 0.2$ for turbulent flow were employed.

In chapter 4 will be shown, that these two first models (stagnant air like and Blasius like interfacial friction) do not predict with sufficiently high accuracy the occurrence of a hydraulic jump at high gas velocities. Therefore, a third intend was to choose an interfacial friction factor correlation, for which the friction factor increases with the Reynolds number of the liquid film (unlike in the Blasius correlation). Among the correlations present in the literature, the Kim et al. correlation [37] was chosen:

$$\lambda_K = 0.14 \cdot 10^{-5}\,\mathrm{Re}_L + 0.021 \tag{3.25}$$

This correlation was developed for steam-water countercurrent stratified flow in a duct. Since λ_K is the friction factor obtained from pressure losses data [10], the corresponding fanning friction factor to calculate the interfacial shear stress λ_i is

$$\lambda_i = \frac{\lambda_K}{4} = \frac{0.14 \cdot 10^{-5}\,\mathrm{Re}_L + 0.021}{4} \tag{3.26}$$

Ohnuki et al. [51] used also the Kim et al. correlation in their study on scale effects on countercurrent flow during hot leg injection. However, there is a lack of appropriate correlations for such conditions in the literature, and further investigations should be done in this field.

Taking the wall friction factor given by equation (3.21) and the interfacial friction factor given by equation (3.26), equation (3.12) can be solved. The liquid Reynolds number as well as the slip velocity ratio were considered constant for the complete channel length, since in a supercritical flow, the liquid depth changes slightly, so that the changes in velocity and in hydraulic diameter can be neglected. We obtain

$$(\eta_A - \eta_0) - \frac{1}{4}\left(\eta_A{}^4 - \eta_0{}^4\right) = \frac{0.3164}{8}\mathrm{Re}_L^{-1/4}\xi_A + \frac{(0.14 \cdot 10^{-5}\,\mathrm{Re}_L + 0.021)}{8}\frac{\rho_G}{\rho_L}(s+1)^2\xi_A \tag{3.27}$$

The solution of the momentum equation for the liquid film gives, as a result, the liquid depth at the end of the channel, y_A, in its dimensionless form, η_A as a function of the dimensionless inlet liquid depth, η_0, the Reynolds number of the liquid, the fluids density ratio, the slip velocity ratio and the dimensionless channel length, $\xi_A = \ell / y_C$.

3.4 Occurrence of a Hydraulic Jump

Equation (3.27) includes both, subcritical and supercritical solutions. If $\eta_0 < 1$ at the flow inlet, the liquid depth increases from $\eta = \eta_0$ to $\eta = 1$. If $\eta_0 > 1$ at the inlet, the liquid depth decreases from $\eta = \eta_0$ to $\eta = 1$. However, there is no solution for x beyond the point where $\eta = 1$. Instead, in this case, a hydraulic jump occurs in the flow and the liquid depth jumps from $\eta < \eta_C$, i. e. a supercritical flow, to $\eta > \eta_C$, i. e. a subcritical flow, somewhere in the channel. As a conclusion, a supercritical flow throughout the whole channel can only occur if $\eta_0 < 1$ and $\eta_A < 1$ at $\xi = \ell / y_c \equiv \xi_A$.

Starting with a supercritical flow, with $\eta_0 < 1$, the hydraulic jump will occur as soon as $\eta_A = 1$ at $\xi = \xi_A$. Substituting these jump conditions into equation (3.27) yields the constraint equation for the occurrence of a hydraulic jump if $\eta_0 < 1$. We get

$$(1-\eta_0)-\frac{1}{4}(1-\eta_0^4)=\frac{0.3164}{8}\mathrm{Re}_L^{-1/4}\xi_A+\frac{(0.14\cdot 10^{-5}\mathrm{Re}_L+0.021)}{8}\frac{\rho_G}{\rho_L}(s+1)^2\xi_A \tag{3.28}$$

It is here convenient to relate η_0 to the Froude number Fr_0 at the liquid flow inlet:

$$\eta_0=\frac{y_0}{y_C}=\left(\frac{\dot{m}_L}{Z\rho_L\sqrt{gy_0^3}}\right)^{-2/3}=\mathrm{Fr}_0^{-2/3} \tag{3.29}$$

Since

$$\frac{\xi_A}{\eta_0}=\frac{\ell}{y_0} \tag{3.30}$$

the dimensionless momentum equation for the occurrence of a hydraulic jump in a channel with countercurrent flow of gas, starting from a supercritical flow is given by

$$\frac{\ell}{y_0}=\frac{8\left(\frac{3}{4}\mathrm{Fr}_0{}^{2/3}+\frac{1}{4}\mathrm{Fr}_0^{-2}-1\right)}{0.3164\mathrm{Re}_L{}^{-1/4}+\frac{\rho_G}{\rho_L}(s+1)^2(0.14\cdot 10^{-5}\mathrm{Re}_L+0.021)} \tag{3.31}$$

This dimensionless equation depends only on the liquid conditions at the entrance (y_0, Fr_0) the ratio of densities, the slip velocity ratio between gas and liquid at the liquid outlet and the liquid Reynolds number as well as on the channel length ℓ.

3.5 Considerations

Equation (3.31) predicts the occurrence of a hydraulic jump in a horizontal channel by estimating the channel length ℓ necessary to have a transition from supercritical to subcritical flow at the end of the test section. To investigate the occurrence of a hydraulic jump in a channel of given length ℓ_{CH} and with a given inlet liquid depth $y_{0,CH}$, the flow conditions can be introduced in equation (3.31) and the value ℓ / y_0 obtained can be compared with the real ratio ℓ_{CH} / $y_{0,CH}$. The following procedure is recommended to predict the occurrence of a hydraulic jump in a channel:

1) Calculate liquid inlet flow conditions: Fr_0, Re_L with the liquid velocity at the inlet u_{L0} and the inlet liquid depth $y_{0,CH}$ (see Fig. 2.2).

2) Calculate the slip velocity ratio using the liquid and gas velocities at the end of the test section:

$$s = \frac{u_{GA}}{u_{LA}} \tag{3.32}$$

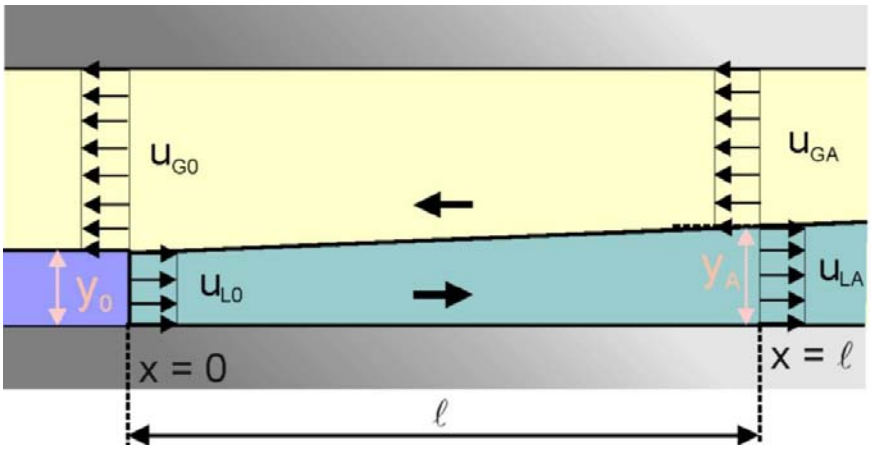

Fig. 3.3. Velocities to be considered in equation (3.31).

To calculate u_{GA} and u_{LA} it is necessary to estimate y_A by means of equation (3.27).

$$(\eta_A - \eta_0) - \frac{1}{4}\left(\eta_A{}^4 - \eta_0{}^4\right) = \frac{0.3164}{8}\mathrm{Re}_L^{-1/4}\xi_A + \frac{(0.14 \cdot 10^{-5}\,\mathrm{Re}_L + 0.021)}{8}\frac{\rho_G}{\rho_L}(s+1)^2\xi_A \tag{3.33}$$

and

$$\eta_A = \frac{y_A}{y_c} \tag{3.34}$$

Where the critical height y_C can be calculated with equation (3.9).

$$y_C{}^3 = \frac{\dot{m}_L{}^2}{\rho_L{}^2 Z^2 g} \tag{3.35}$$

=(3.9)

Once y_A is obtained, the gas and liquid velocity at the end of the test section can be calculated:

$$u_{GA} = \frac{\dot{m}_G}{\rho_G (H - y_A) Z} \tag{3.36}$$

$$u_{LA} = \frac{\dot{m}_L}{\rho_L y_A Z} \tag{3.37}$$

3) Calculate ℓ by means of equation (3.31).

4) Compare ℓ with ℓ_{CH}. If $\ell > \ell_{CH}$, the flow is supercritical for the whole channel. On the other hand, if $\ell = \ell_{CH}$, a hydraulic jump will occur at the end of the test section. Finally, there is a hydraulic jump in the channel if $\ell < \ell_{CH}$.

4 Results

4.1 Integral Measurements

4.1.1 Flow Regime Maps and Limits of Flow Regimes

Fig. 4.1 shows flow regime maps obtained with different inlet water depths ranging from 3 to 15 mm in terms of the liquid and gas superficial velocities (u_{LS} and u_{GS} respectively).

Three different regions can be clearly distinguished in the flow maps: a region of stable countercurrent horizontal flow, a region where the liquid flows partially reversed and a region with no liquid delivery, i.e. a totally reversed flow. For stable countercurrent stratified flow, we differ between *subcritical flow*, *supercritical flow* and *flow with a hydraulic jump*, indicated with the acronyms SB, SP and HJ respectively.

The region of stable countercurrent stratified flow is delimited by the curve ***O**nset of **P**artially **R**eversed **F**low*, OPRF. The ***O**nset of **T**otally **R**eversed **F**low* is indicated by the curve OTRF. Beyond the totally reversed flow line, in the *no liquid delivery region*, no liquid reaches the outlet of the test section due to the effect of the countercurrent gas flow.

In the next chapters, all possible flow regimes and associated transitions will be described.

a) Stable Horizontal Countercurrent Flow of Liquid and Gas

The flow regime maps presented in Fig. 4.1 show that stratified horizontal countercurrent flow is only possible for a given range of liquid and gas superficial velocities, namely, for low to moderate superficial gas velocities. Stratified countercurrent horizontal flow exists in three different modes:

- subcritical liquid film with countercurrent gas flow (SB),
- supercritical liquid film with countercurrent gas flow (SP),
- liquid film with a hydraulic jump and countercurrent gas flow (HJ).

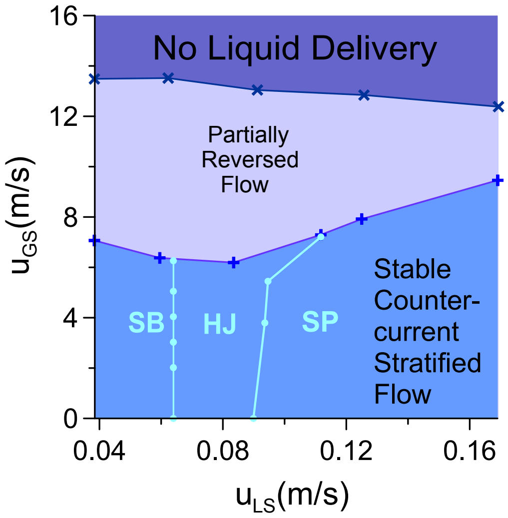

Inlet Water Depth y_0 = 15 mm

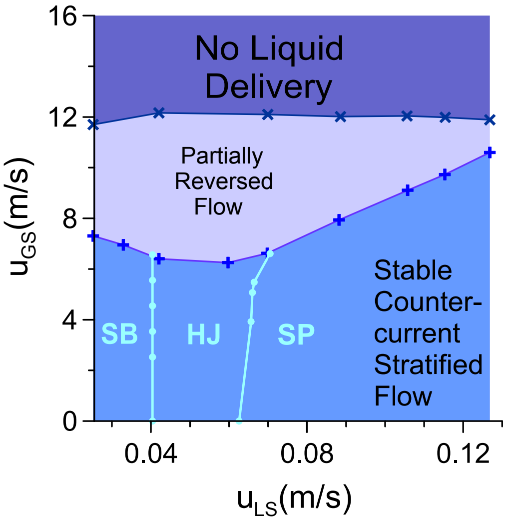

Inlet Water Depth y_0 = 11 mm

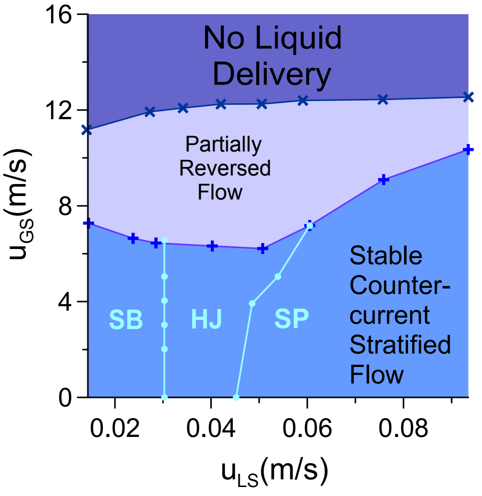

Inlet Water Depth y_0 = 9 mm

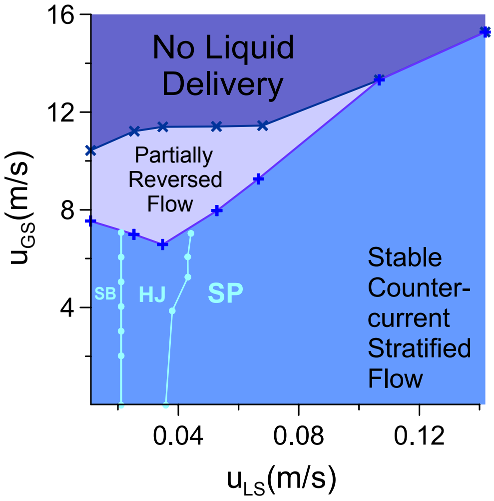

Inlet Water Depth y_0 = 7 mm

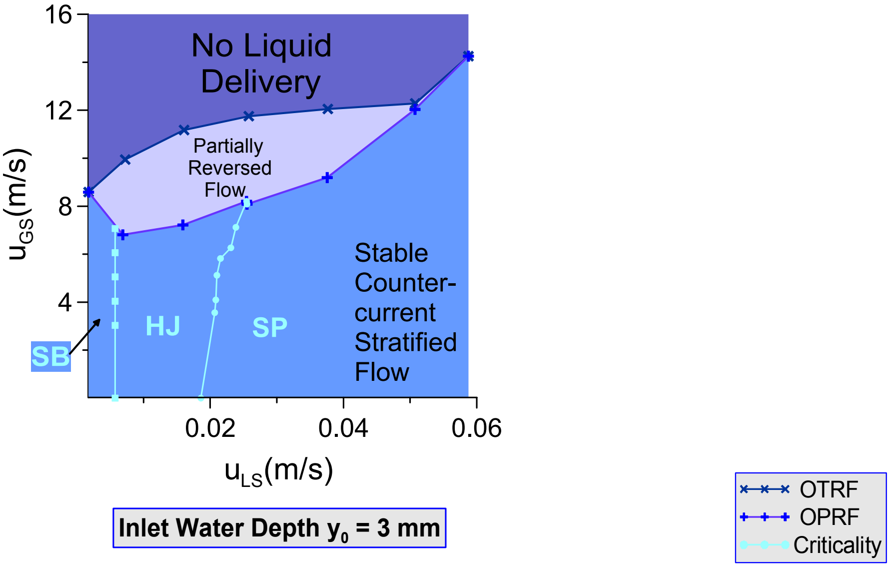

Inlet Water Depth y_0 = 3 mm

Fig. 4.1. Flow regime maps in terms of superficial velocities.

Subcritical Flow

Subcritical flow with stagnant air is a very tranquil flow since liquid velocities are very low. The liquid depth decreases progressively along the test section. For comparison, in Fig. 4.2 images of a subcritical flow at low inlet Froude number Fr_0 are presented for the case of stagnant air and two different gas volumetric flow rates. The interface is rather smooth in the two first cases but becomes wavy in the third case.

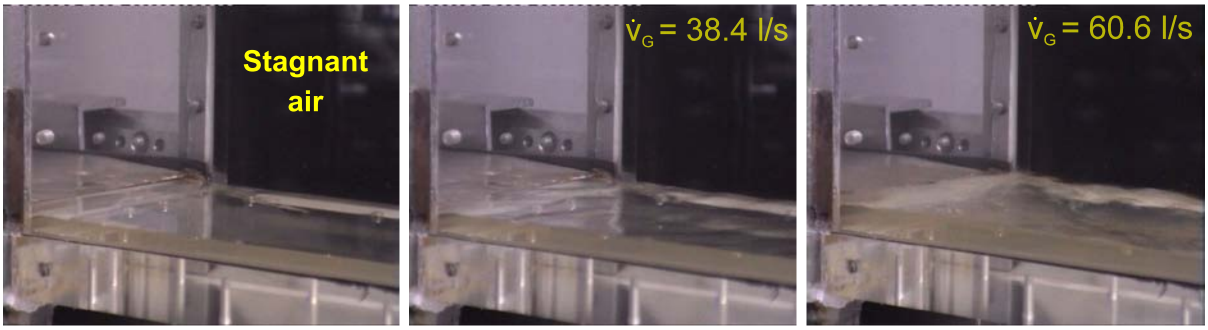

Fig. 4.2. Subcritical flow with stagnant air, an air volumetric flow rate of 38.4 l/s and one of 60.6 l/s respectively. The inlet liquid depth is 7 mm and the inlet Froude number is $\mathrm{Fr}_0 = 0.33$.

In general, the effect of countercurrent flow on a subcritical liquid film can be classified into three different cases:

- Low air velocities ($u_{GS} < 25$ m/s) yield the formation of 3-dimensional waves of small amplitudes and small wavelengths, the so-called *ripples*. These ripples propagate in the liquid flow direction.

- At medium air velocities (25 m/s < $u_{GS} < 35$ m/s), the propagation velocity of the interfacial waves reduces considerably. Even stationary waves can be observed for a given set of liquid and gas velocities: equilibrium between the propagating surface waves and the drag force applied on them by the gas exists. However, the existence of stationary waves is usually limited to a narrow range of flow conditions.

- If $u_{GS} > 35$ m/s, the interfacial waves propagate in the air flow direction. For these flow conditions, the waves are mainly 2-dimensional and have large wavelengths.

Supercritical Flow

The oblique interference pattern typical of supercritical flows can be observed for the complete range of air velocities investigated (including air velocity equal to zero, i.e. stagnant air) independently of the liquid film inlet velocity. By increasing the air velocity, the supercritical waves increase their amplitudes progressively as they propagate downstream in the liquid flow direction. Additionally, the propagation velocity of the waves increases for higher air velocities. The interface of the liquid film oscillates at the liquid outlet with high frequency and the liquid depth at the outlet varies between a minimum and a maximum value. The minimum value corresponds to the value measured with stagnant air. The maximum value can be predicted with equation (3.27) if the experimental flow conditions are introduced to calculate η_A. Some values are presented in Table 9 for comparison (see Appendix, Page 122).

A first obvious conclusion that can be extracted from the data presented in Table 9 is that the liquid depth at the end of the test section is smaller than the critical depth for a supercritical flow. It increases progressively as either the liquid flow rate is reduced or the gas flow rate is increased.

Equation (3.27) predicts with good accuracy the increase in liquid depth. Fig. 4.3 presents values of the liquid depth at the end of the test section (test section length ℓ = 470 mm) obtained in 28 experiments with supercritical flow and countercurrent flow of air. Data employed are those given in Table 9 (Page 122). Inlet liquid depths ranging from 3 to 15 mm were investigated. The liquid inlet Froude number was varied from 1.5 up to 8.8. The gas velocities ranged from 0 (stagnant air) to 14 m/s.

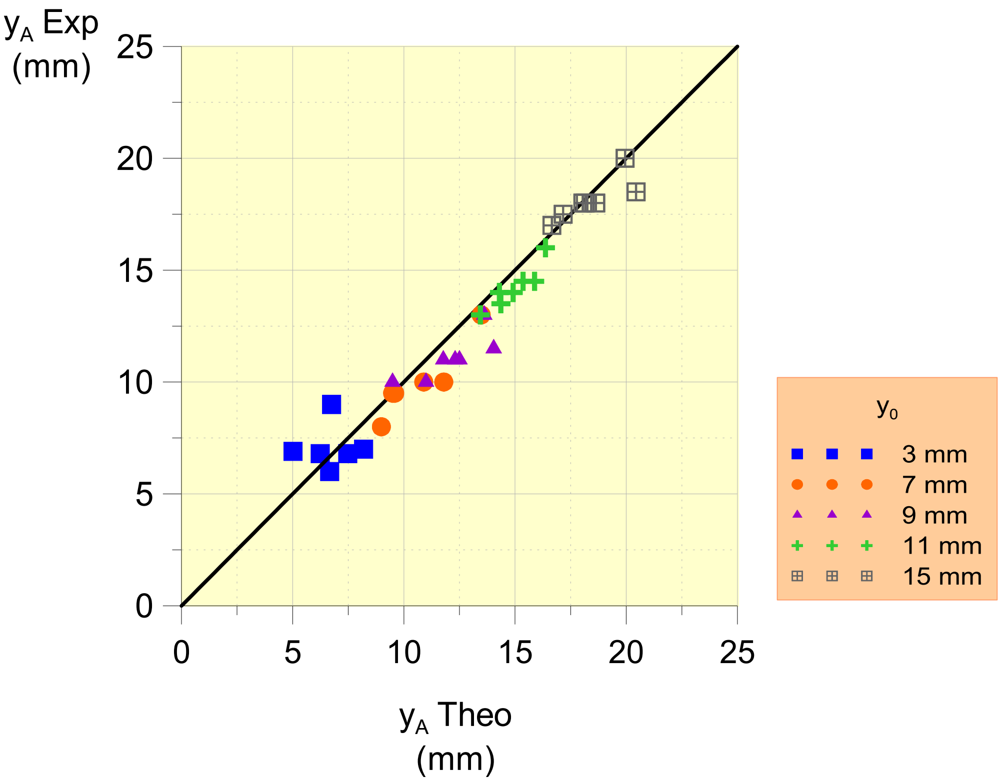

Fig. 4.3. Liquid depth prediction by means of equation (3.27) for supercritical flows with countercurrent air flow (test section length ℓ = 470 mm).

It can be concluded that the value of the liquid depth at the end of the test section does not have to be measured experimentally, since equation (3.27) can be used to predict y_A reliably, provided the liquid film flows supercritically and the flow conditions are known.

Hydraulic Jump

A hydraulic jump occurs if the Froude number is equal to unity at any position of the test section, i.e. the critical depth is reached at that position. The oblique interference pattern, typical of supercritical waves, can be observed at the supercritical side of the hydraulic jump, whereas the large amplitude, large wavelength waves typical of subcritical flows are present at the subcritical side of the jump (See Fig. 4.4). Therefore, if a hydraulic jump is present in the test section, the supercritical part of the liquid film has a relatively smooth interface while the subcritical region presents a rough wavy interface.

Fig. 4.5 presents the region for which a hydraulic jump exists in the test section with an inlet water depth of 9 mm.

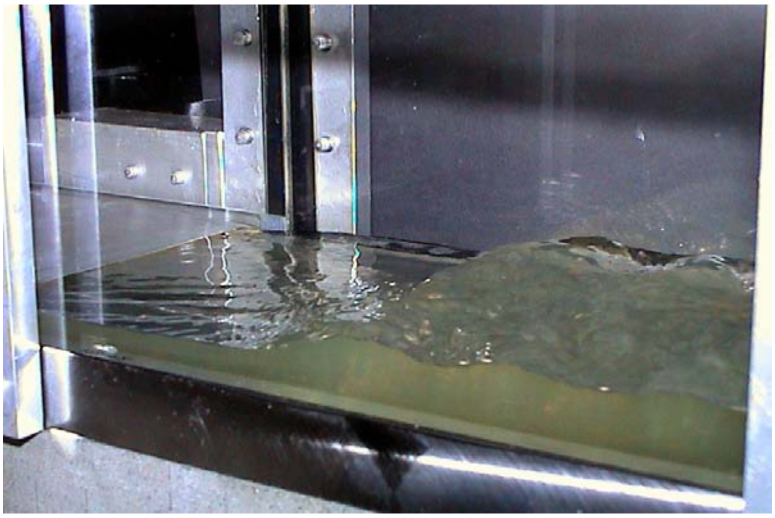

Fig. 4.4. Hydraulic jump in the test section.

The hydraulic jump region is delimited by three curves: the transition between supercritical flow and hydraulic jump flow (curve C-E), the transition between subcritical flow and hydraulic jump flow (curve D-F) and the transition from hydraulic jump flow to reversed flow (E-F).

At the right side of the flow regime with a hydraulic jump, the region with supercritical film flow can be observed (SP). In order to illustrate the transition from supercritical flow to hydraulic jump flow, consider a supercritical flow with the flow conditions defined by point 1 in Fig. 4.5. Air is flowing countercurrently. Now, the superficial velocity of the gas is increased gradually (by increasing the air volumetric flow rate) while the liquid superficial velocity is kept constant. The flow regime changes following the line defined by the points 1 to 3.

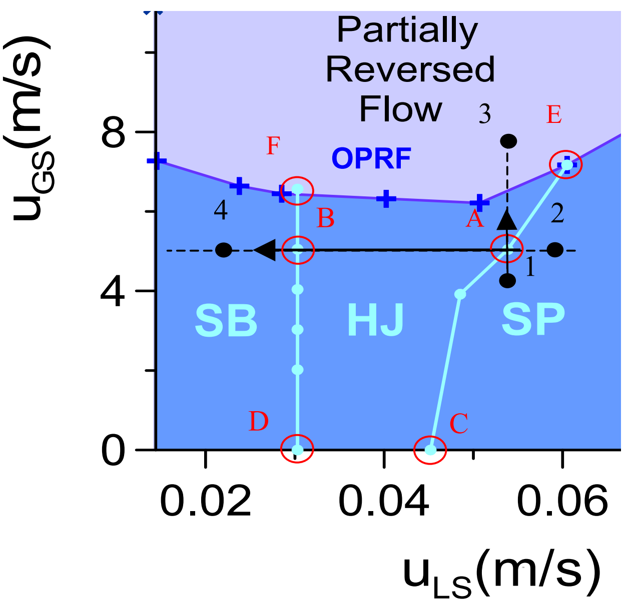

Fig. 4.5. Flow regimes with a hydraulic jump (inlet water depth 9 mm).

First, the liquid depth at the end of the test section becomes unstable. This effect becomes more important as the superficial gas velocity is increased. As the point A in Fig. 4.5 is reached, the liquid depth obtains its largest value at the end of the test section, though only for a fraction of second. The first transition is observed: the critical depth is reached at the end of the test section for a very small fraction of time and the supercritical flow changes to subcritical flow, so that a hydraulic jump generates at the end of the test section. Fig. 4.6 shows a sequence of images taken during this transition for an inlet water depth y_0 of 9 mm and a constant liquid superficial velocity of 0.055 m/s. These flow conditions correspond to those existing at point A in Fig. 4.5. The occurrence of a hydraulic jump was observed for a superficial gas velocity of approximately 5 m/s.

For superficial gas velocities lower than this critical one, the liquid depth is smaller than the critical depth in the complete channel. As the gas velocity is increased, the liquid depth increases also. The Froude number of the liquid film at the end of the test section is still higher than unity, but reduces progressively with increasing gas velocity. At the threshold velocity of 5 m/s, the liquid depth is equal to the critical one at the end of the test section and the liquid depth grows suddenly. The hydraulic jump occurs and progresses in the air flow direction until an equilibrium position is reached. A small change of the flow conditions in the test section yields a change in the hydraulic jump position, so that there is a wide range of liquid and gas velocities where a hydraulic jump flow is possible. The narrowest range of liquid flow rates, for which a hydraulic jump flow is present in the test section, corresponds to a liquid film with gas velocity equal to zero, i.e. with stagnant air (see region C-D in Fig. 4.5).

u_{GS}= 4.2 m/s

The liquid film flows supercritically.

u_{GS}= 5 m/s

The critical depth is reached at the liquid outlet: a hydraulic jump is generated.

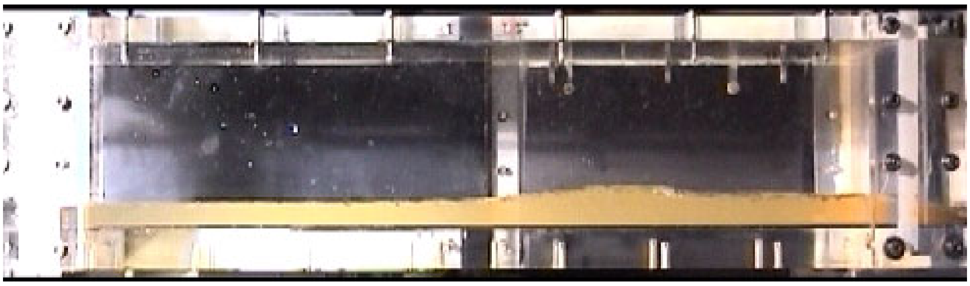

u_{GS}= 5 m/s

The hydraulic jump progresses in the air flow direction to a stable position.

u_{GS}= 5 m/s

The stable position in the test section is reached. If the flow conditions are kept constant, the hydraulic jump remains in this position.

Fig. 4.6. Hydraulic jump formation with an initial supercritical flow (y_0 = 9 mm, u_{LS} = 0.055 m/s)

Once the point A is reached and the hydraulic jump is generated, the gas superficial velocity can be further increased keeping the liquid flow rate constant. The hydraulic jump moves towards the liquid inlet, pushed by the increasing gas flow. If the gas flow rate is sufficiently increased, a transition to reversed flow can occur and, at first, partially reversed flow sets in (point 3, Fig. 4.5).

On the other hand, a transition to subcritical liquid film flow can occur if the flow conditions are changed following the line from point 2 to point 4 (Fig. 4.5). In this case, we begin once more with a supercritical flow but change the flow conditions keeping the superficial velocity of the gas constant, at approximately 5 m/s. The liquid flow rate is then reduced in small steps. Again, the first transition is from supercritical flow to hydraulic jump flow at position A (Fig. 4.5). The hydraulic jump is generated also at the end of the test section, in a similar way as shown in Fig. 4.6, but in this case, due to a reduction of the liquid flow rate. If the superficial liquid velocity is further reduced, the hydraulic jump moves upstream and, for a given liquid superficial velocity, reaches the liquid inlet position ($x = 0$). The Froude number at the inlet is now equal to unity ($Fr_0 = 1$). The transition to subcritical flow is imminent (point B, Fig. 4.5). The hydraulic jump disappears rapidly if the superficial liquid velocity is slightly reduced and subcritical flow sets in the entire test section. For lower liquid superficial velocities than that present in point B, the flow is subcritical, as for example in point 4. Some flow conditions during this transition are presented in Table 10 (See Appendix, page 123).

Recapitulating, the transition of an initial supercritical flow to a subcritical flow can occur if either the liquid flow rate is reduced (line 2 - 4 in Fig. 4.5) or the gas flow rate is increased (line 1 - 3 in Fig. 4.5). When performing these transitions in WENKA, no hysteresis was observed, i.e. the transition from point 1 to point 4 occurs at the same superficial velocities as the transition from point 4 to point 1.

b) Transition from Supercritical to Subcritical Flow: Hydraulic Jump at the End of the Test Section

The onset of a hydraulic jump in the channel, from a supercritical flow, was investigated experimentally in more detail for inlet water depths ranging from 3 to 15 mm and for gas velocities up to 8 m/s. The flow was initially supercritical and the liquid flow rate was reduced progressively at a constant gas flow rate. The flow conditions present in some of the experiments, for which a hydraulic jump occurred at the end of the test section, are given in Table 12. The nomenclature adopted is shown in Fig. 3.3 (see page 54). The liquid depth at the outlet, y_A, was measured right before the hydraulic jump was generated, that is to say, the experimental value of y_A at the onset of a hydraulic jump is given. On the other hand, the critical depth corresponding to a Froude number equal to unity at the end of the test section, $y_{A,C}$ was estimated with equation (3.9) using the experimental value of the liquid mass flow rate.

The data presented in Table 12 show a hydraulic jump occurring at the end of the test section if $y_A = y_{A,C}$, that is to say, $Fr_A = 1$. If the experimental values given in Table 12 for the liquid depth at the end of the test section, when a hydraulic jump occurs (column y_A), are compared with those obtained analytically for the critical depth (column $y_{A,C}$), it can be observed that effectively, the hydraulic jump occurs as the critical depth at the end of the test section is reached. This transition can be predicted using the analytical model presented in chapter 1 (equation (3.31), page 53):

$$\frac{\ell}{y_0} = \frac{8\left(\frac{3}{4}\mathrm{Fr_0}^{2/3} + \frac{1}{4}\mathrm{Fr_0^{-2}} - 1\right)}{0.3164\mathrm{Re_L}^{-1/4} + \frac{\rho_G}{\rho_L}(s+1)^2(0.14\cdot 10^{-5}\mathrm{Re_L} + 0.021)}$$

Comparison of the results obtained with (3.31) to predict the onset of a hydraulic jump and experimental values obtained in the test facility can be performed to verifiy the interfacial friction model that was used when deriving equation (3.31). For this purpose, the general form of the constrain equation for the onset of a hydraulic jump (equation 3.12)

$$\int_{\eta_0}^{\eta_A} \left(1-\eta^3\right) d\eta = \int_0^{\xi_A} \frac{\lambda_w}{2} d\xi + \int_0^{\xi_A} \frac{\lambda_i}{2} \frac{\rho_G}{\rho_L} (s+1)^2 d\xi$$

was solved using each of three possible correlations for interfacial friction factor:

1) $\lambda_i = 0$ (stagnant air approximation)

2) $\lambda_i = \frac{C_f}{4 \cdot Re_G^n}$ $\quad$ Turbulent Flow: $C_f = 0.0046, \quad n = 0.2$ (Blasius)

3) $\lambda_i = \frac{0.14 \cdot 10^{-5} Re_L + 0.021}{4}$ (Kim et al.)

The wall friction factor was always estimated with equation (3.21). The three different interfacial friction factors lead to three different solutions of the momentum equation to predict the onset of a hydraulic jump starting from an initial supercritical flow. Each of these three solutions was employed to predict the experimental data presented in Fig. 4.7. Comparison of the results obtained using these three different models for the interfacial friction and those obtained experimentally is presented in Fig. 4.7. The values ℓ / y_0 for which a hydraulic jump is expected in the channel are compared with experimental ones.

Among the data acquired, only selected experiments for inlet water depths of 4, 8 and 12 mm are presented, in order not to overload Fig. 4.7 (See Table 13).

Comparison with experimental data shows that both, the stagnant air model and the Blasius model, fail by predicting the onset of a hydraulic jump for gas velocities higher than 7 m/s. These data points can be seen in Fig. 4.7 as those deviating significantly from theory (region indicated with dotted line).

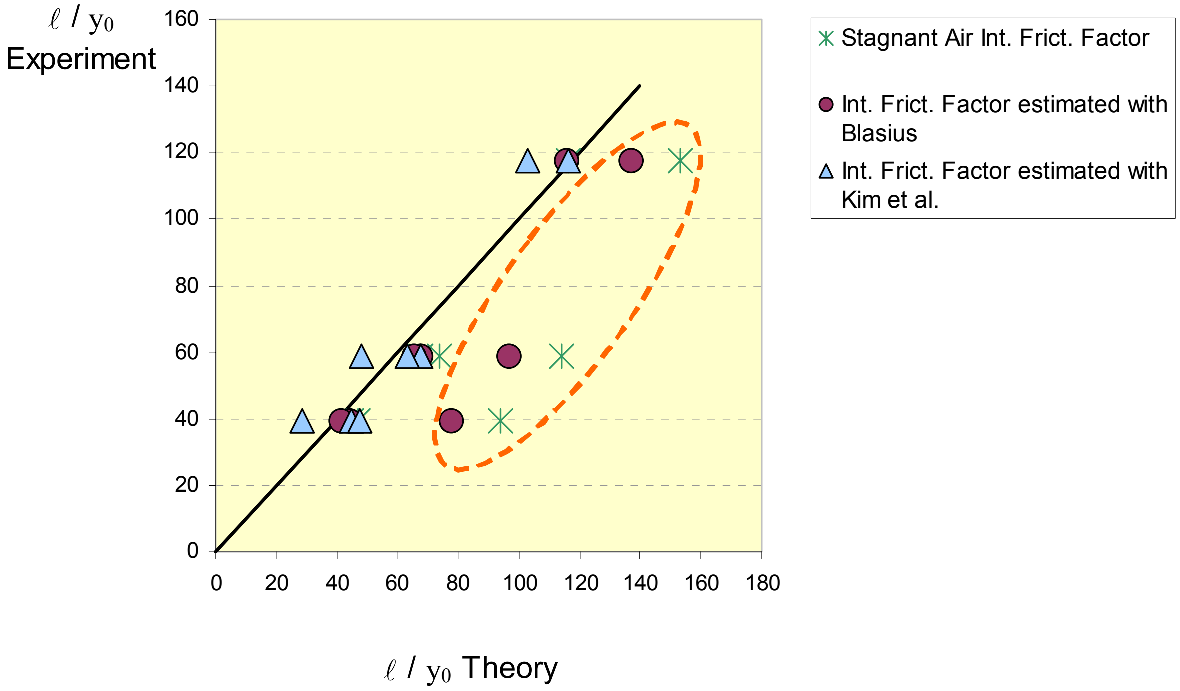

Fig. 4.7. Comparison of Interfacial Friction Factor Models by predicting the occurrence of a hydraulic jump in the WENKA test facility.

On one hand it can be concluded that a simple model with stagnant air cannot predict well the onset of hydraulic jump, if air is flowing countercurrently. Thus, the influence of the air flow must be taken into account in the case of closed channels. On the other hand, the assumption that the interfacial friction factor decreases with the gas Reynolds number, like in the Blasius correlation, leads to discrepancies. Using an interfacial friction factor based on the liquid Reynolds number, as the correlation of Kim et al. does, yields the best agreement (data points represented by triangles in Fig. 4.7). Therefore, the correlation obtained by Kim et al. was chosen for equation (3.31).

As a conclusion, the constrain equation (3.31) for predicting the occurrence of a hydraulic jump in the test section forecasted successfully a large number of experiments performed in WENKA, with liquid inlet depths ranging from 3 to 15 mm, Froude numbers at the injection point up to 4 and gas velocities up to 8 m/s. As shown in Fig. 4.8, predictions and experimental data (Data from Table 13, page 126) differ by less than 20%.

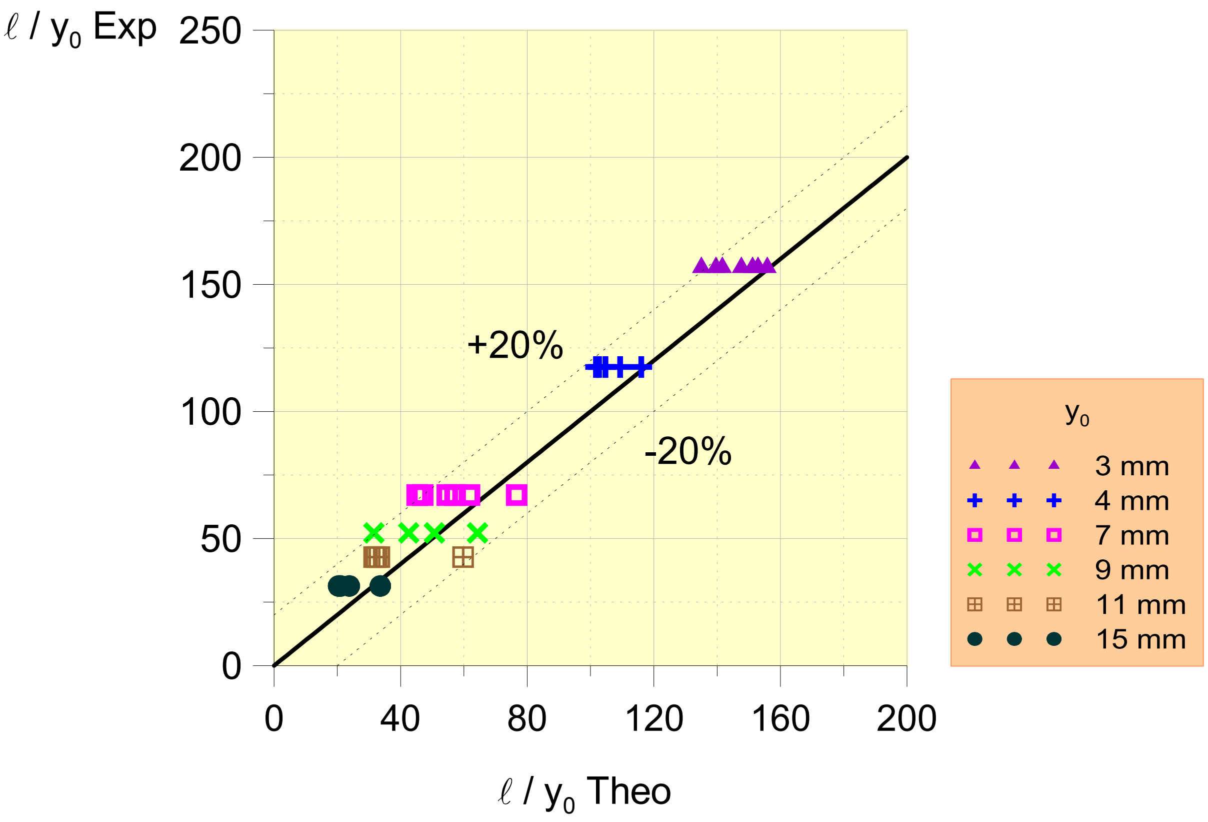

Fig. 4.8. Hydraulic jump occurrence predicted by equation (3.31).

c) Transition from Subcritical to Supercritical Flow: Hydraulic Jump at the Beginning of the Test Section

It was shown, that the transition from supercritical flow to subcritical flow can be predicted analytically with an equation that estimates the occurrence of a hydraulic jump at the end of the test section, provided the liquid film is supercritical initially. Now, we consider the reverse process, i.e. a transition from point 4 to point 2 in Fig. 4.5. At point 4 the liquid flow is subcritical and the flow conditions change towards point 2 as the superficial liquid velocity is increased.

The subcritical flow changes to supercritical flow if the superficial liquid velocity is increased sufficiently so that the critical liquid depth is reached at some position in the test section. In a subcritical flow the liquid depth decreases gradually in the flow direction. It has a value lower than the critical depth. This means that, if the liquid flow rate is increased, the position where at first the critical depth will be reached is the injection point, since this will be always the position with the maximum depth. Indeed, experiments showed that a hydraulic jump grows at the liquid inlet as soon as the liquid inlet depth is equal to the critical depth, that is to say, $y_C = y_0$.

In supercritical flow, the interface at the liquid outlet oscillates and the amplitude of this oscillation depends basically on the gas velocity. This, however, does not occur at the inlet of the test section. At the injection point, the inlet depth is always equal to y_0 since this depth is forced by the parallel plate used to perform the liquid injection. As the depth at the inlet does not vary depending on the gas velocity, the transition curve between subcritical and hydraulic jump flow is a vertical line (see Fig. 4.1). The position of this vertical line corresponds to the critical superficial velocity of the liquid $u_{LS,crit}$ at the inlet that leads to a Froude number equal to unity:

$$Fr_0 = \frac{u_{L0}}{\sqrt{g \cdot y_0}} = \frac{u_{LS}}{\sqrt{g \cdot y_0}} \frac{A_{TOT}}{A_L} = \frac{u_{LS}}{\sqrt{g \cdot y_0}} \frac{H \cdot Z}{y_0 \cdot Z} = \frac{u_{LS}}{\sqrt{g \cdot y_0}} \frac{H}{y_0} = 1 \quad \Rightarrow \quad u_{LS,crit} = \frac{\sqrt{g \cdot y_0^{\,3}}}{H} \tag{4.1}$$

Here A_{TOT} is the total cross sectional area of the test section (90x110 mm²), A_L is the area of the liquid, H the channel height (90 mm) and Z the channel width (110 mm).

In Fig. 4.9 this transition is presented for an inlet liquid depth of 7 mm and a constant gas flow rate of 51 l/s. The liquid is initially subcritical at a liquid flow rate of 3 l/s. The liquid flow rate is increased progressively up to 18 l/min.

Again, no hysteresis was observed for this transition.

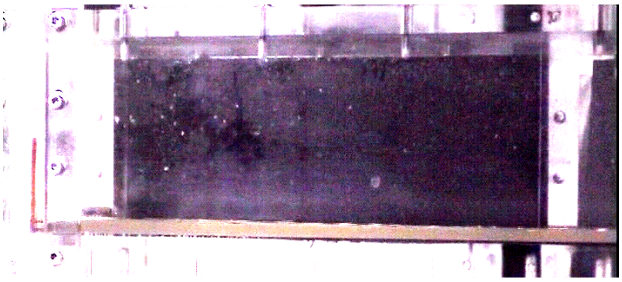

a) u_{LS} = 0.005 m/s, Fr_0 = 0.25

u_{GS} = 5.1 m/s

Subcritical flow. Some small waves can be observed at the interface.

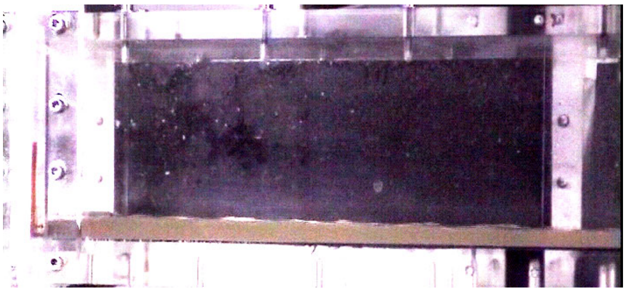

b) u_{LS} = 0.013 m/s, Fr_0 = 0.66

u_{GS} = 5.1 m/s

The wave pattern becomes rough as the liquid volumetric flow rate is increased.

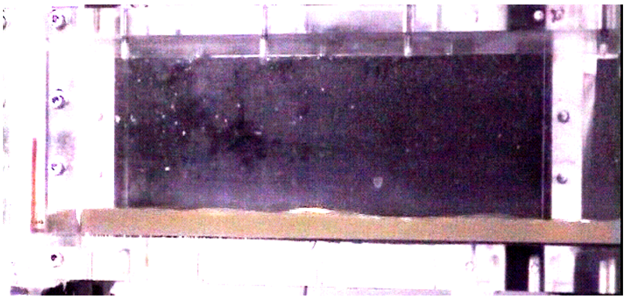

c) u_{LS} = 0.021 m/s, Fr_0 = 1.03

u_{GS} = 5.1 m/s

The liquid film depth increases and reaches the critical depth. The hydraulic jump is imminent.

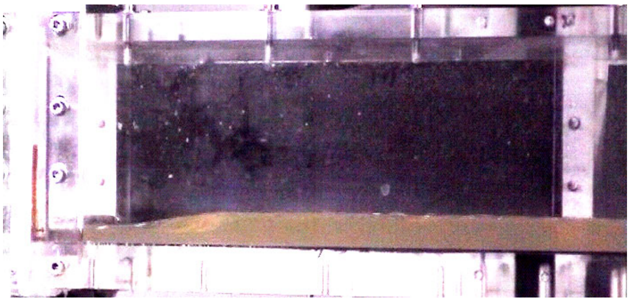

d) u_{LS} = 0.021 m/s, Fr_0 = 1.03

u_{GS} = 5.1 m/s

A hydraulic jump progresses downstream. The first part of the liquid film flows already supercritically.

e) u_{LS} = 0.025 m/s, Fr_0 = 1.24

u_{GS} = 5.1 m/s

The hydraulic jump moves downstream.

f) u_{LS} = 0.030 m/s, Fr_0 = 1.49

u_{GS} = 5.1 m/s

The hydraulic jump reaches a stable position in the test section.

Fig. 4.9. Occurrence of a hydraulic jump at the beginning of the test section.

d) Curve Onset of Partially Reversed Flow (OPRF)

Concerning the slope of the curve transition between stable countercurrent flow and partially reversed flow (curve OPRF), two different regions can be recognized:

OPRF Curve with Negative Slope

There is a region of the curve OPRF with negative slope corresponding low superficial liquid velocities, (Region A - B, see Fig. 4.10). This region with negative slope coincides with the subcritical liquid film region and part of the hydraulic jump region. The curve decreases until a minimum superficial gas velocity is reached (Point B, see Fig. 4.10). The minimum superficial gas velocity that can cause the breakdown of stratified countercurrent flow is always visible in all four cases in the hydraulic jump region.

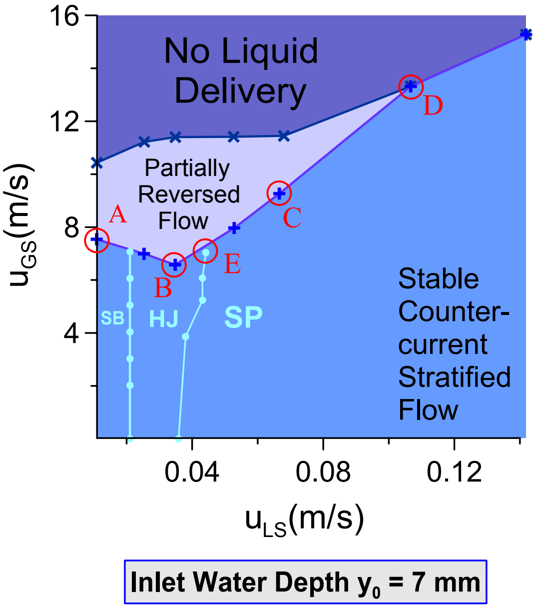

Fig. 4.10. Different regions of the curve OPRF.

<u>OPRF Curve with Positive Slope</u>

From the minimum superficial gas velocity on, the curve OPRF increases almost linearly with positive slope. The superficial gas velocity, at which the breakdown of stable countercurrent flow occurs, increases with increasing superficial liquid velocity. This region is always visible in the supercritical flow region.

The curve that represents the transition between supercritical film flow and flow with a hydraulic jump is an inclined curve with positive slope that converges to the curve OPRF. This means that a maximum liquid superficial velocity exists for which a stable hydraulic jump can occur in the test section (point E, Fig. 4.10). For superficial liquid velocities higher than that corresponding to point E, the onset of a hydraulic jump in the test section coincides with the OPRF from supercritical flow. This is an important issue when predicting analytically the onset of reversed flow from a supercritical flow, since a transition to subcritical flow is a necessary condition for reversed flow (see chapter 4.1.2).

The fact that the curve has two different slopes depending on the Froude number of the liquid film is an indicator that two different mechanisms are responsible for the onset of partially reversed flow. This will be discussed in chapter 4.1.2 (page 77). In the following sections, the flow phenomena at this transition will be described in more detail.

e) Transition from Supercritical Flow to Partially Reversed Flow

Reversed flow in an initial supercritical flow was always associated to a previous transition of the liquid film to subcritical flow. Thus, a direct transition from supercritical flow to reversed flow was not observed. The transition was only possible if the supercritical flow changed to subcritical flow through a hydraulic jump that was generated at the end of the test section and progressed beyond the liquid inlet plate, leading to reversed flow. It can be concluded, that the onset of a hydraulic jump coincides with the onset of reversed flow for supercritical flows. The transition is shown in several consecutive images in Fig. 4.11. An inlet liquid depth of 9 mm was employed. The liquid flow rate was kept constant and the gas flow rate was increased progressively.

The phenomenon observed in these cases was a highly turbulent, wavy interface, as soon as the hydraulic jump occurred. Liquid atomization was always observed during the transition. However, only a reduced fraction of the liquid was entrained. High speed pictures of the flow showed that the entrainment volumetric flow rate was insignificant. Thus, liquid entrainment cannot be taken into consideration as a cause of liquid delivery reduction.

The transition to partially reversed flow was a hysteresis dominated transition, especially, if the flow was initially supercritical. For example, a countercurrent stratified flow with an inlet liquid depth of 11 mm and a superficial liquid velocity of 0.09 m/s (inlet Froude number Fr_0 = 2.2) turned to reversed flow at a superficial gas velocity of approximately 8 m/s. If then the gas flow rate was reduced, the stable countercurrent stratified flow was not reached at a superficial gas velocity of 8 m/s but at 7 m/s.

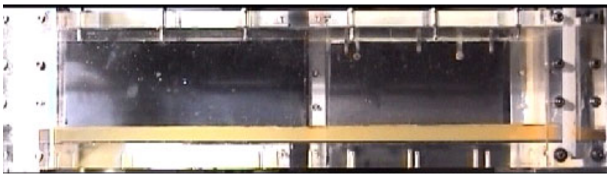

a) u_{LS} = 0.07 m/s, u_{GS} = 5.0 m/s

Supercritical flow. The interface is rather smooth.

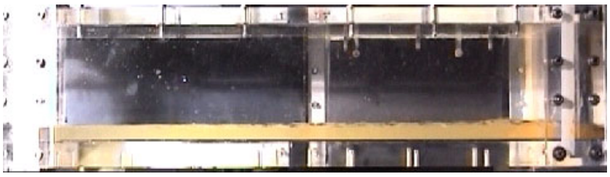

b) u_{LS} = 0.07 m/s, u_{GS} = 7.0 m/s

Supercritical flow with oscillating interface. The interface is smooth close to the liquid inlet but the roughness increases progressively.

c) u_{LS} = 0.07 m/s, u_{GS} = 8.6 m/s

The oscillating liquid depth reaches for only one instant the critical depth: a wave front develops. First droplets are entrained by the gas flow and deposit at the test section wall.

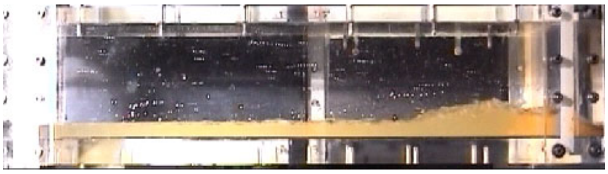

d) u_{LS} = 0.07 m/s, u_{GS} = 8.6 m/s

The wave front takes the form of a hydraulic jump advancing upstream.

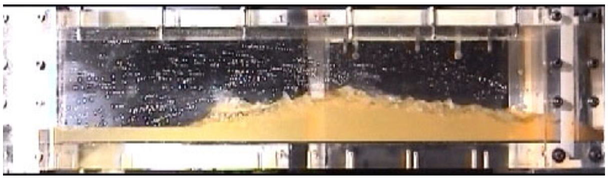

e) u_{LS} = 0.07 m/s, u_{GS} = 8.6 m/s

The hydraulic jump propagation velocity is high.

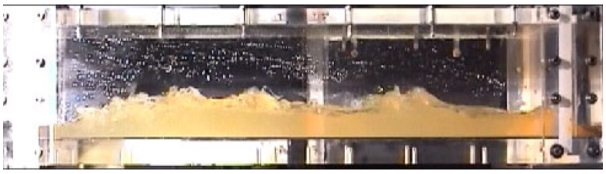

f) u_{LS} = 0.07 m/s, u_{GS} = 8.6 m/s

The hydraulic jump reaches the beginning of the test section. Partially reversed flow sets in.

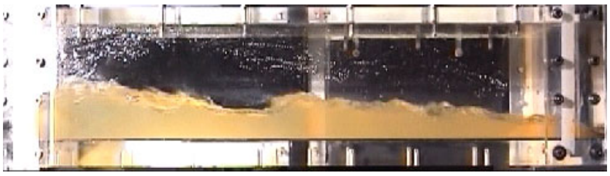

g) u_{LS} = 0.07 m/s, u_{GS} = 8.6 m/s

Partially reversed flow has fully developed.

Fig. 4.11. Onset of partially reversed flow.

f) Transition from Hydraulic Jump Flow to Partially Reversed Flow

This transition is very similar to the one described above. Initially, a hydraulic jump exists at a position $x = X_0$ in the test section. This is a stable position at the current liquid and gas mass flow rates (a hydraulic jump has a stable position only if a balance of fluid forces is established, see page 61). The transition to reversed flow occurs if either the gas flow rate is increased or the liquid flow rate is reduced, since this balance is broken in favour of the gas flow. Due to the drag force caused by the gas at the subcritical side of the generated jump, the hydraulic jump moves towards the liquid inlet and over the liquid inlet plate. In the test section reversed flow has set in. Again, hysteresis was observed.

g) Transition from Subcritical Flow to Partially Reversed Flow

As commented previously, the transition from subcritical flow to reversed flow is conditioned by the wave pattern of the interface. The transition occurs as soon as the amplitude of the waves at the liquid inlet is larger than the liquid inlet plate height and the waves propagate in the upstream direction (same direction as the gas flow). If these two conditions are fulfilled, then the upper part of the liquid film begins to flow upstream beyond the liquid inlet plate. These flow conditions correspond to the onset of reversed flow. Hysteresis was also observed during this transition.

h) The Curve Onset of Totally Reversed Flow (OTRF)

Fig. 4.1 (see page 58) presents the curve OTRF for all inlet liquid depths investigated in the WENKA test facility. The slope of the curve decreases progressively as the liquid inlet depth increases. For low liquid inlet depths (3 and 7 mm), the superficial gas velocity yielding totally reversed flow increases with increasing superficial liquid velocity. In some cases, the curve reaches a plateau, where the superficial gas velocity remains approximately constant (see Fig. 4.12, inlet depth 7 mm). In other cases, this plateau is not observed. As an example of flow regime maps including this plateau-region, flow regime maps for a liquid inlet depth of 3 and 7mm are shown in Fig. 4.12.

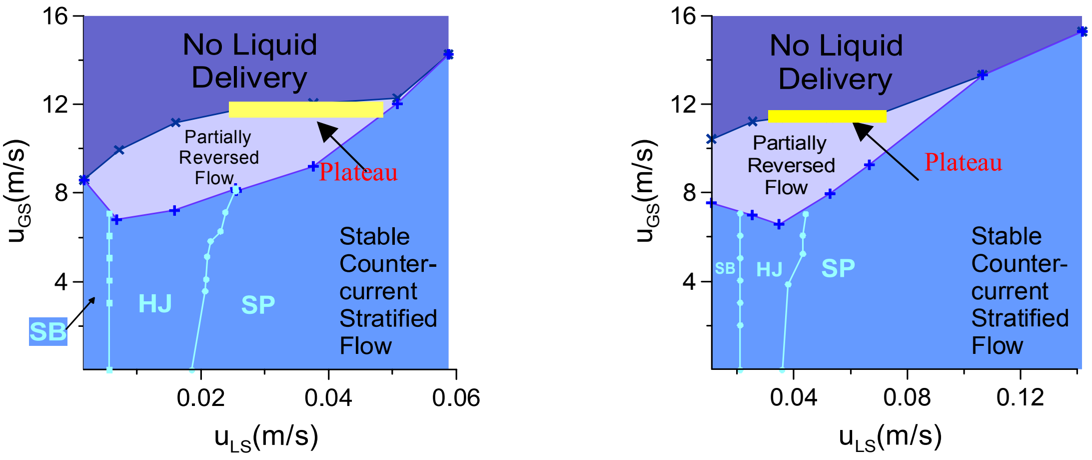

Inlet Water Depth y_0 = 3 mm

Inlet Water Depth y_0 = 7 mm

Fig. 4.12. Onset of totally reversed flow with plateau.

For liquid inlet depths higher than 7 mm, the slope of the transition curve becomes slightly negative. This effect is observed for large values of y_0: for y_0 > 7mm, the cross sectional area available for the gas flow close to the position $x = 0$ reduces considerably due to turbulence, air entrainment and splashing as soon as partially reversed flow sets in.

In many cases, the flow path available for the gas is almost blocked at $x = 0$. A turbulence induced slug flow has occurred. As an example, some images are presented in Fig. 4.13. The first images correspond to flow conditions with fully developed partially reversed flow and the latter to flow conditions with fully developed totally reversed flow. From the first image to the last one, the air flow rate was increased progressively. Intermediate stages are present passing from the first state to the last one.

The obstruction of the air flow path at the beginning of the test section is caused by the injected liquid that flows reversely right after the injection point. This situation is reached progressively, as the air flow rate is increased.

Fully developed partially reversed flow.

Partially reversed flow with imminent totally reversed flow.

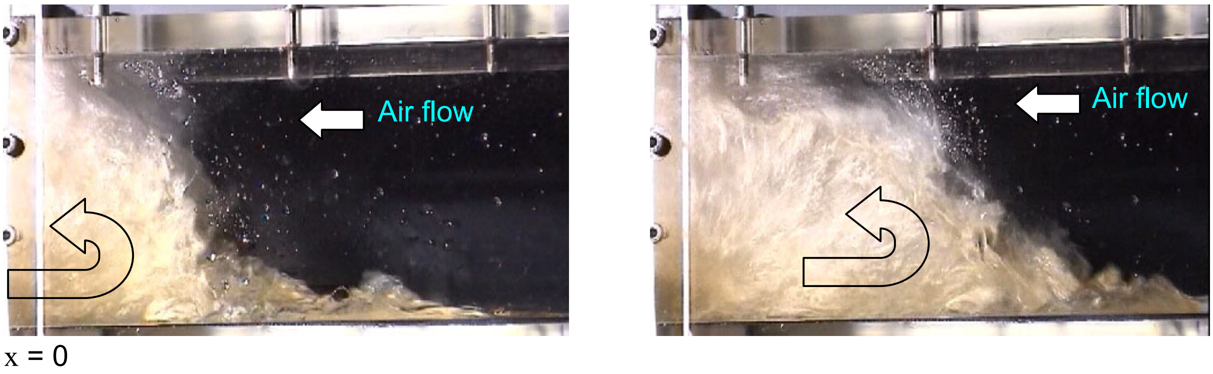

Fully developed totally reversed flow yielding air flow path obstruction.

Fig. 4.13. Different stages between partially and totally reversed flow showing cross section blockade.

In Fig. 4.14 the gas volumetric flow rate Q delivered by the blower is represented versus the pressure increase together with the head losses characteristic line (HLC). At a given blower's rotational speed n_1, a gas flow rate Q_1 is delivered causing a pressure increase P_1 in the test section, provided the head losses characteristic line of the facility is $HLC\ 1$. Before reversed flow sets in, the characteristic line for head losses in the test section changes only slightly, since oscillations at the interface in supercritical flow do not modify significantly the resistance line. Starting in the curve $HLC\ 1$ at a point 1 with a given air flow rate Q_1 and a given pressure increase P_1, the air mass flow rate can be increased up to a value Q_2 by increasing the blower's rotational speed from n_1 to n_2. The corresponding increase of pressure is represented by P_2 ($P_2 > P_1$). Thus, an increase of the blower's rotational speed moves the system from point 1 to point 2, and yields an increase in air flow rate. However, due to the fact that partially reversed flow causes a blockade of the gas flow, the resistance against the gas flow increases considerably. As a consequence, the characteristic line of head losses in the test section changes abruptly as soon as partially reversed flow sets in. There is a transition from the head losses characteristic line HLC 1 (in orange) to the line HLC 2 (in green), which is a line with a considerable slope. The blower responds to this change instantaneously, and the operation point moves from point 2 to the new equilibrium point 3, and in doing this, the air flow rate is reduced automatically down to the value Q_3 ($Q_3 < Q_1$). Now, we can try to increase the volumetric flow rate by increasing the blower's rotational speed, but due to the large curve slope, a large increase in rotational speed is needed to obtain a slight increase in air flow rate (Q_4).

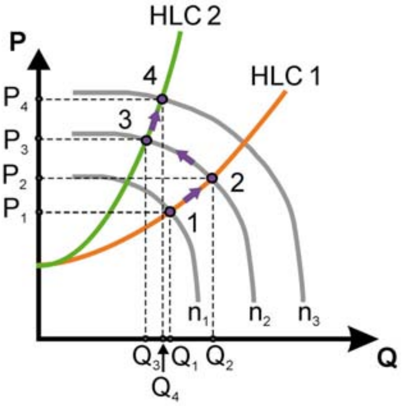

Fig. 4.14. Schematic representation of blower response when changing the head losses characteristic line of the test section.

As a result of the effect described above, the curve OTRF has a negative slope for large values of y_0. Large values of y_0 tend to show channel obstruction phenomena close to the liquid injection point and, as soon as the air flow path is blocked, the head losses characteristic line of the facility changes drastically to a new one with larger slope. The system response is to progress to a new equilibrium point, what reduces the air flow rate even if the rotational speed is increased. According to this, the gas superficial velocity needed to cause totally reversed flow decreases progressively with increasing superficial liquid velocity. An increase of the liquid superficial velocity or of the inlet liquid depth increments this effect even more.

i) Transition from Partially Reversed Flow to Totally Reversed Flow

The mechanism yielding totally reversed flow onset is based on liquid film dry out. Experiments show, that the liquid film cannot maintain its depth at any gas velocity. During partially reversed flow the lower part of the liquid film flows still in the initial direction, while the upper part is swept in the air flow direction and has negative velocities. However, the region that still holds positive liquid velocities thins progressively as the fraction of liquid flowing reversely increases. At a sufficiently high gas velocity, the liquid film at the end of the test section is interrupted and totally reversed flow sets in. A *dry zone* exists in the channel (see Fig. 4.15). The liquid film depth tends progressively to zero as it approaches this zone.

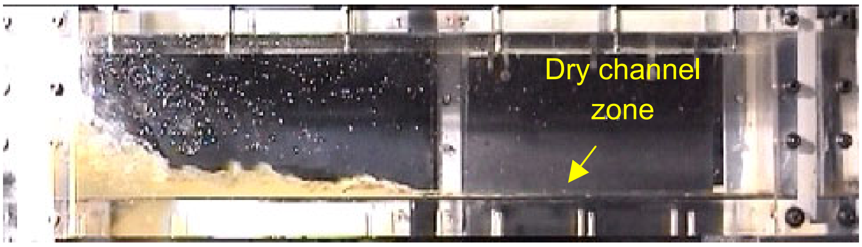

Fig. 4.15. Totally reversed flow with dry channel zone.

The transition from partially reversed flow to totally reversed flow is presented in Fig. 4.16. In these images the progressive obstruction of the gas flow path can be observed.

Once totally reversed flow occurs and the channel is blocked, a further increase of the liquid mass flow rate cannot re-establish stratified flow. A strong hysteresis effect is observed. Instead of increasing the liquid flow rate, a depressurization of the channel is recommended to restore liquid penetration.

a) Partially reversed Flow. Large amplitude waves are present at the interface.

b) The flow path available for the gas is reduced at the liquid injection point due to the constructive interference between large amplitude waves and the injected liquid.

c) Occurrence of roll waves that break at the liquid injection point, splashing and air entrainment generate a blockade.

d) The volumetric flow rate of gas delivered by the blower is automatically reduced due to an increase in head losses.

e) The liquid film depth thins progressively. This effect is much more important at the end of the test section than at the beginning.

f) The back flow ratio increases considerably as the liquid film depth reduces.

g) The liquid film dries out at the end of the test section: no liquid delivery occurs.

Fig. 4.16. Onset of totally reversed flow.

4.1.2 Reversed Flow: A Novel Criterion for Onset of Flow Reversal

As flow reversal is not possible as long as the flow remains supercritical, the hydraulic jump criterion defines a necessary constraint for which flow reversal will not occur in a horizontal channel under countercurrent flow conditions. Even if a hydraulic jump occurred, however, the flow has not necessarily to be reversed. A second criterion exists that must be fulfilled for the onset of partially reversed flow.

Experimental observations in the WENKA test facility have shown, that flow reversal occurs in countercurrent horizontal flow only if the liquid flow is subcritical and the Wallis criterion for onset of flow reversal as proposed by Richter

$$u_{LS}^{*\,1/2} + u_{GS}^{*\,1/2} = C \tag{4.2}$$

is fulfilled.

Richter proposed a value of $C = 0.7$. In the WENKA test facility flow reversal was observed for values of the Wallis constant C starting from 0.6 - 0.7. In Fig. 4.17 the onset of partially reversed flow for an inlet water depth of 9 and 3 mm is presented. Here, the value of the Wallis constant is plotted versus the ratio $y_A / y_{A,C}$, where y_A is the water depth at the end of the channel and $y_{A,C}$ is the critical water depth, for which the Froude number at the end of the channel is equal to unity. The transition from supercritical flow to partially reversed flow happens indeed as soon as the ratio $y_A / y_{A,C}$ is equal to unity (transition from supercritical to subcritical flow) and the Wallis condition for flow reversal is fulfilled. Note that experimental points exist for which the transition occurs at values of the Wallis constant larger than 0.7. For these points, the value $C = 0.7$ is reached before $y_A / y_{A,C} = 1$, and flow reversal was observed for values of C larger than 0.7, since the condition of subcritical flow was not fulfilled. It can be concluded, that the Wallis correlation cannot be applied to supercritical flow ($y_A < y_{A,C}$).

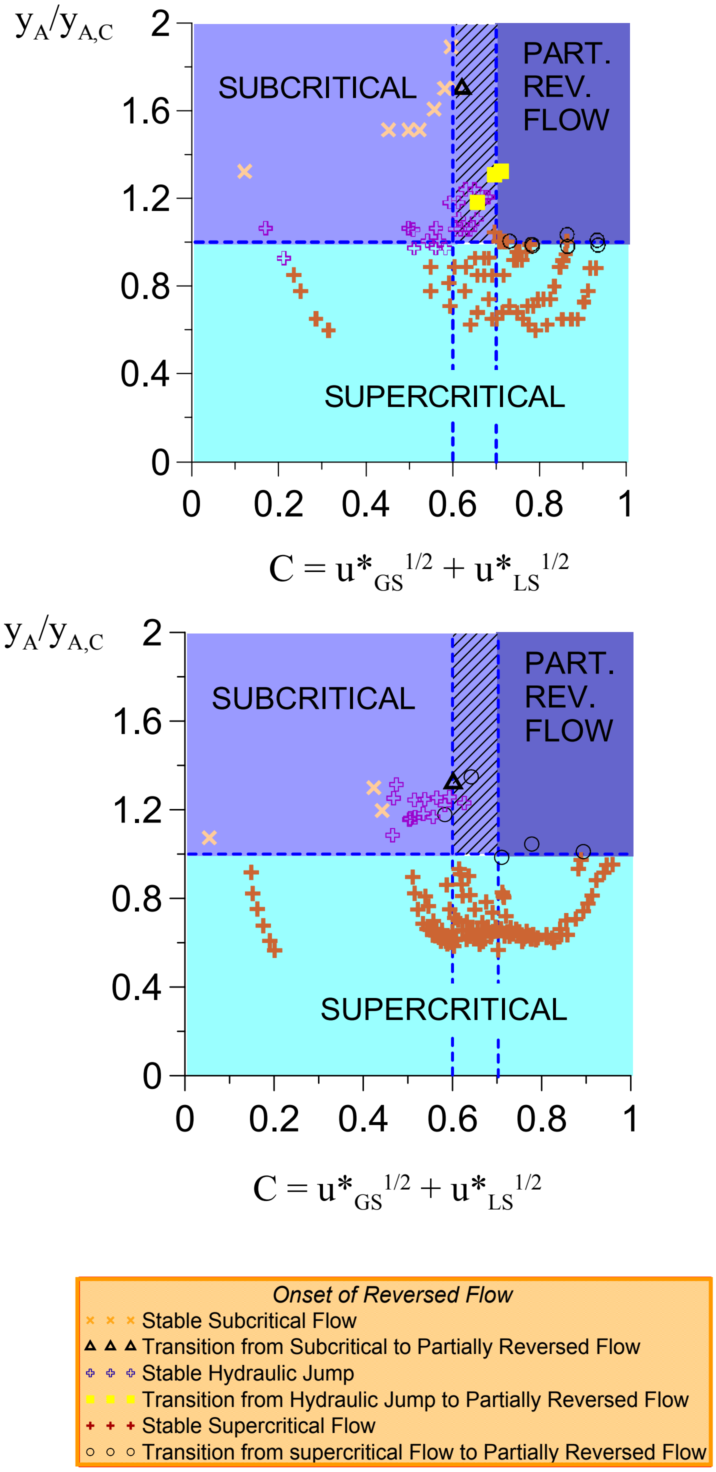

Fig. 4.17. Flow reversal using an inlet water depth of 9 (above) and 3 mm (below).

In case of subcritical flow, however, the Wallis correlation can indeed be applied. Experiments with subcritical flow showed, that the Wallis constant ranges between 0.6 and 0.7.

Consequently, starting with a countercurrent flow, the liquid flow will at least be partially reversed if

$$u_{LS}^{*\,1/2} + u_{GS}^{*\,1/2} \geq 0.7 \quad \text{and} \quad \frac{y_A}{y_{A,C}} \geq 1 \tag{4.3}$$

The flow will only be reversed if both of these two criteria are fulfilled. Note that the liquid inlet conditions which lead to $y_A = y_{A,C}$ at the outlet can be determined with equation (3.31).

The liquid depth increases in the liquid flow direction although it has always a value lower than the critical depth, for which the Froude number at the water outlet is equal to unity. Thus, the ratio $y_A / y_{A,C}$ increases in the channel and gets closer to unity. This change in liquid depth depends not only on the inlet Froude number of the liquid but also on the gas superficial velocity. Typically, the liquid depth increases only a few millimeters. Note that this change in liquid depth can be estimated for supercritical flows using equation (3.27) as was shown in chapter 4.1.1a) (see page 57).

As soon as the gas velocity is increased up to a value that leads to a liquid depth at the water outlet position equal to the critical height, a transition to subcritical flow in form of a hydraulic jump occurs. The jump is generated at the end of the channel, where the critical depth is reached first.

4.1.3 Liquid Back Flow Ratios

Measured back flow ratios obtained experimentally are presented in Fig. 4.18 versus the gas velocity at the gas inlet section $u_{G,IN}$. As this gas velocity is calculated with the whole channel cross section it is equivalent to the superficial gas velocity in the two-phase region.

For a given inlet water depth and a given inlet Froude number, the back flow ratio depends primarily only on the gas velocity $u_{G,IN}$. If the gas velocity is increased, the back flow ratio increases also. However, a minimum gas velocity exists under which no reversed flow occurs, and therefore, the back flow ratio is equal to zero. This minimum velocity, $u_{G,IN\ min}$, is the gas velocity at the onset of reversed flow as described above by Eq. (4.3). As soon as this velocity is reached, values of b greater than zero are measured instantaneously.

Fig. 4.18 (first diagram) shows that the inlet Froude number influences the value of $u_{G,IN\ min}$. The higher the inlet Froude number, the higher is the minimum velocity required for occurrence of reversed flow as to be expected from equation (3.31). Once flow reversal has started, however, the Froude number has only minor influence on the back flow ratio. The back flow ratio increases almost linearly with the gas velocity, also in case of other liquid depths, as shown on the lower part of Fig. 4.18.

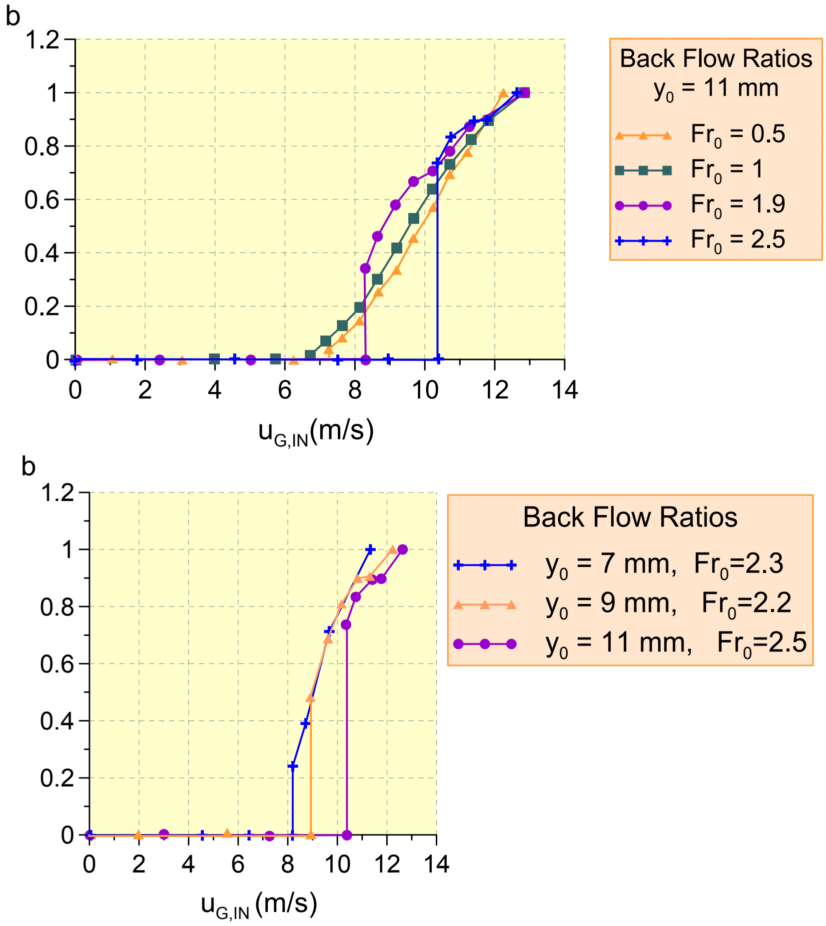

Fig. 4.18. Back flow ratios.

Above: Inlet water depth of 11 mm for different inlet Froude numbers.

Below: Constant inlet Froude number of 2.2 with varying inlet water depth.

Since in all likelihood the Froude number and the gas velocity turned out to be representative for the water delivery rates, it was intended to correlate empirically the back flow ratios with the inlet Froude number and the gas Reynolds number, estimated with $u_{G,IN}$. A data bank of back flow ratios obtained in approximately 84 experiments was employed. With a multiple linear regression model, the back flow ratios can be predicted by means of a correlation of the form:

$$b = n + k \cdot Fr_0 + d \cdot Re_{G0} \tag{4.4}$$

Where n, k and d are constant coefficients, b is the back flow ratio, Fr_0 the inlet Froude number and Re_{G0} is the gas Reynolds number estimated with $u_{G,IN}$.

The best fit to the experimental data (95.5% fitted) was given by the equation:

$$b = -1.22 + 0.09 Fr_0 + 2.88 \times 10^{-5} Re_{G0} \qquad \text{if} \qquad 0 \le b \le 1 \quad \text{and Eq. (4.3) is exceeded} \tag{4.5}$$

Fig. 4.19 shows experimental values of b versus those predicted by equation (4.6). Good agreement is obtained between predicted and experimental back flow ratios. However, this is an empirical correlation, obtained for a certain range of values of Fr_0 (between 0.5 and 3) and Re_{G0} between $3.6 \cdot 10^4$ and $8.0 \cdot 10^4$. Extrapolations may lead to higher uncertainties than those shown in the figure.

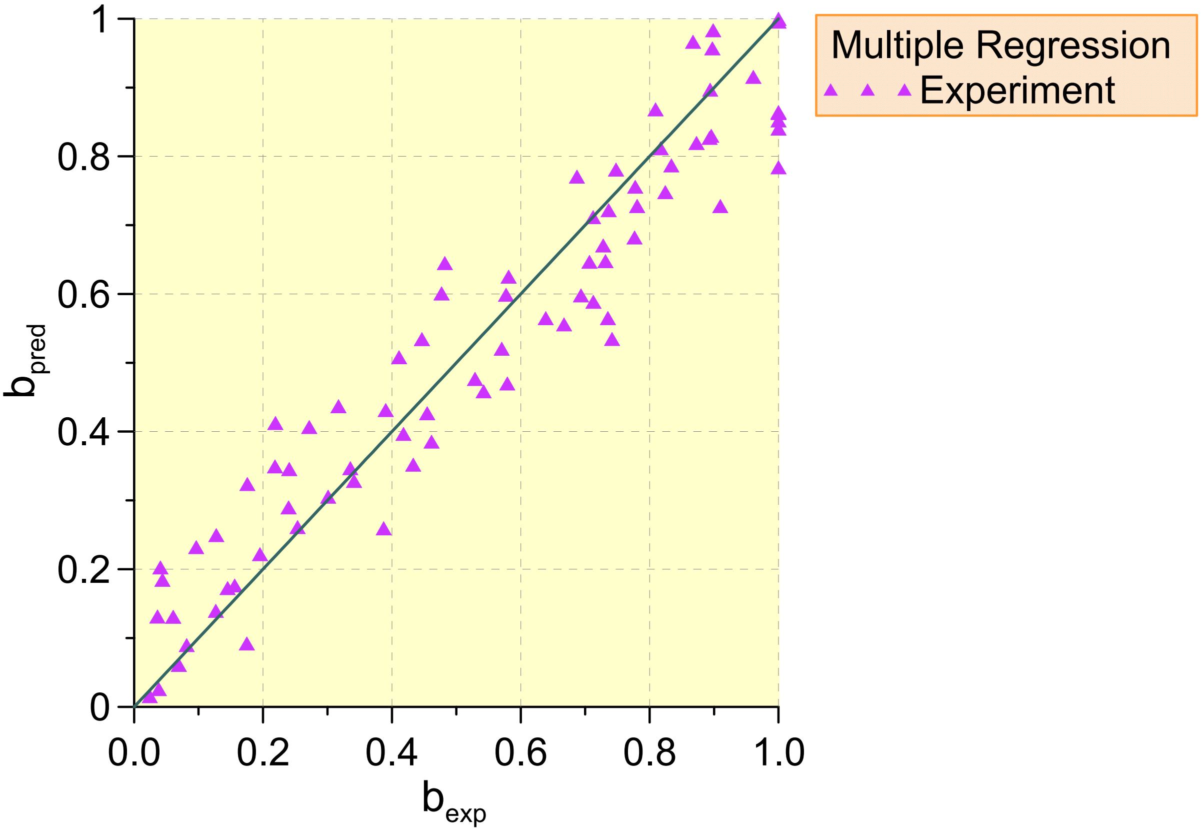

Fig. 4.19. Back flow ratio prediction by means of linear multiple regression.

4.2 Local Measurements

4.2.1 Local Air Velocities

a) Effect of Seeding Flow (Secondary Flow)

In chapter 2.2.6a) (see page 42) the PIV technique was presented. It was pointed out, that this measurement technique needs the introduction of tracer particles in the flow to acquire local velocities. The tracer particles employed to measure air velocities were generated by an oil seeding generator. Thus, an additional flow of air at low pressure and oil particles was always mixed with the main flow in the test section (see Fig. 2.8, page 44).

To investigate the possible influence of this additional flow on the main flow in the test section, some pre-tests were performed. In these experiments, the air flow introduced by the seeding generator was studied. No air was provided by the blower, only the air flow delivered by the seeding generator was introduced in the test section.

Fig. 4.20 presents a velocity profile of this additional flow obtained from 50 PIV images. The vertical position within the channel is designated as h (local height).

As an example, one of the PIV vector fields is shown in Fig. 4.21. The pressure delivered by the particle generator was 0.5 bar. A lower injection pressure would have reduced the influence of the additional flow on the air velocities. However, lower injection pressures yielded difficulties concerning seeding density: the tracer particles volumetric concentration was acceptable at the center of the flow cross section, but insufficient close to the walls.

Using an injection pressure of 0.5 bar, the velocities profile presents a maximum velocity of 0.43 m/s that is reached at the center of the vertical axis, at a local height, h, of approximately 45 mm. The velocity decays rapidly as it approaches to the channel walls, as usual in a laminar flow profile. Nevertheless, the profile presented here is has a strong peak, since the injection of tracer particles was performed in the center of the channel cross section (see Fig. 2.8, page 44). As a result, the flow presents higher velocities at the center region of the profile.

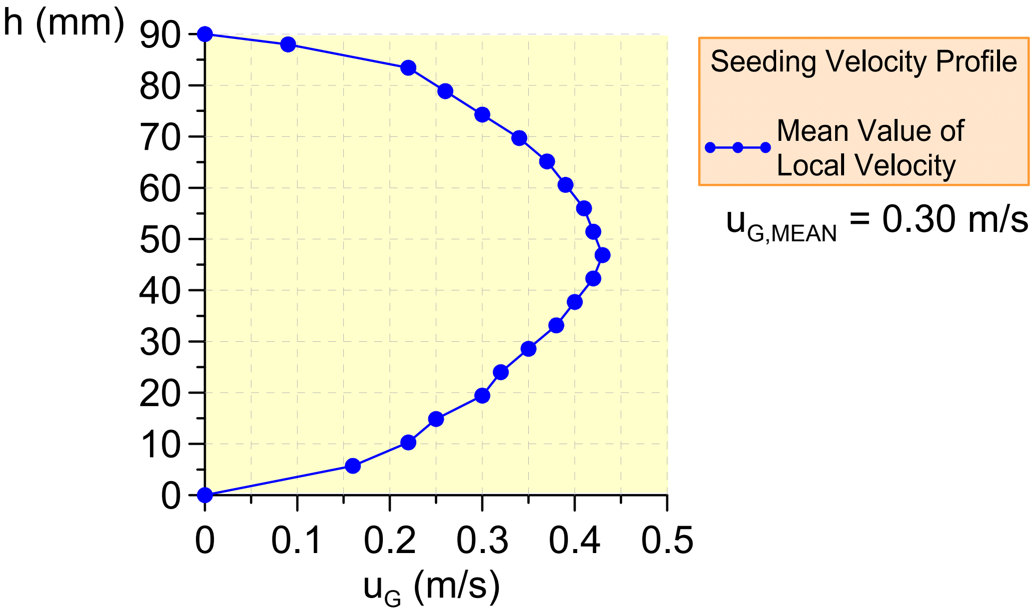

Fig. 4.20. Additional flow velocity profile due to seeding introduction.

The profile presented in Fig. 4.20 yields the conclusion that the velocity profiles obtained in the test section are only slightly influenced by the additional flow introduced to inject the seeding. A maximum increase in velocity up to a value of 0.43 m/s is possible due to the secondary flow. This effect is less important at the channel wall.

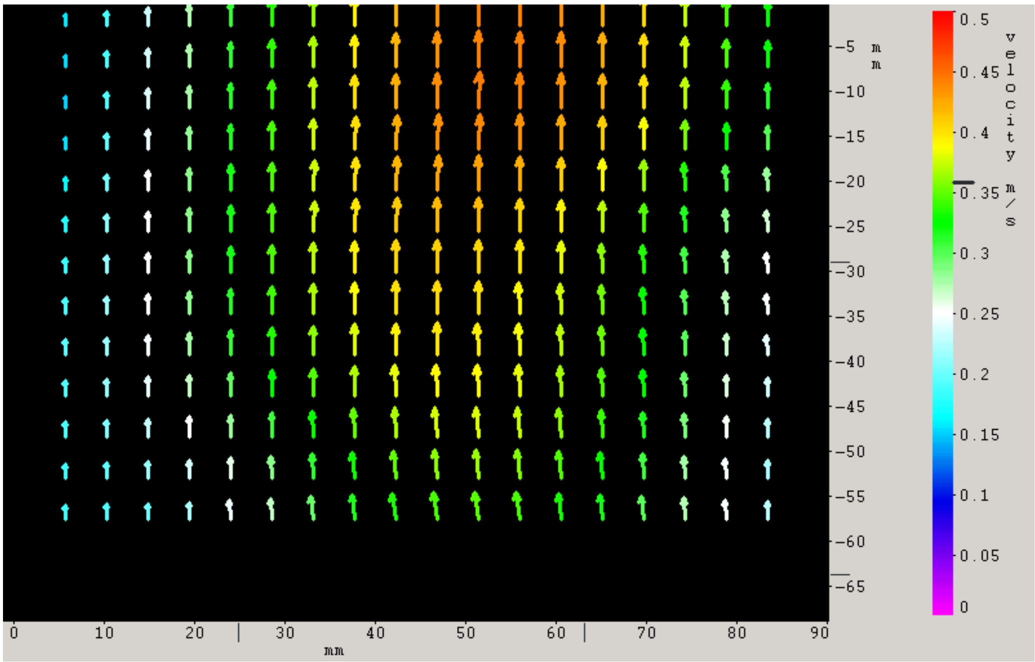

Fig. 4.21. Secondary flow vector field obtained by means of PIV.

b) Air Velocity Profiles

Fig. 4.22 shows velocity profiles obtained with PIV for single-phase air flow for mean velocities up to 15.4 m/s. The experimental data are presented in Table 11. A non-symmetric profile can be observed as a general feature for mean velocities larger than 12 m/s. For these velocities, the lower part of the profiles tends to zero much faster than the upper part. This may be an entrance effect due to the existence of the liquid inlet plate.

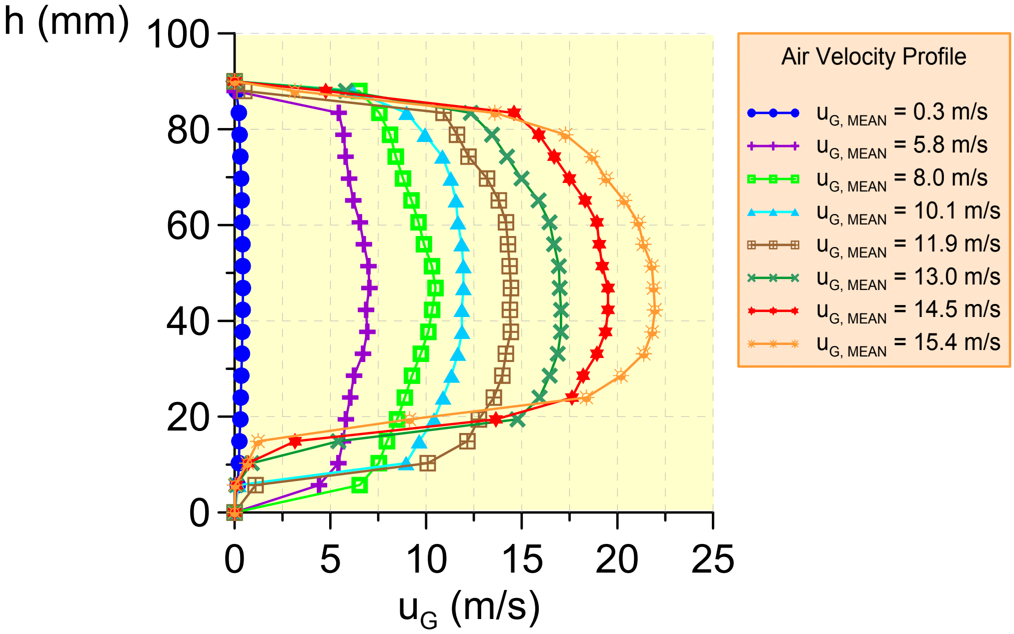

Fig. 4.22. Air velocity profiles (single-phase flow measurements) at x = 144 mm .

If the air flow rate is increased in the test section this effect becomes much stronger, so that the velocity reduces considerably at the lower part of the profile.

4.2.2 Local Liquid Film Velocities

a) Liquid Film with Stagnant Air

First PIV measurements of the liquid film were performed with stagnant air. To provide an illustrative example, three different cases are presented in Fig. 4.23 measured at position P2 (see Fig. 2.9, page 45) and using an inlet water depth of 16 mm:

- A subcritical flow (SB), with a liquid volumetric flow rate of 30 l/min and an inlet Froude number $Fr_0 = 0.7$. This flow presents the slowest mean velocity. The velocity profile is similar to those observed in open channel flow (for example, see [15]).

- A hydraulic jump flow (HJ), measured at its supercritical side (upstream of the hydraulic jump). The liquid flow rate was 61 l/min, corresponding to a value of $Fr_0 = 1.4$. The velocity profile presented was measured at the supercritical side of the jump, and for this reason, the water level is higher than that showed for the subcritical flow.

- A supercritical flow (SP), with liquid flow rate of 74 l/min and an inlet Froude number equal to 1.8, that presents again a profile typical of those observed in open channel flow.

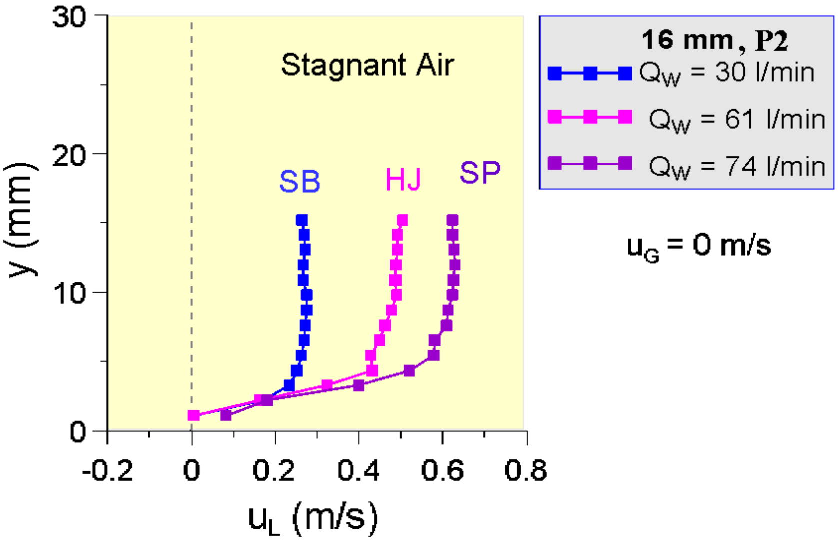

Fig. 4.23. Velocity profiles of liquid film with stagnant air.

Although there are small differences between the profiles, the liquid depth does not vary significantly from one case to another, since the interface between water and air is very stable for the case of stagnant air. The profiles develop progressively from low velocities (at the channel wall) to a nearly constant value that is reached beyond a liquid depth of approximately 5 mm.

Some difficulties arise when trying to measure the velocity vectors close to the interface. Fig. 4.24 shows an image of the liquid film illuminated by the laser light. The tracer particles can be easily recognized. The interface is recorded in form of a thick boundary layer as a result of superposition of different waves moving at different velocities and with different phases. In this region, the image of the tracer particles disappears, mixed with the background. This yielded to computation of false velocity vectors at the interface.

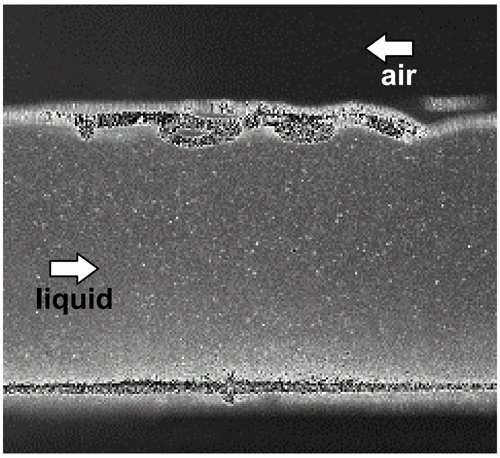

Fig. 4.24. Image of the liquid film illuminated by the laser.

In these cases, a special vector post-processing was employed to remove false vectors close to the interface. The results obtained with this method are presented in Fig. 4.25 and Fig. 4.26.

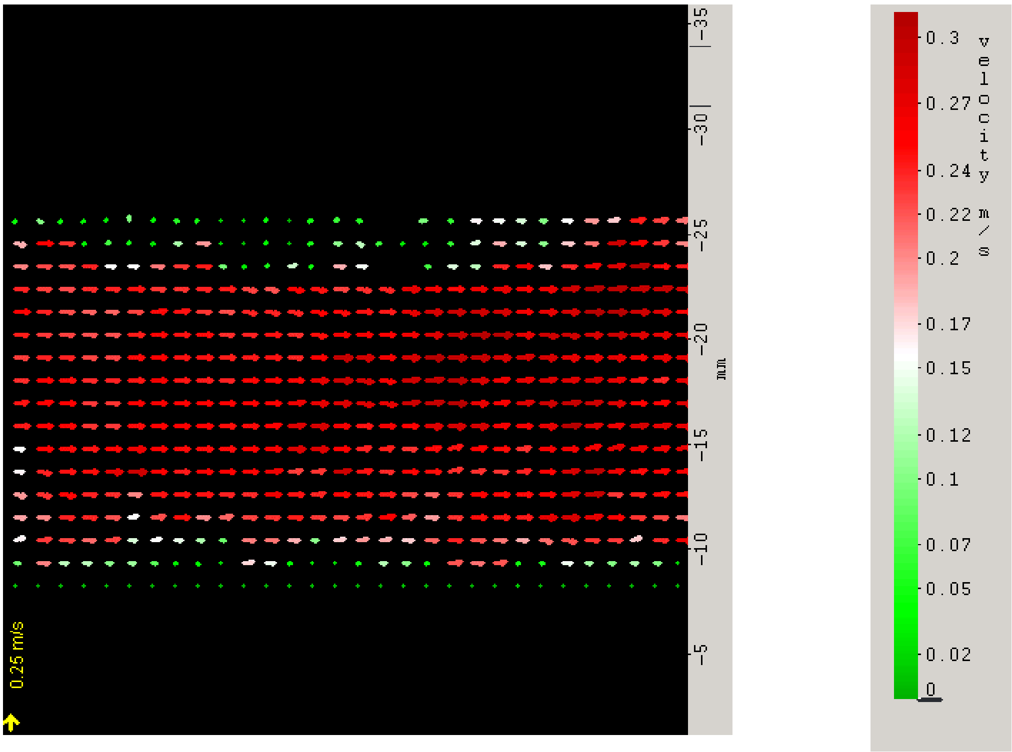

Fig. 4.25. Velocity field of liquid film after post-processing.

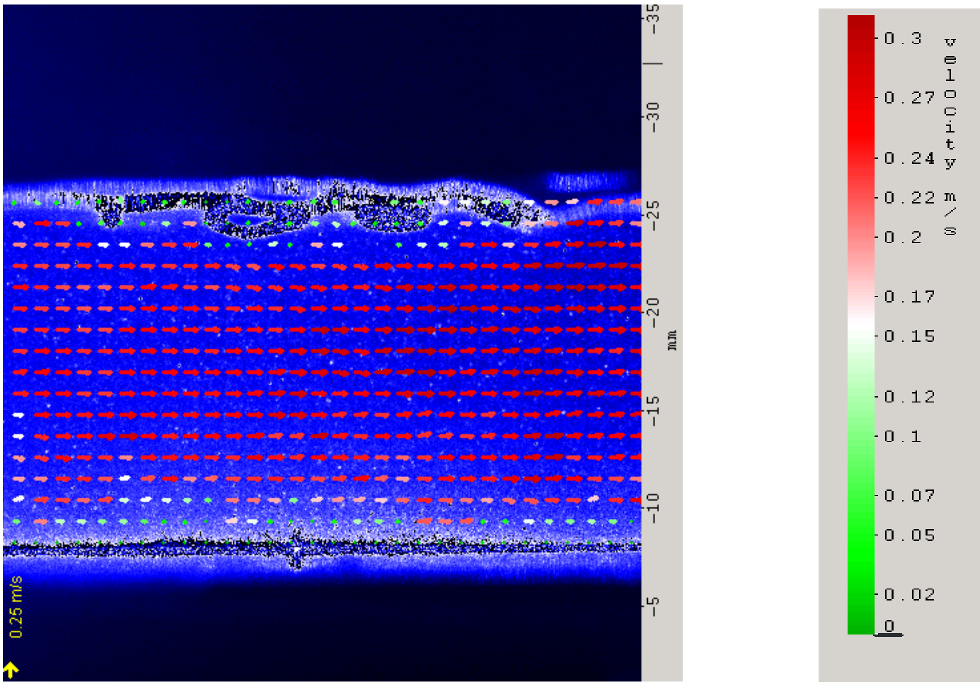

Fig. 4.26. Vector field with original image as background.

b) Liquid Film with Countercurrent Flow of Gas

Figure Fig. 4.27 presents velocity profiles of the liquid film with and without countercurrent flow of air obtained with PIV at Position P2 for an initial water level of 16 mm.

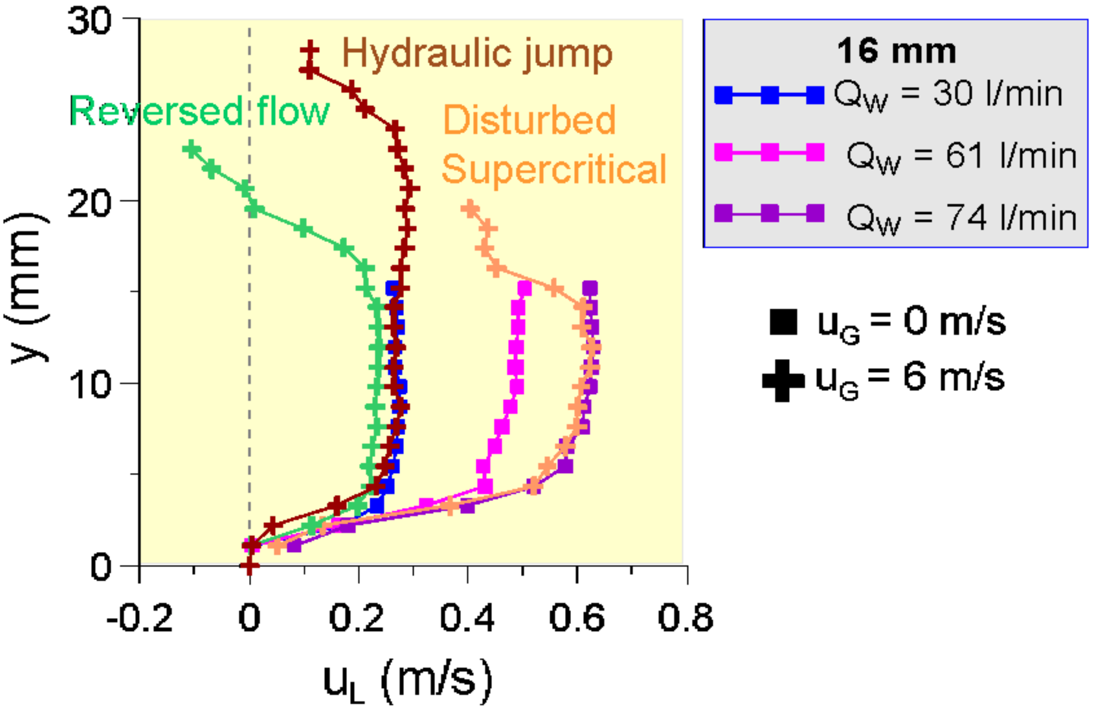

Fig. 4.27. Differences between velocity profiles of liquid film with stagnant air and those with countercurrent flow of air at 6 m/s.

In the right-side of the picture, the velocity profiles without air (squares) are represented as a reference for the profiles with air flow (crosses). If air flows countercurrently to the liquid film, with a velocity of 6 m/s, the following changes can be observed in the velocity profiles:

- The subcritical flow changes to partially reversed flow, the upper velocities of the profile become negative, whereas the lower part of the velocity profile does not seem to be disturbed by the countercurrent gas flow. Additionally, the water level increases, due to the wavy interface generated by the air flow. As an example, one of the 50 vector fields employed to compute the velocity profile presented in Fig. 4.27 is given in Fig. 4.28. Note that the upper part of the liquid film has negative velocity vectors (positive direction is the initial liquid film flow direction). Additionally, while the velocity vectors have mainly a horizontal direction in the lower part of the liquid film, the vectors at the interface are influenced by the wave dynamics at the surface. This effect is much stronger at lower superficial gas velocities for which turbulence eddies are generated at the upper part of the liquid film (see Fig. 4.29). High superficial gas velocities break these eddies in carrying the liquid film.

- The hydraulic jump (critical flow) is shifted by the air flow towards the water inlet section, and then remains at a certain position stable, so that the PIV system measures now the subcritical region just behind the jump. The velocity profile is shifted towards the velocity profile of the subcritical flow without air, but, since the subcritical side of the hydraulic jump has a higher water depth, the velocity profile is also higher and somewhat disturbed at the interface, due to the presence of the waves caused by the liquid-gas interaction.

- The supercritical flow presents also a disturbed velocity profile at its upper part. However, no negative velocities were measured. Velocities at the upper part of the liquid film are reduced by the gas flow but they remain positive.

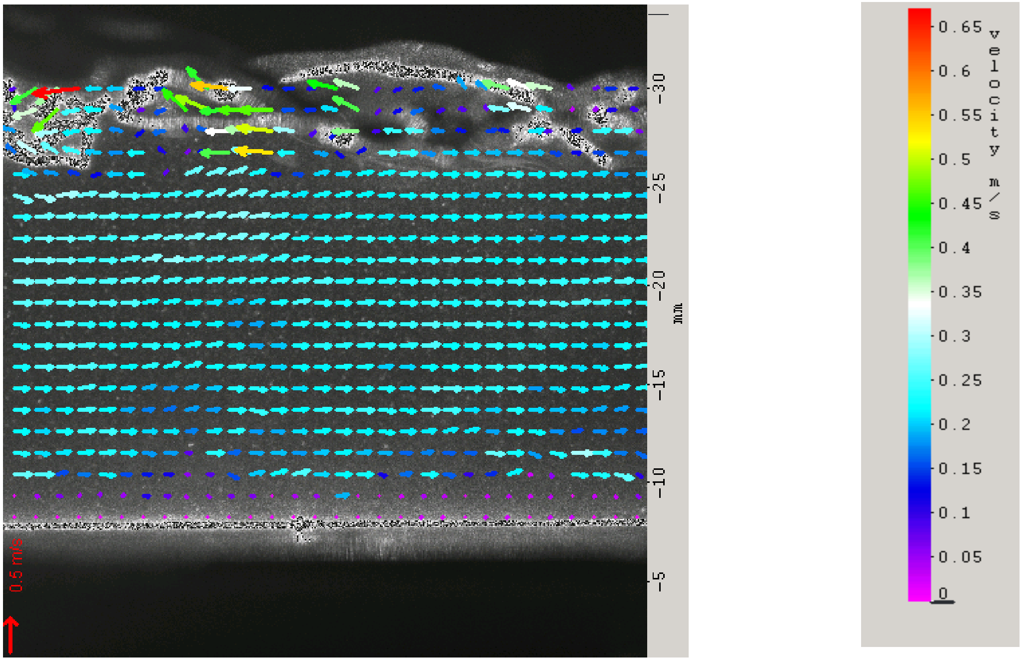

Fig. 4.28. Vector field with partially reversed liquid flow (superficial gas velocity 8 m/s)

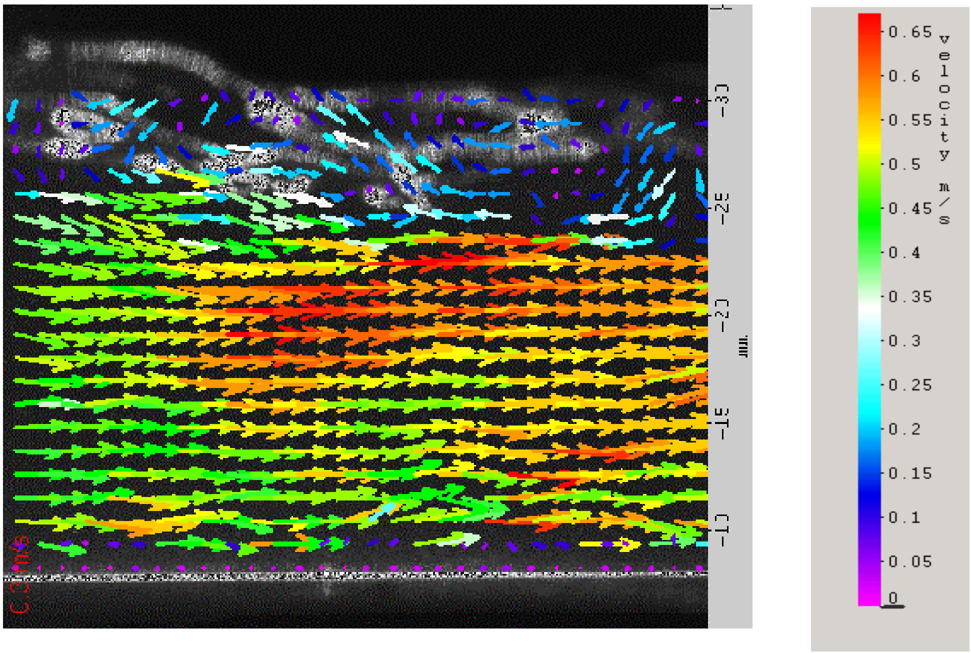

Fig. 4.29. Turbulence eddies at the upper part of the liquid film for reversed flow caused by a superficial gas velocity of 6 m/s.

For additional information about these PIV experiments, see the diploma thesis of Anglada [2].

4.2.3 Liquid Film Morphology

The morphology of the liquid film was investigated for selected experiments to obtain representative data on interface form, wave velocities, amplitudes and frequencies. Some examples of the results obtained in these experiments are presented in this section. The entire report can be found in the diploma thesis of Asla [5].

a) Calibration and Image Distortion

In order to extract the Cartesian coordinates of the liquid interface with the image processing software Optimas®, a calibration, including image distortion correction, was performed.

Fig. 4.30 shows a typical image of the liquid film flowing in the test section. Due to image distortion, the rectangular transparent side wall of the test section (blue rectangle) is recognized by the software as a distorted rectangle (red polygon).

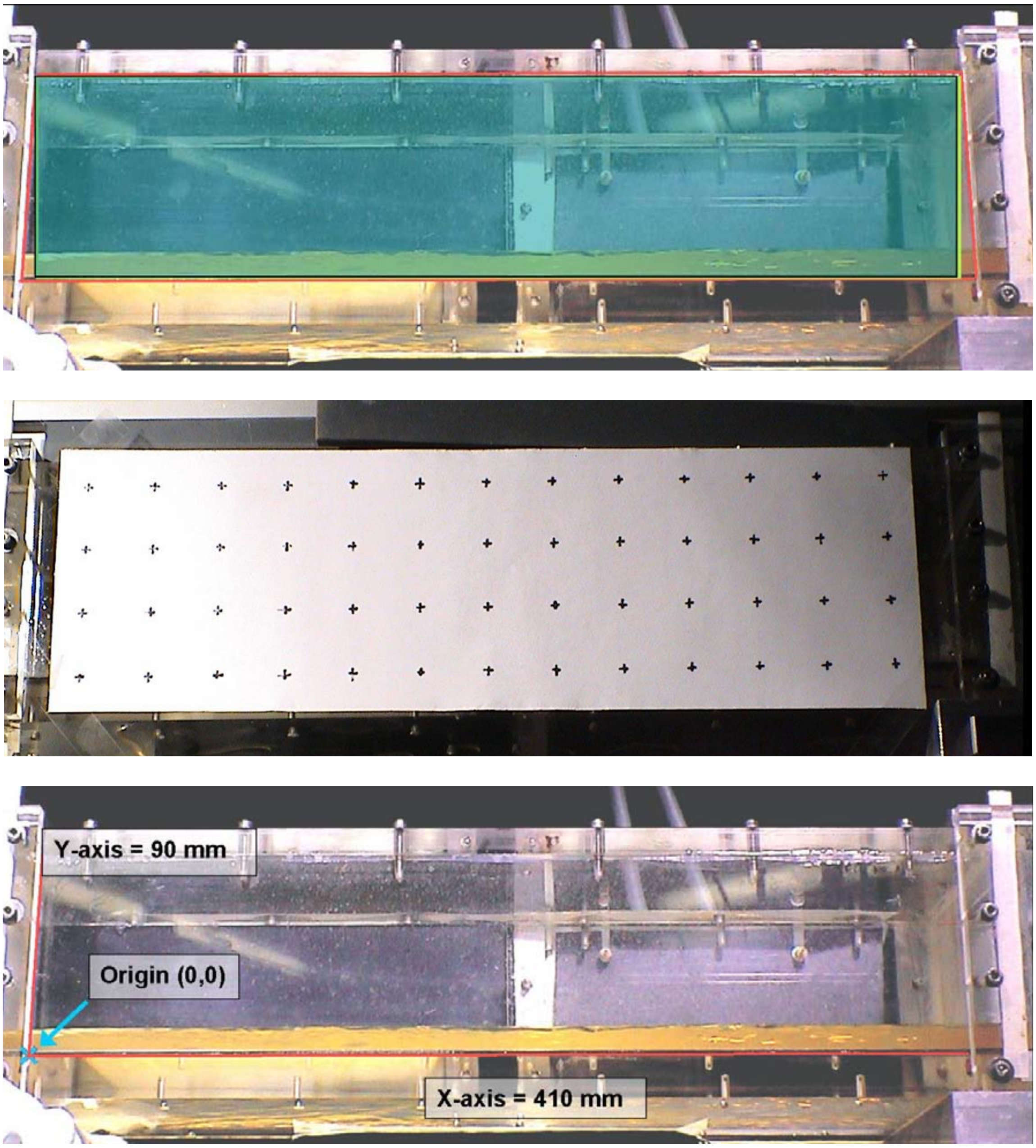

Fig. 4.30. The problem of image distortion and calibration applied to solve it.

The problem of image distortion was solved by placing a correction grid at the test section side wall and recording this image (see Fig. 4.30, center). The obtained image was used by a subroutine of Optimas® to eliminate distortion effects and compute the correct Cartesian coordinate values of any point in the image. Cartesian coordinates can only be given to a point if an origin is defined. The origin employed in all images was placed at the left lowest position of the channel bottom, as shown in Fig. 4.30 (third image).

In the next sections, examples of interface detection for a supercritical flow and for reversed flow are presented.

b) Supercritical Flow

The supercritical flow is one of the simplest cases to analyze due to its approximately smooth interface even if air is flowing countercurrently. Especial attention was given to the linear increase of the liquid depth in the water flow direction. Therefore, the supercritical surface waves present in the images were eliminated by means of running average and smoothing of the detected interface. Results obtained for an inlet liquid depth of 11 mm are presented in Fig. 4.31. The superficial liquid and gas velocities are 0.12 and 9.00 m/s respectively.

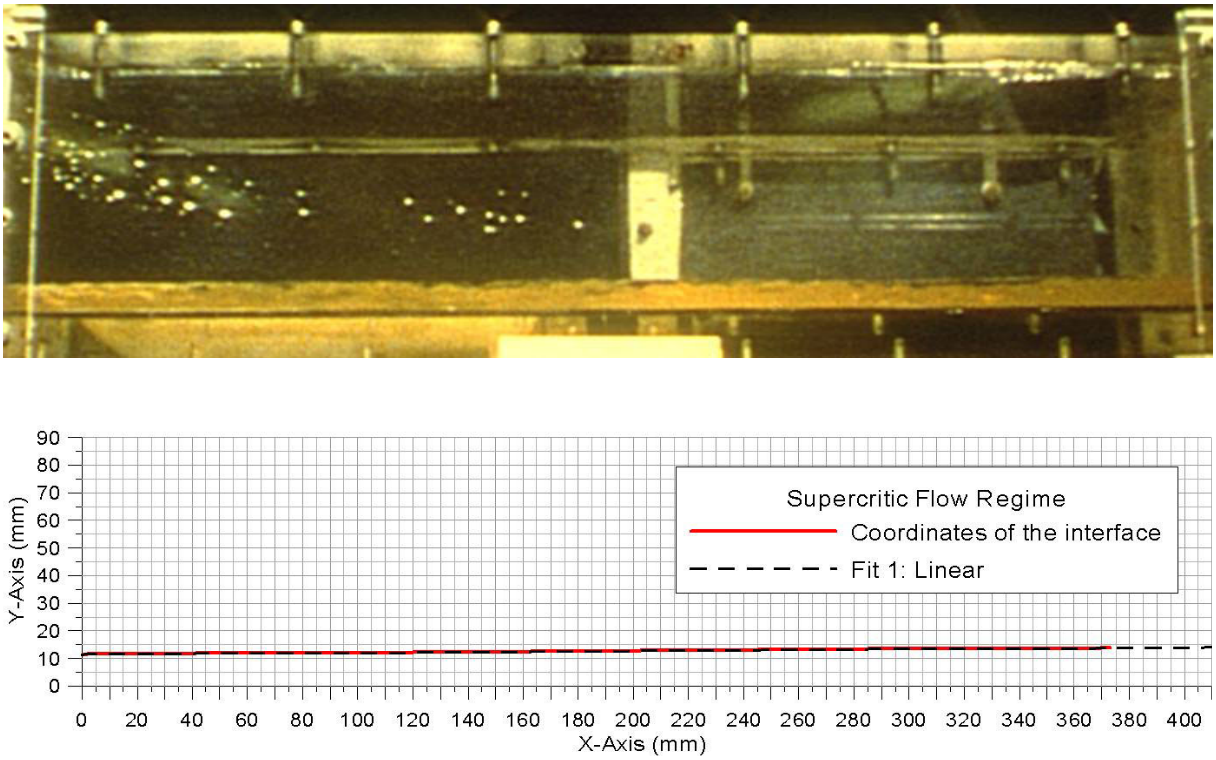

Fig. 4.31. Interface detection of a supercritical flow (u_{LS}= 0.12 m/s and u_{GS} = 9.00 m/s).

c) Onset of Partially Reversed Flow

The evaluation carried over for an image taken during partially reversed flow is presented in Fig. 4.32. The inlet water depth was 11 mm and the superficial liquid and gas velocities were 0.12 and 10.80 m/s.

During the experiments, the wavy character of the observed interface yielded a non-homogeneous interface pattern. Optical phenomena as light refraction and reflection were enhanced by the moving interface and some regions of the liquid film were recorded with a good contrast and other with a bad one. As a consequence, interface detection was complex and had to be optimized in a determined region of the acquired image. Usually, a division of the area of interest of the image in two was sufficient, in order to detect properly the interface in each of them separately. Afterwards, a post-processing was performed to merge data obtained in each image. For example, Fig. 4.32a shows an image for which indeed interface detection was performed in this way. The rest of the interface was detected defining a second area of interest and setting new detection criteria.

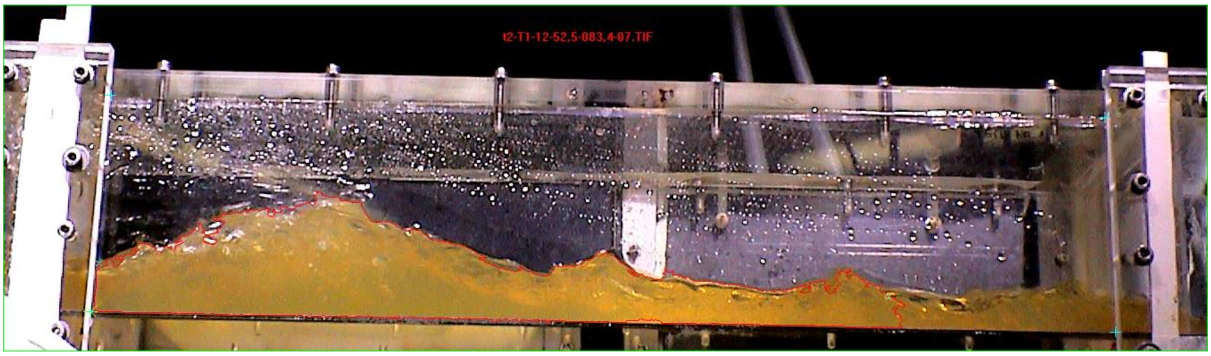

a) Interface detection.

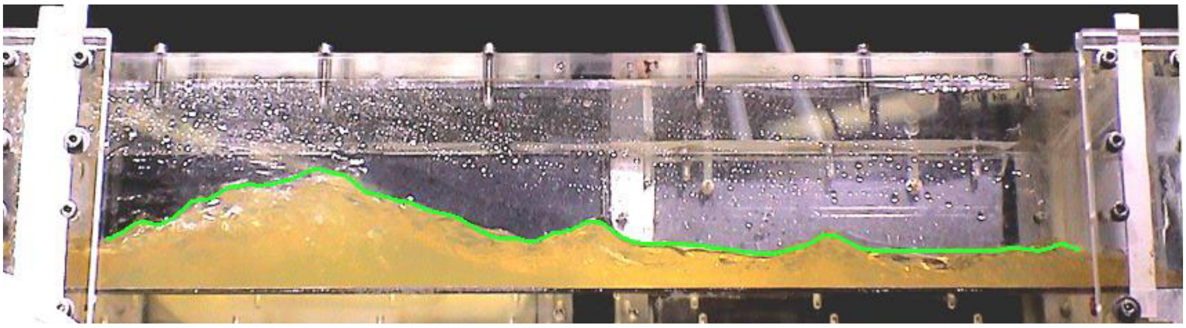

b) Interface merging.

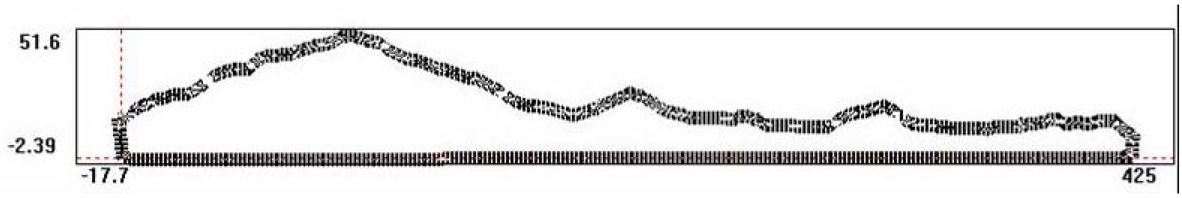

c) Extracted set of points (1000 points).

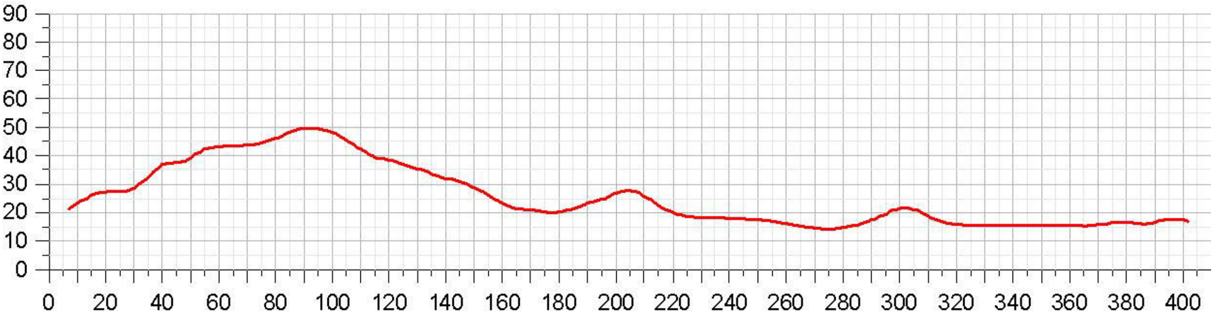

d) Plot of interface after post-processing.

Fig. 4.32. Interface detection process and data obtained for a partially reversed flow (u_{GS}= 10.80 m/s, u_{LS}= 0.12 m/s, y_0= 11 mm)

After interface merging the detected line was divided in a certain number of points, approximately 1000 (see Fig. 4.32c). The interface was plotted and smoothed by mathematical methods (Fig. 4.32d) such as running averages.

This procedure was performed with images recorded consecutively. Once the interface was obtained, features, as for example waves, were identified. Since the time between images was known, wave velocities were investigated.

d) Wave Velocities

Wave velocities obtained for an inlet water depth of 11 mm are presented in this section. Initially the liquid flowed supercritically in the entire test section with an inlet velocity of 1 m/s (Fr_0= 3). The air flow rate was set at a low value and increased progressively. A set of images corresponding to flow conditions at onset of partially reversed flow, fully developed partial reversed flow and totally reversed flow was selected. For each flow regime, three images separated a known period of time were investigated. To analyze wave velocities, the positive direction of the x-axis was changed to obtain positive wave velocities.

Results obtained with three images taken at the onset of partially reversed flow (see Fig. 4.34) are presented in Fig. 4.35. The time interval between images is 110 ms. Three different wave regimes are identified in the channel:

- A wave growing zone: waves are generated at the end of the test section as they get in contact with the air and propagate in the air flow direction. As they progress, their amplitude increases progressively. However, a maximum amplitude exists that can be reached by the waves. This maximum value depends on the relative position of the wave in the x-direction. A wave growing limit can be defined as the envelope line for the maximum wave amplitudes. Also, a lower tangent line can be defined as the position for which the wave amplitude tends to a local minimum (Fig. 4.33).

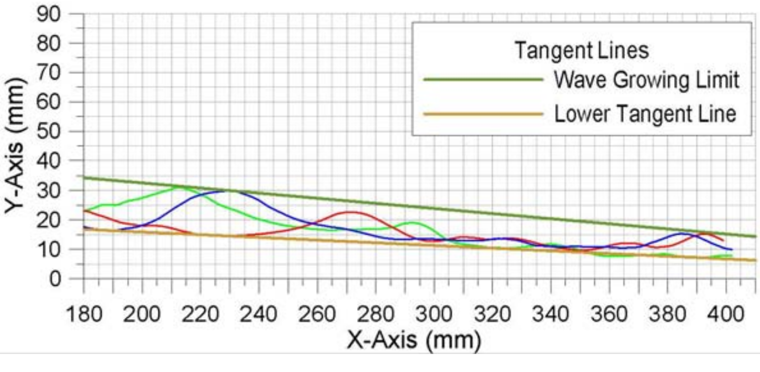

Fig. 4.33. Wave amplitude limits.

- A wave destruction zone: a limiting point for wave growing exists in the test section (see Fig. 4.35, point WDZ1). Beyond this point, waves break due to turbulence caused by the liquid flowing out of the inlet and interacting with the wave fronts. The position of this point is shifted towards the liquid inlet if the gas velocity is increased, so that the wave destruction zone becomes narrower and the growing zone wider.

- A rollover wave zone: part of the injected liquid flows reversely right after the injection point and interferes with the waves present in this zone. The flow path available for the gas is considerably reduced. This effect was already commented in chapter 4.1.1 (see page 72).

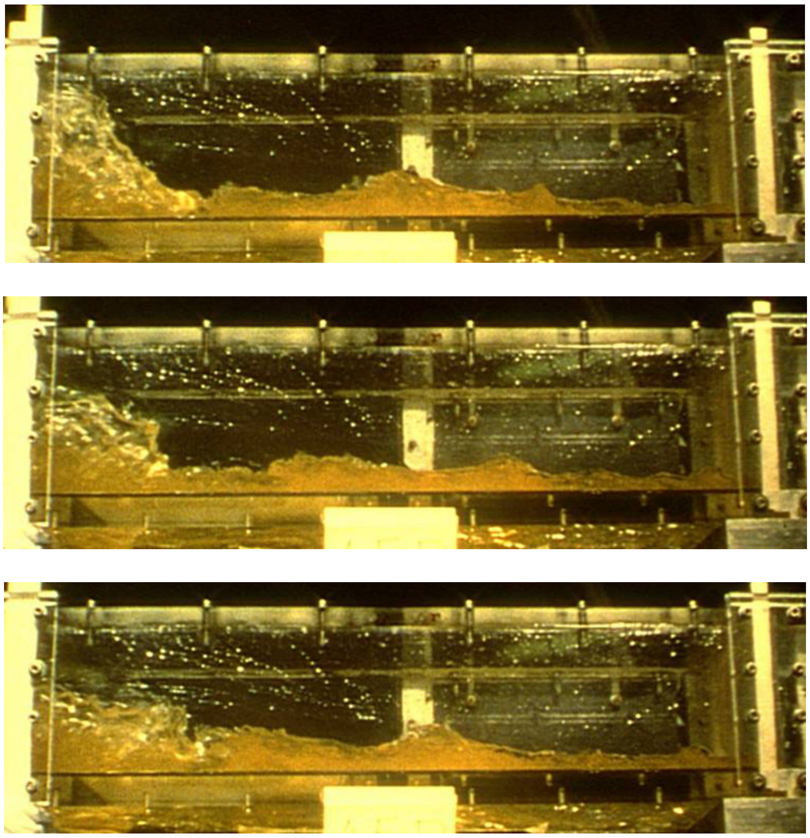

a) t = 0 ms

b) t = 110 ms

c) t = 220 ms

Fig. 4.34. Images selected to calculate wave velocities.

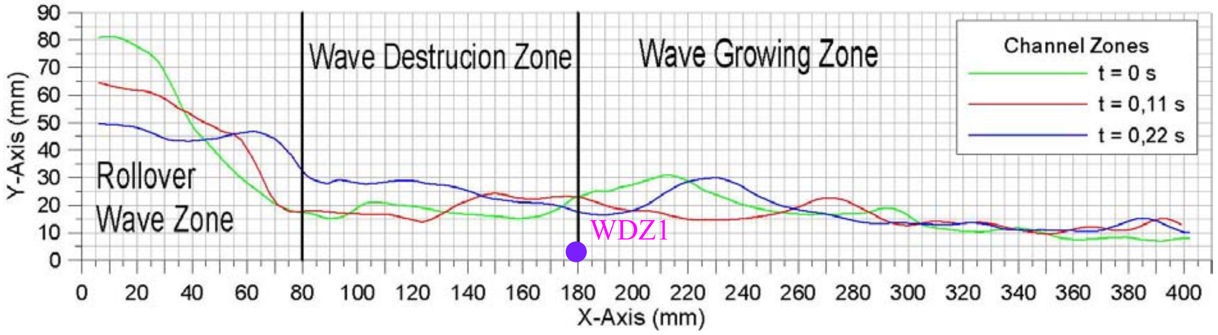

Fig. 4.35. Different wave regimes during onset of partially reversed flow.

It is clear that wave velocities can only be estimated in the wave growing zone. In the example shown in this section, three different wave fronts (**WF**) could be identified (see Fig. 4.36). For example, the wave growth of WF2 can be clearly followed. The distance travelled by the wave between two consecutive images can be extracted and used to calculate the wave velocity.

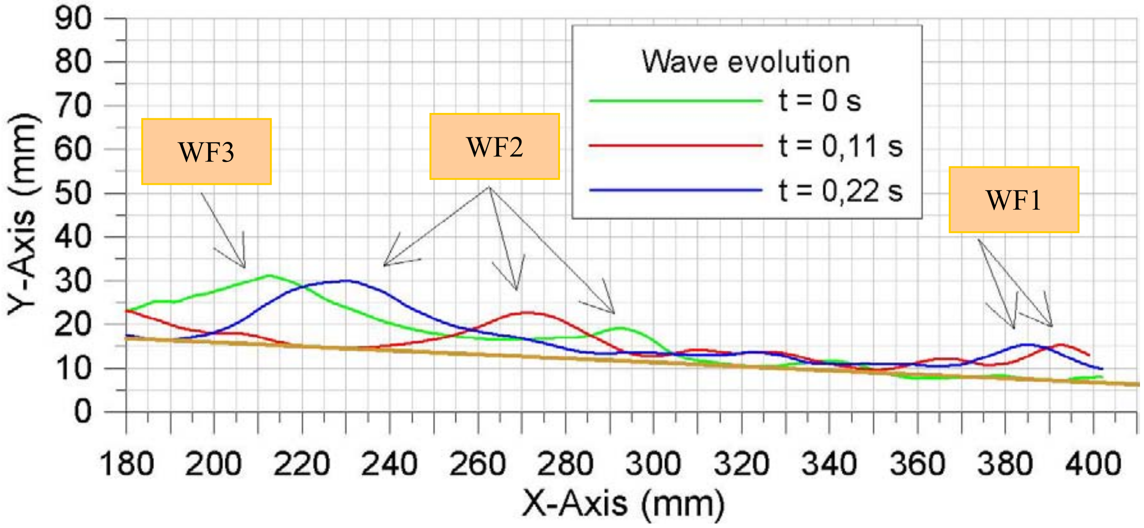

Fig. 4.36. Wave front identification.

Fig. 4.37 shows results obtained using this methodology. Wave velocities obtained for the set of three images presented in Fig. 4.34 are represented with green crosses (OPRF). The wave velocity increases as the position of the wave moves towards the liquid inlet. If the air velocity is increased and partially reversed flow is developed (u_{GS}= X m/s), the wave velocity increases at a given x-position (see points PRF in Fig. 4.37). For higher superficial velocities, totally reversed flow sets in (points represented with OTRF, u_{GS}= x m/s). In this case, a progressive increase in wave velocity can be observed if the position at which the liquid depth tends to zero and the channel dry zone begins is considered as the equivalent zero for the x-coordinate. Then, the “real” position of the wave can be shifted to its equivalent position as shown in Fig. 4.37 for the point TRF.

As a result it can be concluded that the wave velocity increases with increasing air velocity or wave x-position, provided the x coordinate is defined positive in the air flow direction as shown in Fig. 4.37. For the case presented here, wave velocities are in the range of 100 mm/s at the onset of partially reversed flow and increase up to 500 mm/s during totally reversed flow.

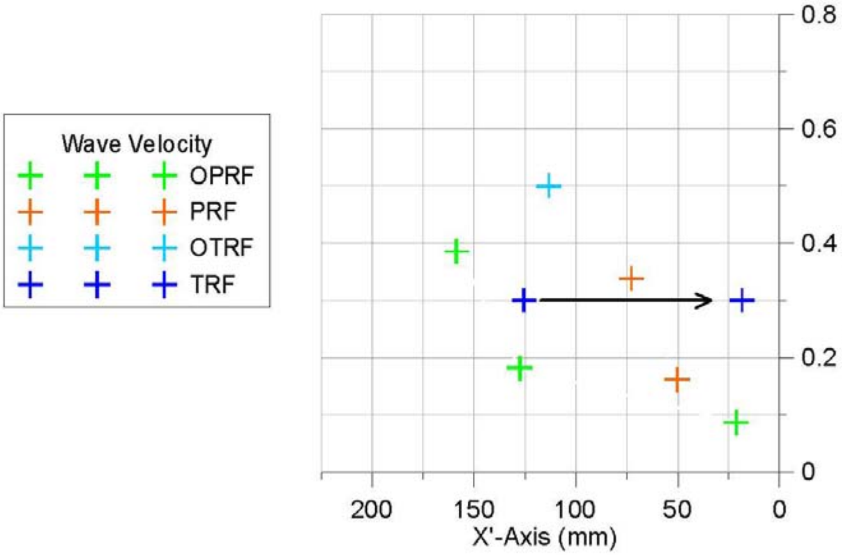

Fig. 4.37. Wave velocities for different flow regimes.

5 Analysis on Prototypic Conditions

5.1 Application to the Reactor Case

The ultimate objective of this work is to provide some criteria to improve ECC in LWRs. Therefore it is necessary to analyze the definitions used up to this point and redefine them for the reactor case, to facilitate the assessment of statements under prototypic conditions.

The conclusions presented in the previous chapter may be applicable to the reactor case, if the particularities associated to it are taken into account. One of the main differences is the circular geometry existing in the prototypic case. Consequently, the problem of defining a Froude number in a circular geometry must be addressed.

Furthermore, the flow regimes in WENKA, which correspond with those in a LWR during ECC, must be identified, so that similarity between these flow regimes exists. As a reference, the conditions of some UPTF experiments, [21], are taken. Similarity between the flow regimes existing in UPTF and WENKA can be expected, if resemblance to a number of dimensionless parameters is borne. The representative parameters are the ratio liquid-inlet-depth-to-channel-height, y_0/H, the ratio channel-length-to-liquid-inlet-depth, ℓ/y_0, the Froude number at the injection point, Fr_0, the gas Reynolds number, Re_G, and the momentum ratio, M. The latter will be defined in chapter 5.3 where these dimensionless parameters are checked out and compared for both facilities.

5.2 Application to Non-rectangular Cross Section: the Froude Number

So far the theory presented as well as the experiments performed have dealt only with rectangular channels. However, there are many applications, where horizontal stratified flow is associated to non-rectangular cross sections, as for example, in the case of circular culverts. Furthermore, as it was pointed out in chapter 1.1.3, hot leg ECC injection in LWRs is performed in a pipeline like geometry (running part-full). Therefore, the problem dealt with in this section is of considerable practical interest.

As a result, the problem of stability of countercurrent stratified flow must be first extended to cover channel sections of any type, and then, to the case of ECC in a LWR with its particularities. Since the Froude number is the key parameter for defining flow regimes and predicting the onset of reversed flow, a general definition of this dimensionless parameter will be presented. A detailed explanation of Froude number calculation for any cross section and useful formulas are to be found in open channel flow literature, as for example in [31].

Consider a channel section with an arbitrary form as shown in Fig. 5.1. Q is the total discharge or volumetric flow rate, A is the whole area of the cross section and B is the surface width of the waterway.

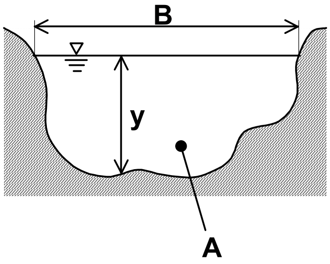

Fig. 5.1. Channel with an arbitrary cross section.

The depth y changes locally but an *equivalent depth*, y_{eq} can be calculated as

$$y_{eq} = \frac{A}{B} \tag{5.1}$$

The Froude number is defined as:

$$Fr = \frac{u}{u_C} = \frac{u}{\sqrt{g A/B}} = \frac{u}{\sqrt{g y_{eq}}} \tag{5.2}$$

Using this generalized definition, the conclusions obtained in chapter 1 about the occurrence of critical flow are equally true for all shapes of channel cross section. The flow is critical if the Froude number is equal to unity and the equivalent depth y_{eq} is equal to the critical height.

According to the above discussion, the first step to determine the Froude number in any geometry is to calculate the whole area of the cross section A and the surface width of the waterway B**.** However, if the UPTF geometry is analyzed (the arrangement of the ECC hot leg injection used in the UPTF experiments was already presented in chapter 1.1.3), there may be some problems by the definition of the terms B and A.

For comparison with the flow regimes in the WENKA test facility, the Froude number at the end of the secondary pipe of the UPTF test facility, $Fr_{A\text{-}A}$**,** (section A-A, seeFig. 1.13, page 28) must be estimated. This Froude number defines the flow regime of the coolant at the end of the injection pipe, that is to say, the entry conditions of liquid during hot leg ECC.

To facilitate the analysis of the Froude number for the UPTF geometry, a simplified method has been devised. Fig. 5.2 (left-side) shows the flow cross section at the end of the injection pipe in the UPTF facility and an equivalent geometry to simplify the calculation of the Froude number (right-side). Actually, the cross section of the flow takes approximately this form right after having left the injection pipe. Both flow cross sections have the same liquid area A_L. This liquid flow area is used to determine the wetted perimeter b, the liquid depth y_L and the liquid width B in the simplified case.

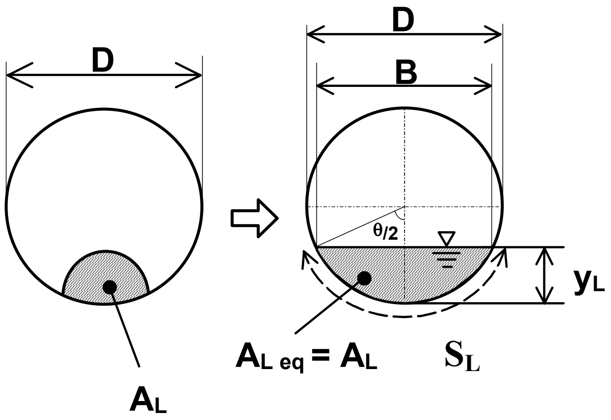

Fig. 5.2. Geometrical similarity for Froude number calculation using UPTF-geometry.

It is easy to probe that

$$y_L = \frac{D}{2}\left(1-\cos(\theta/2)\right) \tag{5.3}$$

$$A_L = \frac{S_L D}{4} - \frac{B\left(D-2y_L\right)}{4} \tag{5.4}$$

where D is the pipe diameter of the main line, $\theta/2$ is the contact angle of the wetted perimeter S_L and

$$S_L = \theta\frac{D}{2} \tag{5.5}$$

$$B = D\sin(\theta/2) \tag{5.6}$$

Note, that y_L is not the equivalent height, but it is needed to determine A_L. The equivalent water depth y_{eq} can be calculated as

$$y_{eq} = \frac{A_L}{B} = \frac{S_L D}{4D\sin(\theta/2)} - \frac{\left(D-2y_L\right)}{4} = \frac{D}{4}\left(\frac{1}{2}\frac{\theta}{\sin(\theta/2)} + \frac{2y_L}{D} - 1\right) \tag{5.7}$$

And the Froude number is given by

$$Fr = \frac{u}{u_C} = \frac{u}{\sqrt{g y_{eq}}} \tag{5.8}$$

Table 1 shows experimental values of the UPTF injection test 26, run 230 [31] and the calculated Froude numbers at the end of the injection pipeline. All parameters are referred to the injection point (subscript 0). The liquid depth yielding critical conditions, $y_{L,C}$ and the corresponding liquid area $A_{L,C}$ are also given.

$\dot{m}_L$(kg/s)	D(m)	A_{L0}(m²)	B(m)	y_{L0} (m)	y_{eq}(m)	u_{L0}(m/s)	Fr_0	$y_{L,C}$(m)	$A_{L,C}$(m^2)
150	0.75	0.0365	0.516	0.103	0.071	4.43	5.32	0.241	0.122
400	0.75	0.0365	0.516	0.103	0.071	11.82	14.18	0.401	0.240

Table 1. Froude numbers for UPTF test 26.

Two different mass flow rates, $\dot{m}_L$, were investigated: 150 and 400 Kg/s. The Froude numbers at the end of the injection pipe (calculated with an equivalent water depth of 71 mm) show that the flow is injected in both cases supercritically. The flow is critical up to a value of water depth y_L of 241 mm (150 Kg/s) and 401 mm (400 Kg/s), that is to say, critical flow would occur, if the flow cross section increased somewhere in the primary line up to 0.122 and 0.240 m² respectively.

5.3 Comparison with WENKA Flow Regimes: Similarity Check

The similarity between liquid flow regimes in the WENKA test facility and the UPTF test facility is applicable if the Froude numbers at the injection points (Fr_0), the Reynolds numbers of the gas entering the flow section (Re_{GS}), the slip velocity ratio, s, and the ratio channel-length-to-liquid-inlet-depth, ℓ/y_0, are equal. This yields similar conditions for critical flow occurrence, what actually determines the conditions for which onset of reversed flow occurs.

Once reversed flow has been established, additional parameters play a predominant role in determining the liquid delivery rates, the grade of blockade of the gas flow cross section or hysteresis effects. These parameters are the ratio channel-height-to-liquid-inlet-depth (y_0/H in WENKA and y_{L0}/D in UPTF), that yields similar conditions for slug flow onset, and the momentum ratio M, that is defined in WENKA as

$$M = \frac{\rho_G u_{GS}^2 H}{\rho_L u_{L0}^2 y_0} \tag{5.9}$$

This parameter is necessary to formulate meaningful assessments for the UPTF case based on the conclusions valid for WENKA, since it is a measure of the inertia balance between both fluids. The corresponding definition for UPTF (pipe flow) is

$$M = \frac{\rho_G u_{GS}^2 D}{\rho_L u_{L0}^2 y_{L0}} \tag{5.10}$$

First of all, the similarity of the liquid flow regimes will be analyzed. In Table 15 the experimental conditions of the WENKA tests are presented together with the correspondent liquid Froude numbers at the inlet and the ratios ℓ/y_0. Conditions with Froude numbers in the range defined by those calculated for the UPTF experiments are pointed out in bold. A graphical representation is given in Fig. 5.3.

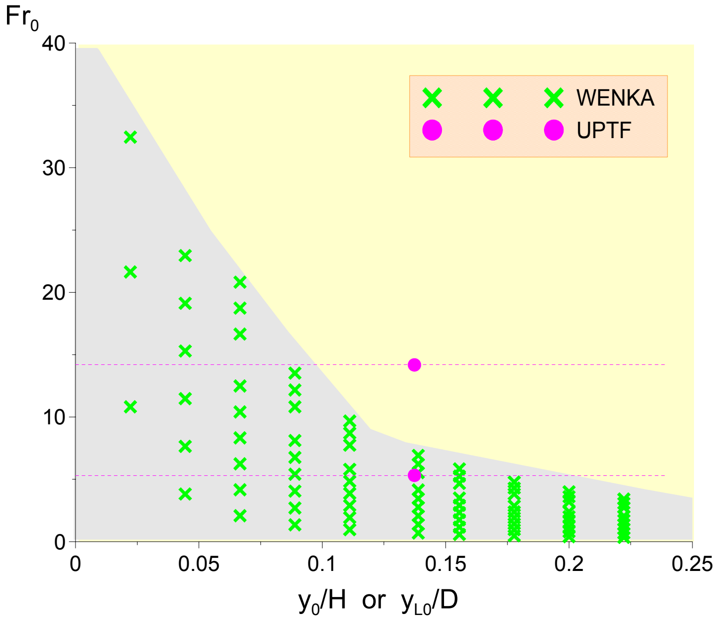

Fig. 5.3. Possible liquid Froude numbers at injection point in WENKA compared to those present in hot leg ECC injection (Data from UPTF).

It can be concluded that with inlet liquid depths between 2 and 20 mm the Froude numbers existing in UPTF are well represented in WENKA. An inlet water depth of 12.5 mm yields good similarity regarding the inlet Froude number. For this liquid height, the ratio y_0/H is equal to 0.139, approximately the same as in UPTF (y_{L0}/D = 0.137), leading to similarity about onset of slug flow. Nevertheless, the maximum Froude number that can be achieved in WENKA with this liquid height is around 7, much less than the maximum value in the prototypic case (In UPTF the injection Froude number ranges from 5.3 to 14.2) and estimations outside the flow conditions investigated in WENKA are merely extrapolations and should be assisted by additional tests or numerical calculations.

Concerning the liquid Reynolds numbers, it will be assumed that the liquid Reynolds number similarity is fulfilled. The WENKA tests were performed for highly turbulent flow, with liquid Reynolds numbers up to 6.6E+4 (see Table 14). Reynolds numbers of the UPTF experiments are presented in Table 2. Note that even though the liquid Reynolds numbers in UPTF are higher, we expect that the difference is not relevant for values of this order of magnitude.

$\dot{m}_L$ (kg/s)	$\dot{V}_G$ (m^3/s)	A_{L0}(m²)	u_{L0}(m/s)	Dh_{L0}(m)	Re_{L0}
150	0.162	0.0365	4.43	0.19	4.06E+06
400	0.432	0.0365	11.82	0.19	1.08E+07

Table 2. Liquid Reynolds numbers in UPTF.

The similarity for the gas flow Reynolds numbers is checked in Table 3 and Table 4. The gas Reynolds numbers were calculated using the superficial gas velocity. Since the Reynolds numbers differ only in one order of magnitude, and the high turbulent regime can be guaranteed, the similarity will be again assumed as fulfilled.

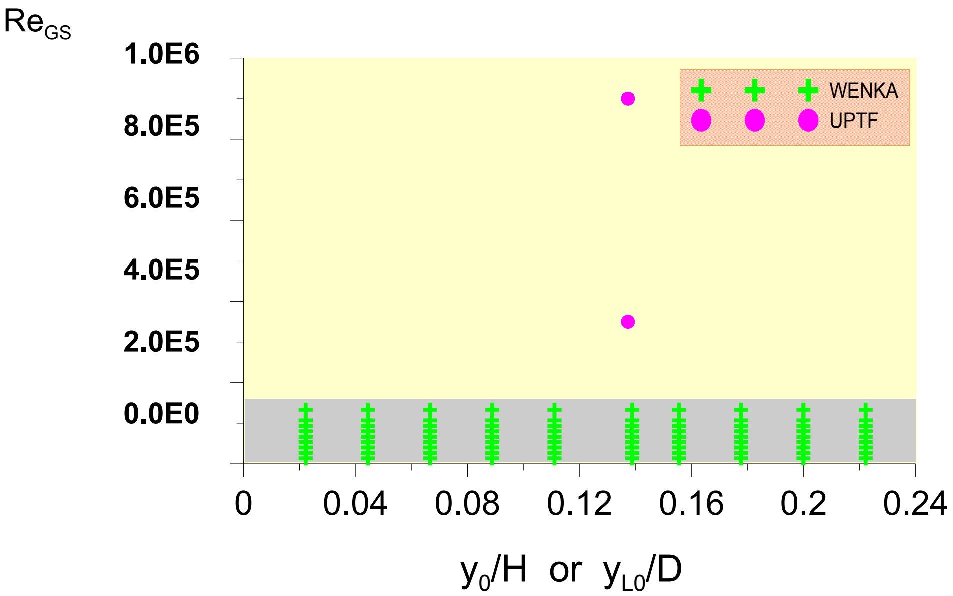

Fig. 5.4. Gas Reynolds numbers in WENKA and in UPTF.

$\dot{m}_G$(kg/s)	$\dot{V}_L$(m³/s)	A_{G0}(m²)	u_{G0}(m/s)	Re_{G0}
8	3.7	0.442	8.4	9.9E+05
32	14.9	0.442	33.7	3.9E+06

Table 3. Gas Reynolds number in UPTF.

Q_G(l/s)	$\dot{V}_G$(m³/s)	A_{G0} (m²)	u_{G0}(m/s)	D_{hG0}(m)	Re_{G0}
50	0.05	0.0099	5.1	0.099	7.8E+04
60	0.06	0.0099	6.1	0.099	9.4E+04
80	0.08	0.0099	8.1	0.099	1.3E+05
100	0.10	0.0099	10.1	0.099	1.6E+05
120	0.12	0.0099	12.1	0.099	1.9E+05
140	0.14	0.0099	14.1	0.099	2.2E+05
160	0.16	0.0099	16.2	0.099	2.5E+05
180	0.18	0.0099	18.2	0.099	2.8E+05
200	0.20	0.0099	20.2	0.099	3.1E+05

Table 4. Gas Reynolds number range investigated in WENKA.

Similarity for the momentum ratio M can now be checked considering that the ratio y_L/D is equal to y_0/H (what applies in WENKA if y_0=12.5 mm). Then, the momentum ratio similarity can be reduced to similarity for the ratio

$$\frac{\rho_G u_{GS}^2}{\rho_L u_{L0}^2} \tag{5.11}$$

(see equations (5.9) and (5.10)). It should be noted, that the density ratio of the fluids employed in WENKA differs from that of the fluids present in the reactor case or used in the UPTF test series. As it was already mentioned in chapter 0, in the WENKA test facility water and air are used, whereas in the UPTF test facility water and steam were used as test fluids since they are prototypic. In addition, the temperatures in UPTF were much higher than in WENKA, where the fluids were used at ambient temperature. This yields to a difference in the density ratio of the fluids. In Table 5 a comparison of these density ratios is presented, taking as a reference for prototypic conditions the pressure and temperatures given in [40].

UPTF			**WENKA**		
ρ_G(Kg/m^3) *(P=0.4 MPa T=146°C)*	**ρ_L(Kg/m^3)** *(P=0.4 MPa T=140°C)*	ρ_G/ρ_L	**ρ_G(Kg/m^3)** *(P=0.1 MPa T=20°C)*	**ρ_L(Kg/m^3)** *(P=0.1 MPa T=20°C)*	ρ_G/ρ_L
2.148	926.097	2.32E-03	1.189	998.21	1.19E-03

Table 5. Comparison of density ratios.

The density ratio of the prototypic fluids is almost twice that of the fluids employed in the WENKA experiments. Consequently, similarity for the M parameter means actually

$$\left(\frac{u_{GS}}{u_{L0}}\right)^2_{UPTF} = \frac{1}{2}\left(\frac{u_{GS}}{u_{L0}}\right)^2_{WENKA} \Rightarrow \sqrt{2}\left(\frac{u_{GS}}{u_{L0}}\right)_{UPTF} = \left(\frac{u_{GS}}{u_{L0}}\right)_{WENKA} \tag{5.12}$$

That is to say, the momentum ratio is equivalent in both facilities when the squared gas-to-liquid-velocity ratio in UPTF doubles that investigated in WENKA, or in another words, when the ratio of gas and liquid velocity in WENKA is $\sqrt{2}$ times that of UPTF.

Considering a water depth of 12.5 mm, the ratio y_0/H in WENKA is equivalent to y_{L0}/D in UPTF, so that the momentum ratio equivalence applies if equation (5.12) is satisfied. Table 16 shows the values of $\sqrt{2}\left(u_{GS}/u_{L0}\right)$ for the UPTF experiments. Given these values, there is momentum similarity between WENKA and UPTF if the ratio $\left(u_{GS}/u_{L0}\right)$ in WENKA ranges from 1 to 11 approximately. This is fulfilled for several pairs of gas and liquid velocities for an initial water depth of 12.5 mm (Table 17, arrays in bold).

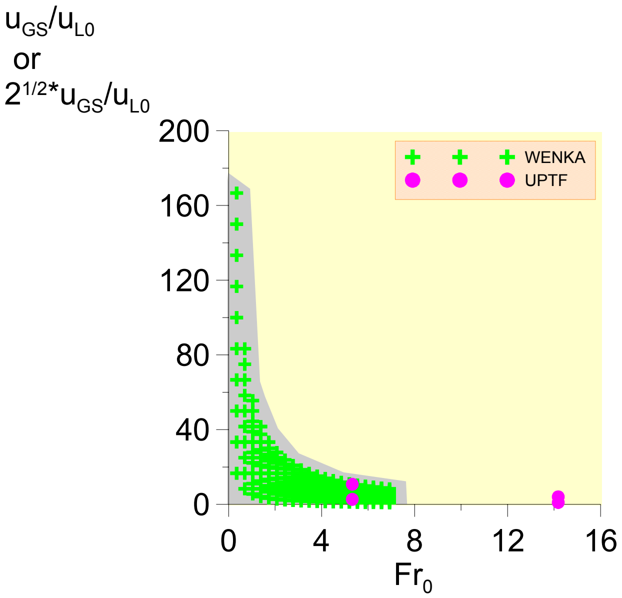

Fig. 5.5. Comparison of velocity ratios versus inlet Froude number.

Fig. 5.5 presents a comparison of velocity ratios over the inlet Froude number. For Froude numbers up to 7 is the similarity fulfilled. Momentum ratio similarity can be assumed.

Finally, the ratio ℓ/y_0 must be checked. Table 6 gives the values of this ratio for the WENKA test facility. The value employed in UPTF was 14.85. This value can be represented in WENKA if an inlet water depth of 32 mm is set. However, the 1-dimensional model presented in chapter 1 can predict satisfactorily values of ℓ/y_0 up to 30, and since it is an analytical model, can predict also the transition to subcritical flow for the UPTF conditions.

y_0/H	y_0 (mm)	ℓ/y_0
0.022	2	235.0
0.044	4	117.5
0.067	6	78.3
0.089	8	58.8
0.111	10	47.0
0.139	12.5	37.6
0.156	14	33.6
0.178	16	29.4
0.200	18	26.1
0.222	20	23.5

Table 6. Values of ℓ/y_0 in WENKA.

It can be concluded that similarity is confirmed between the conditions investigated in the WENKA test facility and those present in a hot leg ECC scenario: same Froude numbers, liquid and gas Reynolds numbers and momentum ratios were investigated and in this way, the fluid dynamics of hot leg injection can be better understood.

6 Conclusions and Outlook

Horizontal countercurrent stratified flow was investigated with application to ECC hot leg injection in PWRs.

The stability of countercurrent flow in the hot leg during LOCA scenarios was studied extensively over the last years for reflux condensation mode. However, the problem of ECC injection by means of a secondary pipe in the hot leg was little investigated. Hereby, the coolant is injected at large Froude numbers counter a steam flowing out of the RPV with large Reynolds numbers. Countercurrent flow limitations have not been studied sufficiently up to now in order to predict properly coolant delivery rates. Additionally, there is a lack of experimental data to support the analysis of such an accident scenario with CFD - codes.

The WENKA program was launched to investigate flow regimes in horizontal countercurrent stratified flow in a simplified PWR hot leg geometry. Using air and water, the fluid dynamics of the injection process was reproduced in a rectangular channel to derive 1-dimensional models to predict the limits of coolant delivery. On the other hand, a data base of local flow parameters was established to enhance CFD-Codes performance. Experimental local velocities of the liquid film were obtained by means of Particle Image Velocimetry and the liquid film morphology was analyzed depending on the flow regimes.

Flow regime maps were obtained for inlet liquid depths ranging from 3 to 15 mm. Depending on the superficial velocities of liquid and gas, stratified countercurrent flow, partially reversed flow or totally reversed flow was experimentally observed.

Stratified countercurrent flow can be in form of a supercritical flow if the Froude number of the liquid film is larger than unity throughout the test section. A supercritical flow is an inertia dominated flow. For Froude numbers less than unity the liquid film is subcritical and wave propagation upstream the injection point is possible. A subcritical flow is a gravity dominated flow. The transition from supercritical flow to subcritical flow is in form of a hydraulic jump that occurs at the end of the test section and progresses up to a stable position in the channel. This transition was modelled by means of 1-dimensional momentum equations of the liquid film. An analytical model was obtained to predict the occurrence of a hydraulic jump in a channel with countercurrent gas flow. Comparison with experimental data obtained for a wide range of conditions yielded satisfactory agreement with model predictions.

At high superficial velocities, the stability of stratified flow is broken and a transition to partially reversed flow occurs. A fraction of the injected liquid flows backwards carried over by the gas flow and this yields to reduced liquid delivery. A back flow ratio is defined as the ratio of mass flow rate flowing backwards and the initially injected mass flow rate. For a value of the back flow ratio equal to unity, the entire liquid flows in the gas flow direction. This situation is referred to as totally reversed flow. An empirical correlation obtained from experimental data is proposed to predict water delivery rates depending on the flow conditions. The Froude number of the liquid at the injection point and the Reynolds number of the gas calculated with the superficial gas velocity are the parameters that determine the fraction of liquid delivered.

With an initial supercritical flow, the transition to partially reversed flow coincides with the transition to subcritical flow in form of a hydraulic jump that progresses beyond the liquid injection point setting reversed flow. It can be concluded, that the transition to subcritical flow is a necessary condition for reversed flow in a channel. However, an additional criterion exists, since a hydraulic jump was observed in the test facility without reversed flow. Additional experiments were performed focusing on this problem. The Wallis correlation to predict onset of reversed flow was checked. This is a well-established correlation regarding investigations on reversed flow with application to light water reactors safety. Nevertheless, this correlation overpredicts the occurrence of reversed flow in the WENKA test facility because Wallis did not consider the inertia of the fluids in his model. As a result, the Wallis correlation is only applicable to subcritical flows, where gravitational forces are dominant. Comparison with experimental data showed, that the modification of the Wallis correlation proposed by Richter yields good agreement if both the necessary condition of subcritical flow and the condition given by the Richter correlation are fulfilled. The constraint equation for the transition from supercritical to subcritical flow obtained in the first part of this work was combined with the constraint equation of Richter to predict reversed flow. A novel criterion to predict the onset of reversed flow that merged both concepts was presented. The new criterion predicts successfully the occurrence of reversed flow in the WENKA test facility.

Literature

[1] Andreussi, P., Sandroni, G., Minervini, A., Battarra, V., Mariani, O. and Nicolai, H., *Countercurrent Gas-Liquid Flow in Inclined Pipes*, Proceedings 3rd Int. Conf. Multi-Phase Flow, 13 – 20 May, The Hague, Netherlands, BHRA, The Fluid Engineering Centre, Cranfield, 1987.

[2] Anglada, J. M., *Local Measurements of Stratified Flow in Channels Concerning LWR's Safety*, Diploma Thesis, ETSEIB, Mechanical Engineering University, Barcelona, Spain, 2003.

[3] Ardron, K. H. and Banerjee S., *Flooding in an Elbow Between a Vertical and a Horizontal or Near-Horizontal Pipe. Part II: Theory*, Int. J. Multiphase Flow, Vol. 12, No. 4, 1986, 543-558.

[4] Argyropoulos, P. A., *The Hydraulic Jump and the Effect of Turbulence on Hydraulic Structures: Contribution of the Research of the Phenomena*, Proc. 9th Conference Int. Ass. for Hydraulic Research, 1961, 173-183.

[5] Asla, R., *Liquid Film Morphology Analysis Applied to the Hot Leg Injection in Pressurized Water Reactor's Emergency Core Cooling System*, Diploma Thesis, ETSEIB, Mechanical Engineering University, Barcelona, Spain, 2003.

[6] Badie, S., Lawrence, C. J. and Hewitt, G. F., *Axial Viewing Studies of Horizontal Gas-Liquid Flows with Low Liquid Loadings,* Int. J. Multiphase Flow, Vol. 27, 2001, 1259-1269.

[7] Baker, A. and Gravestock, N., *New Correlations for Predicting Pressure Loss and Holdup in Gas / Condensate Pipelines*, Proceedings 3rd Int. Conf. Multi-Phase Flow, 13 – 20 May, The Hague, Netherlands, BHRA, The Fluid Engineering Centre, Cranfield, 1987.

[8] Baker, O., *Simultaneous Flow of Oil and Gas*, Oil and Gas J., Vol. 53, 1959, 85-195.

[9] Bankoff, S. G. and Lee, S. C., *A Critical Review of the Flooding Literature*, NUREG/CR-3060R2, 1983.

[10] Bankoff, S. G. and Kim, H. J., *Local Condensation Rates in Nearly Horizontal Stratified Countercurrent Flow of Steam and Cold Water,* AIChE Symposium Series, Vol. 79, 1983, 209-223.

[11] Barnea, D., Yosheph, N. B. and Taitel, Y., *Flooding in Inclined Pipes: Effect of Entrance section*, Can. J. Chem. Eng., Vol. 64, 1986, 177.

[12] *VDI-Wärmeatlas, Berechnungsblätter für den Wärmeübergang*, VDI-Gesellschaft Verfahrenstechnik und Chemieingenieurwesen(GVC), 9. Aufl., 2002, XIII.

[13] Chanson, H. and Brattberg, T., *Experimental Study of the Air-Water Shear Flow in a Hydraulic Jump*, Int. J. Multiphase Flow, Vol. 26, 2000, 583-607.

[14] Choi, K. Y. and No, H. C., *Experimental Studies of Flooding in Nearly Horizontal Pipes*, Int. J. Multiphase Flow, Vol. 21, No. 3, 1995, 419-436.

[15] Chow, V. T., *Open Channel Hydraulics*, McGraw-Hill Book Company, New York, 1959.

[16] Chun, M. and Yu, S., *Effect of Steam Condensation on Countercurrent Flow Limiting in Nearly Horizontal Two-Phase Flow*, Nucl. Eng. Design, Vol. 196, 2000, 201-217.

[17] Chung, S. K., Liu, L. P. and Tien, L., *Flooding in Two-Phase Countercurrent Flows II, Experimental Investigation*, Physicochemical Hydrodynamics, Vol. 1, 1980, 209-220.

[18] Clift, R., Pritchard, C. L. and Nedderman, R. M., *The effect of Viscosity on the Flooding Conditions in Wetted Wall Columns*, Chem. Eng. Sci., Vol. 21, 1966, 87-95.

[19] Collyer, M. R., *The Stability of Stratified Shear Flows*, J. Fluid Mech., Vol. 42, 1970, 367-378.

[20] Daly, B. J. and Harlow, F. H., *A Model of Counter-current Steam-Water Flow in Large Horizontal Pipes*, Nuclear Science and Engineering, Vol. 77, 1981, 273-284.

[21] Damerell, P. S. and Simons, J. W., *Reactor Safety Issues Resolved by the 2D / 3D Program*, Prepared Jointly by Japan Atomic Energy Research Institute, Gesellschaft für Anlagen- und Reaktorsicherheit (GRS) mbH, Siemens AG, UB KWU, U. S. Nuclear Regulatory Commission, Los Alamos National Laboratory, MPR Associates, Inc., 1993.

[22] Dillistone, M. J., *Analysis of the UPTF Separate Effects Test 11 (Steam - Water Countercurrent Flow in the Broken Loop Hot Leg) using RELAP5 / MOD2,* Winfrith Technology Center, NUREG/IA-0071, 1992.

[23] Dukler, A. E. and Smith, L., *Two-Phase Interactions in Counter Current Flow: Studies of the Flooding Mechanism*, NUREG/CR-0617, 1979.

[24] Elsäßer, A., Samenfink, W., Ebner, J., Dullenkopf, K. and Wittig, S., *Dynamics of Shear-Driven Liquid Films,* Proceedings of the 7th International Conference on Laser Anemometry- Advances and Applications, Karlsruhe, Germany, September 8-11, 1997.

[25] Fabre, J., Masbernat, L. and Suzanne, C., *Stratified Flow, Part II: Interfacial and Wall Shear Stress, Proc. 2nd Int. Workshop on Two-Phase Flow Fundamentals, Experimental Data Sets for Evaluation of Modeling Methods*, Rensselaer Polytechnic Institute, Troy, NY, 1987.

[26] French, R. H., *Open-Channel Hydraulics*, McGraw-Hill Company, New York, 1985.

[27] Wallis, G. B. and Dobson, J. E., *The Onset of Slugging in Horizontal Stratified Air - Water Flow*, Int. J. Multiphase Flow, Vol. 1, 1973, 173-193.

[28] Gardner, G. C., *Flooded Countercurrent Two-Phase Flow in Horizontal Tubes and Channels*, Int. J. Multiphase Flow, Vol. 9, No. 4, 1983, 367-382.

[29] Glaeser, H., *Downcomer and Upper Tie Plate Countercurrent Flow in the Upper Plenum Test Facility*, Gesellschaft für Reaktorsicherheit, GRS-A-1726, November 1990.

[30] Grolmes, M. A., Lambert, G. A. and Fauske, H. K., *Flooding in Vertical Tubes*, AIChE Symposium on Multiphase Flow Systems, Glasgow, Scotland, 1974.

[31] Henderson, F. M., *Open Channel Flow*, The McMillan Company, New York, 1966.

[32] Hewitt, G. F. and Hall-Taylor, S., *Annular Two-Phase Flow*, Pergamon Press, Oxford, 1970.

[33] Hewitt, G. F., *Influence of End Conditions, Tube Inclination and Physical Properties on Flooding in Gas-Liquid Flows*, Harwell Report, HTFS-RS222, 1977.

[34] Hewitt, G. F. and Wallis, G. B., *Flooding and Associated Phenomena in Falling Film Flow in a Vertical Tube*, AERE-R4022, 1963.

[35] IAEA Safety Series No. 50-C-D (Rev.1), *Code on the Safety of Nuclear Power Plants: Design*, IAEA, Vienna, 1988.

[36] Jayanti, S., Tokarz, A and Hewitt, G. F., *Theoretical Investigation of Diameter Effect on Flooding in Countercurrent Flow*, Int. J. Multiphase Flow, Vol. 22, No. 2, 1996, 307-324.

[37] Kim, H. J., Lee, S. C. and Bankoff, S. G., *Heat Transfer and Interfacial Drag in Countercurrent Steam-Water Stratified Flow*, Int. J. Multiphase Flow, Vol. 11, 1985, 593-606.

[38] Kim, H. J., *Local Properties of Countercurrent Stratified Steam-Water Flow*, Ph. D. thesis, Northwestern University, Evanston, IL, 1983, 27-58.

[39] King, H. W. and Brater, E. F., *Handbook of Hydraulics*, 5th Ed. McGraw-Hill Book Company, New York, 1963.

[40] Kolev, N. I., Seitz, H. and Roloffbock, I., *Hot Leg Injection: 3D versus 1D Three Velocity Fields Modeling and Comparison with UPTF Experiment,* ExHFT-5, 5th World Conference on Experimental Heat Transfer, Fluid Mechanics and Thermodynamics, Thessaloniki, Greece, Sept. 24-28, 2001.

[41] Kordyban, E., *Horizontal Slug Flow: A Comparison of Existing Theories*, ASME J. Fluids Eng., Vol. 112, 1990, 74-83.

[42] Krolewski, S. M., *Flooding Limits in a Simulated Nuclear Reactor Hot Leg*, Massachusetts Institute of Technology, Submission as a part of requirement for a B. Sc., 1980.

[43] Lamb, H., *Hydrodynamics*, 6th Ed., Dover, New York, 1945.

[44] Lee, S. C. and Bankoff, S. G., *Stability of Steam - Water Countercurrent Flow in an Inclined Channel: Flooding*, J. Heat Transfer, Vol. 105, 1983, 713-718.

[45] Lee, S. C., *Interfacial Friction Factors in Countercurrent Stratified Two-Phase Flow*, Chem. Eng. Commun., Vol. 118, 1992, 3-16.

[46] Libmann, J., *Elements of Nuclear Safety*, Les Editions de Physique, Les Ulis cedex A, France, 1996.

[47] Lillington, J. N., *Light Water Reactor Safety, the Development of Advanced Models and Codes for Light Water Reactor Safety Analysis*, Elsevier, The Netherlands, 1995.

[48] Lopez de Bertodano, M., *Countercurrent Gas-Liquid Flow in a Pressurized Water Reactor Hot Leg*, Nuclear Sci. and Eng., Vol.117, 1994, 126-133.

[49] McQuillan, K. W. and Whalley, P.B., *A Comparison between Flooding Correlations and Experimental Flooding Data for Gas - Liquid Flow in Vertical Tubes*, Chem. Eng. Sci. Vol. 40, 1985, 1425-1441.

[50] Meyer, L. and Gargallo, M., *Low-Pressure Corium Dispersion Experiments with Simulant Fluids in a Scaled Annular Cavity*, Nuclear Technology, Vol. 141, Mar. 2003, 257-274.

[51] Ohnuki, A., Adachi, H. and Murao, Y., *Scale Effects on Countercurrent Gas-Liquid Flow in a Horizontal Tube connected to an Inclined Riser*, Nuclear Eng. And Design, Vol. 107, 1988, 283-294.

[52] Ohnuki, A., *Experimental Study of Counter-Current Two-Phase Flow in Horizontal Tube Connected to an Inclined Riser*, J. Nucl. Sci. and Techn., Vol. 23, No. 3, 1986, 219-232.

[53] Pushkina, O. L. and Sorokin, L., *Breakdown of Liquid Film Motion in Vertical Tubes*, Heat Transfer Soviet Research, Vol. 1, 1969, 56-64.

[54] Rahman, M. M., Faghri, A. and Hankey, W. L., *Computation of Turbulent Flow in a Thin Liquid Layer of Fluid Involving a Hydraulic Jump*, J. Fluids Eng., Vol. 113, 1991, 411-418.

[55] Ralph, J. C., Costigan, G. and Gardner, G. C., *Low and High Head Flooding for Countercurrent Flow in Short Horizontal Tubes*, Int. J. Multiphase Flow, Vol. 13, No. 1, 1987, 47-55.

[56] Rao, C. R., *Handbook of Statistics*, Elsevier, Amsterdam, 2003.

[57] Report ASCE, *Task Force on Friction Factors in Open Channels*, Proc. Am. Soc. Civil Engrs. Vol. 89, No. HY2, March 1963.

[58] Richter, H. J., Wallis, G. B., Carter, K. H. and Murphy, S. L., *Deentrainment and Countercurrent Air - Water Flow in a Model PWR Hot Leg*, Nuclear Regulatory Commission Report, NRC-0193-9, 1978.

[59] Siddiqui, H., Banerjee, S. and Ardron, K. H., *Flooding in an Elbow Between a Vertical and a Horizontal or Near - horizontal Pipe. Part I: Experiments*, Int. J. Multiphase Flow, Vol. 12, No. 4, 1986, 531-541.

[60] Silvester, R., *Hydraulic Jump in All Shapes of Horizontal Channels*, Proc. American Society of Civil Eng., Journal of the Hydraulics Division, Vol. 90, HY1, January 1964, 23-55.

[61] Stevanovic, V. and Studovic, M., *A Simple Model for Vertical Annular and Horizontal Stratified Two-Phase Flows with Liquid Entrainment and Phase Transitions: One Dimensional Steady State Conditions*, Nuclear Engineering and Design, Vol. 154, 1995, 357-379.

[62] *Summary of Results from the UPTF Carryover/steam Binding Separate Effects Tests, Comparison to Previous Scaled Tests and Application to U. S. Pressurized Water Reactors*, prepared by MPR Associates, MPR-1213, October 1990.

[63] Taitel, Y., Barnea, D. and Dukler, A. E., *A Film Model for Prediction of Flooding and Flow Reversal for Gas-Liquid Flow in Vertical Tubes*, Int. J. Multiphase Flow, Vol. 8, 1982, 1-22.

[64] Taitel, Y. and Dukler, A. E., *A Model for Predicting Flow Regime Transitions in Horizontal and Near Horizontal Gas-Liquid Flow,* AIChE J., Vol. 22, 1976, 47-55.

[65] Takeuchi, K., Young, M. Y. and Gagnon, A. F., *Flooding in the Pressurizer Surge Line of AP600 Plant and Analyses of APEX Data*, Nuclear Eng. and Design, Vol. 192, 1999, 45-58.

[66] *The Accident at Three Mile Island*, Staff Reports to the President's Commission, Selected reports from the Technical Assessment Task Force, the Public Health and Safety Task Force, the Office of the Chief Counsel. Reprint. from the U.S. Government Publications, Oxford - Pergamon, Progress in Nuclear Energy; New Ser. Vol. 6, 1980.

[67] Wallis, G. B., *Flooding Velocities for Air and Water in Vertical Tubes*, UKAEA Report, AAEW-R123, 1961.

[68] Wallis, G. B., *One-Dimensional Two-Phase Flow*, McGraw-Hill, 1969.

[69] Wang, M. J. and Mayinger, F., S*imulation and Analysis of Thermal-Hydraulic Phenomena in a PWR Hot Leg Related to SBLoca*, Nucl. Eng. and Design, Vol. 155, 1995, 643-652.

[70] Weiss, P. A. and Hertlein, R. J., *UPTF Test Results: First 3 Separate Effects Tests*, NUREG-CP-0082, Vol. 4, 1987.

[71] Wongwises, S., *Effect of Inclination Angles and Upper End Conditions on the Countercurrent Flow Limitation in Straight Circular Pipes*, Int. Comm. Heat Mass Transfer, Vol. 25, No. 1, 1998, 117-125.

[72] Wongwises, S., *Flooding in a Horizontal Pipe with Bend*, Int. J. Multiphase Flow, Vol. 22, No. 1, 1996, 195-201.

[73] Wongwises, S., *Two-Phase Countercurrent Flow in a Model of a Pressurized Water Reactor Hot Leg*, Nucl. Eng. and Design, Vol. 166, 1996, 121-133.

[74] Yih, C., *Stratified Flows*, Academic Pres Inc., 1980.

[75] Zapke, A. and Kröger, D. G., *The influence of Fluid Properties and Inlet Geometry on Flooding in Vertical and Inclined Tubes*, Int. J. Multiphase Flow, Vol. 22, No. 3, 1996, 461-472.

Nomenclature

Symbol	Units (I.S.)	Concept
$\dot{m}$	[kg/s]	Mass flow rate
$\dot{V}$	[m³/s]	Volumetric flow rate
a		Acceleration
A	[m²]	Flow cross sectional area
A_G	[m²]	Flow cross sectional area of the gas
A_L	[m²]	Flow cross sectional area of the liquid
A_0	[m²]	Flow cross sectional area at injection point
A_{TOT}	[m²]	Total flow cross sectional area
B	[m]	Surface Width of the waterway
b	[m]	Back flow ratio
C	[-]	Wallis constant
c	[m/s]	Celerity
C_C^*	[-]	Dimensionless condensation factor
$C_{P,crit}$	[-]	Geometric factor
C_f	[-]	Friction parameter
D	[m]	Diameter
D^*	[-]	Dimensionless diameter
d_H	[m]	Hydraulic diameter
d	[-]	Constant value (back flow ratio correlation)
dx	[-]	Differential of channel length
dy	[-]	Differential of liquid depth
F_a	[N]	Inertial force
F_g	[N]	Gravitational force
Fl_P*	[-]	Fluid properties ratio

Fr	[-]	Froude number
Fr_A	[-]	Local Froude number at liquid outlet
Fr_{A-A}	[-]	Local Froude number at section A-A
Fr_x	[-]	Local Froude number at position x
Fr_0	[-]	Local Froude number at liquid inlet
g	[m/s²]	Acceleration of gravity
H	[m]	Channel height
h	[m]	Local vertical position in channel
K^*	[-]	Dimensionless Kutateladze number
K_G^*	[-]	Dimensionless gas Kutateladze number
K_L^*	[-]	Dimensionless liquid Kutateladze number
ℓ	[m]	Channel length
ℓ_{CH}	[m]	Channel length, measured experimentally
M	[-]	Momentum ratio
m	[-]	Wallis constant for dimensionless superficial liquid velocity
m_F	[kg]	Fluid mass
n	[-]	Constant value
P_K	[Pa]	Pressure measurement at the test section entrance
P_{K0}	[Pa]	Pressure measurement downstream the air flow meter
ΔP_G	[Pa]	Pressure difference measured in the test section
p	[Pa]	Pressure
Q	[m³/s]	Channel total discharge
R_d	[-]	Ratio of Densities
R_{eq}	[m]	Equivalent radius
Re	[-]	Reynolds number
Re^*	[-]	Modified Reynolds number
Re_G	[-]	Gas Reynolds number

Re_L	[-]	Liquid Reynolds number
S_L	[m]	Wetted perimeter
s	[-]	Slip velocity ratio
T	[°C]	Temperature
T_L	[°C]	Liquid temperature
T_G	[°C]	Gas temperature at test section entrance
T_{G0}	[°C]	Gas temperature downstream air flow meter
t	[s], [ms]	time
u	[m/s]	Mean velocity
$u_{S,crit}$	[m/s]	Critical superficial velocity
u_S^*	[-]	Dimensionless superficial velocity
u_L	[m/s]	Mean liquid velocity
u_G	[m/s]	Mean gas velocity
u_{GA}	[m/s]	Mean gas velocity at liquid outlet
u_{LA}	[m/s]	Mean liquid velocity at liquid outlet
$u_{G,crit}$	[m/s]	Critical gas velocity
u_{LS}	[m/s]	Superficial liquid velocity
u_{GS}	[m/s]	Superficial gas velocity
$u_{LS,crit}$	[m/s]	Critical superficial liquid velocity
u_{LS}^*	[-]	Dimensionless superficial liquid velocity
u_{GS}^*	[-]	Dimensionless superficial gas velocity
$u_{GS,E}^*$	[-]	Dimensionless superficial gas velocity taking into account entrainment effects
$u_{GS,C}^*$	[-]	Critical dimensionless superficial gas velocity
$u_{G,crit}$	[m/s]	Critical gas velocity
$u_{G,IN}$	[m/s]	Gas velocity at the gas inlet section (equivalent to superficial gas velocity)
$u_{G,IN,min}$	[m/s]	Minimum gas velocity to set reversed flow
x	[m]	Horizontal Cartesian coordinate

y	[m]	Local liquid depth
y_A	[m]	Liquid depth at liquid outlet
$y_{A,C}$	[m]	Critical liquid depth at liquid outlet
y_C	[m]	Critical liquid depth
y_{eq}	[m]	Equivalent liquid depth
y_0	[m]	Inlet liquid depth
$y_{0,CH}$	[m]	Inlet liquid depth, measured experimentally
Z	[m]	Channel width
Z_L	[m]	Liquid properties parameter

Subscripts

A	Conditions at Liquid Outlet
A-A	Conditions at section A-A in the UPTF
a	Accelerational
B	As Calculated by Blasius
E	Entrainment conditions
L	Liquid
G	Gas
g	Gravitational
H	Hydraulic
0	Conditions at Liquid Inlet
UPTF	Conditions in the Upper Plenum Test Facility
WENKA	Conditions in the WENKA Test Facility
C	Critical Conditions
S	Superficial
W	Wall

i	Interface
*	Dimensionless parameter
eq	equivalent
K	Measurement in the channel
pred	Predicted by theory
exp	Experimental value
MEAN	Mean value
τ	Due to shear stress
theo	Theoretical value
min	Minimum value

Greek Symbols

Symbol	Units (I. S.)	Concept
ρ	[kg/m^3]	Density
τ	[N/m^2]	Shear Stress
δ	[m]	Typical length scale
η	[-]	Dimensionless Liquid Depth
λ	[-]	Fanning Friction Factor
ξ	[-]	Dimensionless Channel Height
ν	[m^2/s]	Kinematic Viscosity
σ	[N/m^2]	Surface tension
α_G	[-]	Void fraction
ϑ	[rad]	Ellbow inclination angle
$\theta/2$	[rad]	Contact angle of wetted perimeter
φ	[rad]	Horizontal pipe inclination angle
μ_L	[kg /(ms)]	Liquid dynamic viscosity
Δ	[-]	Increment

Acronyms

B&W	Babcock & Wilson
BWR	Boiling Water Reactor
CCD	Coupled Charged Device
CCFL	Countercurrent Flow Limitation
CFD	Computational Fluid Dynamics
ECC	Emergency Core Cooling
ECCS	Emergency Core Cooling System
HJ	Hydraulic Jump
HLC	Head Losses Characteristic line
IAEA	International Atomic Energy Agency
KWU	Kernkraftwerk Union
LB-LOCA	Large Break LOCA
LOCA	Loss of Coolant Accident
LWR	Light Water Reactor
LWR, LWRs	Light Water Reactor, Light Water Reactors
OPRF	Onset of Partially Reversed Flow
OTRF	Onset of Totally Reversed Flow
PIV	Particle Image Velocimetry
PRF	Partially Reversed Flow
PTS	Pressurized Thermal Shock
PWR	Pressurized Water Reactor
RPV	Reactor Pressure Vessel
RWZ	Rollover Wave Zone
SB	Subcritical
SB-LOCA	Small Break LOCA
SP	Supercritical

TRF	Totally Reversed Flow
UPTF	Upper Plenum Test Facility
UPTF	Upper Plenum Test Facility
WENKA	Wasser und Entrainment Kanal (Water and Entrainment Channel)
WDZ	Wave Destruction Zone
WF	Wave Front
WGZ	Wave Growing Zone

Tables

y_0 (mm)	$\dot{m}_L$ (kg/s)	$\dot{V}_L$ (l/min)	u_{L0} (m/s)	Fr_0
7	0.108	6.46	0.12	0.44
	0.250	15.03	0.28	1.02
	0.344	20.68	0.39	1.40
	0.523	31.39	0.59	2.12
	0.659	39.55	0.75	2.73
	1.055	63.38	1.20	4.28
	1.403	84.27	1.60	5.70
9	0.135	8.64	0.12	0.39
	0.267	16.07	0.24	0.78
	0.341	20.53	0.31	0.99
	0.414	24.84	0.38	1.20
	0.508	30.06	0.46	1.48
	0.582	35.09	0.53	1.69
	0.754	45.07	0.69	2.19
	0.920	55.52	0.84	2.67
11	0.249	14.98	0.19	0.55
	0.326	19.56	0.25	0.72
	0.416	24.97	0.32	0.92
	0.690	41.45	0.52	1.53
	0.872	52.39	0.66	1.93
	1.046	62.83	0.79	2.31
	1.140	68.49	0.86	2.52
15	1.254	22.787	1.43	5.09
	0.380	36.996	0.21	0.54
	0.616	53.98	0.35	0.88
	0.899	74.236	0.51	1.29
	1.236	100.418	0.71	1.77
	1.672	123.532	0.95	2.40

Table 7. Flow conditions investigated in the WENKA test facility to determine flow regime maps.

Facility	**y_0 (mm)**	**Cross Section (mm^2)**	**$\dot{V}_L$ (m^3/s)**	**$\dot{V}_G$ (m^3/s)**	**u_{L0} (m/s)**	**Fr_0**	**u_{G0} (m/s)**	**Re_L**	**Re_G**	**y_0 / D**
WENKA	3 ÷ 15	90 x 110	$3\cdot10^{-4}$ ÷ $3\cdot10^{-2}$	0.02 ÷ 0.2	0.1 ÷ 10.0	0.5 ÷ 40	2.0 ÷ 18.0	$2\cdot10^{2}$ ÷ $3\cdot10^{4}$	10^{4} ÷ 10^{5}	0.022 ÷ 0.167
Prototypic	103	0.478	3.7 ÷ 15	0.162 ÷ 0.432	4.4 ÷ 11.8	5.3 ÷ 14.2	8.4 ÷ 33.7	$4\cdot10^{6}$ ÷ $1\cdot10^{7}$	10^{5} ÷ $4\cdot10^{6}$	0.137

Table 8. Comparison of flow conditions present in a LOCA scenario with ECC hot leg injection and flow conditions investigated in the WENKA test facility.

y_0 (mm)	Fr_0	u_{L0} (m/s)	u_{G0} (m/s)	u_{GA} (m/s)	Fr_A	$y_{C,A}$ (m)	u_{LS} (m/s)	u_{GS} (m/s)	s	y_A theo Eq. (3.27)	y_A exp
3	8.8	1.5	12.3	13.8	1.0	13	0.05	11.9	37.8	12.8	12.5
	4.2	0.7	4.2	4.4	1.5	8	0.02	4.1	12.1	6.7	6.0
	5.4	0.9	7.4	7.7	1.6	9	0.03	7.1	18.8	6.2	6.8
7	2.7	0.7	8.7	9.4	1.1	13	0.05	8.0	24.9	13.5	13.0
	2.6	0.7	3.8	3.9	1.6	13	0.04	3.5	7.8	9.6	9.5
	3.0	0.8	6.6	6.8	1.9	15	0.05	6.1	11.7	9.5	9.5
	2.5	0.7	0.0	0.0	2.0	13	0.05	0.0	0.0	9.0	8.0
	3.6	1.0	6.6	6.8	2.5	7	0.06	6.1	9.1	9.1	9.0
9	1.9	0.6	6.8	7.1	1.1	14	0.06	6.1	18.6	13.6	13.0
	1.6	0.5	0.0	0.0	1.2	13	0.05	0.0	0.0	12.5	11.0
	2.3	0.7	5.6	5.7	1.7	16	0.07	5.0	10.3	11.8	11.0
	2.3	0.7	0.0	0.0	2.0	16	0.07	0.0	0.0	11.0	10.0
	2.7	0.8	5.6	5.7	2.3	17	0.08	5.0	8.0	9.5	10.0
11	1.8	0.6	7.5	8.0	1.0	16	0.07	6.6	19.6	16.4	16.0
	1.7	0.5	4.5	4.7	1.1	15	0.07	3.9	11.4	15.4	14.5
	1.7	0.6	5.8	6.0	1.1	16	0.07	5.1	14.0	15.9	14.5
	1.8	0.6	4.5	4.6	1.3	17	0.07	3.9	9.7	14.9	14.0
	2.0	0.6	4.5	4.6	1.4	17	0.08	3.9	9.1	14.3	14.0
	1.9	0.6	0.0	0.0	1.5	17	0.08	0.0	0.0	13.4	13.0
	2.3	0.8	7.6	7.8	1.7	19	0.09	6.7	12.7	14.4	13.5
15	2.3	0.9	8.7	9.0	1.7	26	0.15	7.2	12.4	18.2	18.0
	2.0	0.8	0.0	0.0	1.7	24	0.13	0.0	0.0	16.7	17.0
	1.9	0.7	0.0	0.0	1.5	23	0.12	0.0	0.0	17.2	17.5
	1.8	0.7	6.5	6.8	1.4	23	0.12	5.4	11.5	18.6	18.0
	2.0	0.8	8.7	9.3	1.3	23	0.13	7.2	16.5	19.9	20.0
	1.7	0.7	6.5	6.9	1.3	22	0.11	5.4	12.8	20.4	18.5
	1.6	0.6	0.0	0.0	1.2	21	0.10	0.0	0.0	18.0	18.0

Table 9. Prediction of liquid depth at the end of the test section and comparison with experimental values for supercritical flow.

$\dot{V}_G$ (l/s)	$\dot{V}_L$ (l/min)	y_A (mm)	u_{L0} (m/s)	u_{LA} (m/s)	u_{G0} (m/s)	u_{GA} (m/s)	Fr_0	Fr_A	$y_{A,C}$ (mm)	Flow Regime	u_{LS} (m/s)	u_{GS} (m/s)
49.9	46.8	10.0	0.79	0.71	5.6	5.7	2.6	2.27	17.3	SP	0.079	5.0
49.9	40.7	11.0	0.68	0.56	5.6	5.7	2.3	1.70	15.7	SP	0.068	5.0
49.9	37.3	11.0	0.63	0.51	5.6	5.7	2.1	1.57	14.8	SP	0.063	5.0
49.9	34.4	11.5	0.58	0.45	5.6	5.8	1.9	1.35	14.0	SP	0.058	5.0
49.9	32.0	13.0	0.54	0.37	5.6	5.9	1.8	1.04	13.4	SP → HJ (Point A)	0.054	5.0
49.9	32.0 to 18.0	Not measured	0.54 to 0.30	Not measured	5.6	Not measured	1.8 to 1.0	Not measured	Not measured	HJ	0.054 to 0.030	5.0
50	18	Not measured	0.30	Not measured	5.6	Not measured	1.0	Not measured	9.1	HJ → SB (Point B)	0.030	5.0

Table 10. Intermediate stages for the transition SP→ Point A→ Point B (See Fig. 4.5)

V_{mean} (m/s)		0.00	5.66	8.02	10.04	12.04	14.05	16.08	18.00
Q (l/s)		0.00	56.00	79.43	99.44	119.18	139.06	159.20	178.23
Reynolds		0.0E+00	3.6E+04	5.1E+04	6.3E+04	7.6E+04	8.9E+04	1.0E+05	1.1E+05
h (mm)	0.00	0.00	0.00	0.00	0.00	0.00	0.00	0.00	0.00
	5.71	0.16	4.41	6.53	0.20	1.09	0.08	0.10	0.02
	10.29	0.22	5.42	7.53	8.96	10.09	0.90	0.70	0.66
	14.86	0.25	5.66	7.96	9.64	12.16	5.42	3.15	1.22
	19.43	0.30	5.81	8.49	10.42	12.76	14.78	13.65	9.14
	24	0.32	6.04	8.89	10.89	13.54	15.93	17.63	18.38
	28.57	0.35	6.24	9.27	11.33	13.99	16.46	18.21	20.19
	33.14	0.38	6.71	9.73	11.66	14.17	16.88	18.93	21.38
	37.71	0.40	6.93	10.12	11.88	14.43	17.05	19.38	21.82
	42.29	0.42	6.87	10.32	11.87	14.38	17.06	19.51	21.96
	46.86	0.43	7.04	10.50	11.95	14.44	16.98	19.51	21.89
	51.43	0.42	6.99	10.31	11.95	14.37	16.94	19.21	21.80
	55.99	0.41	6.75	9.89	11.86	14.28	16.69	19.05	21.36
	60.57	0.39	6.54	9.61	11.67	14.18	16.45	18.93	21.09
	65.14	0.37	6.20	9.24	11.56	13.80	15.88	18.31	20.35
	69.71	0.34	5.98	8.80	11.29	13.19	14.99	17.49	19.41
	74.29	0.30	5.80	8.42	10.86	12.22	14.23	16.70	18.67
	78.86	0.26	5.69	8.12	9.94	11.62	13.45	15.89	17.29
	83.43	0.22	5.44	7.56	8.98	10.92	12.34	14.60	13.60
	87.99	0.09	0.00	6.51	6.17	0.50	5.81	4.76	3.15
	90	0.00	0.00	0.00	0.00	0.00	0.00	0.00	0.00
u_{mean} (m/s) PIV		0.29	5.82	7.99	10.16	11.90	13.07	14.51	15.44

Table 11. Air velocities obtained with PIV.

y_0 (mm)	$\dot{V}_G$ (l/s)	$\dot{V}_L$ (l/min)	Fr_0	Fr_A	u_{L0} (m/s)	u_{LA} (m/s)	u_{G0} (m/s)	u_{GA} (m/s)	y_A (mm)	$y_{A,C}$ (mm)	s	Re_{G0}
3	0.0	11.1	3.25	0.95	0.56	0.25	0.00	0.00	6.8	6.6	0.0	0.0
	35.3	12.3	3.62	1.01	0.62	0.27	3.68	3.86	7.0	7.1	14.5	23509
	40.5	12.4	3.64	1.02	0.63	0.27	4.23	4.44	7.0	7.1	16.6	27012
	50.7	12.5	3.67	1.03	0.63	0.27	5.30	5.55	7.0	7.1	20.6	33795
	57.6	12.8	3.77	1.01	0.65	0.27	6.02	6.33	7.2	7.3	23.5	38407
	62.0	13.7	4.04	1.02	0.69	0.28	6.48	6.83	7.5	7.6	24.7	41350
	70.5	14.2	4.17	1.12	0.72	0.30	7.36	7.74	7.2	7.8	25.9	46982
4	0.0	13.4	2.56	0.90	0.51	0.25	0.00	0.00	8.0	7.5	0.0	0.0
	53.8	15.8	3.03	1.07	0.60	0.30	5.69	5.97	8.0	8.4	19.9	35873
	64.4	16.1	3.08	1.09	0.61	0.31	6.81	7.14	8.0	8.5	23.4	42927
	68.2	16.9	3.24	0.96	0.64	0.28	7.21	7.66	9.0	8.8	26.9	45483
7	0.0	21.3	1.76	1.03	0.46	0.32	0.00	0.00	10.0	10.2	0.0	0.0
	38.2	22.6	1.86	1.09	0.49	0.34	4.19	4.35	10.0	10.6	12.7	25496
	60.1	25.6	2.12	1.07	0.55	0.35	6.58	6.92	11.0	11.5	19.6	40077
	51.9	25.7	2.12	1.08	0.56	0.35	5.68	5.97	11.0	11.5	16.9	34601
	69.7	26.3	2.17	1.03	0.57	0.35	7.63	8.07	11.5	11.7	23.3	46434
9	0.0	26.9	1.52	0.99	0.45	0.34	0.00	0.00	12.0	11.9	0.0	0.0
	38.8	28.8	1.63	1.06	0.49	0.36	4.35	4.52	12.0	12.5	12.4	25867
	49.9	32.0	1.81	1.04	0.54	0.37	5.60	5.89	13.0	13.4	15.8	33281
11	0.0	37.2	1.56	1.09	0.51	0.40	0.00	0.00	14.0	14.8	0.0	0.0
	38.9	39.0	1.64	1.08	0.54	0.41	4.47	4.68	14.5	15.3	11.5	25905
	50.2	39.2	1.64	1.03	0.54	0.40	5.78	6.09	15.0	15.3	15.4	33469
	54.2	39.5	1.66	1.04	0.54	0.40	6.24	6.57	15.0	15.4	16.5	36161
	65.4	41.9	1.76	0.91	0.58	0.37	7.53	8.15	17.0	16.0	21.8	43617
15	0.0	53.4	1.41	0.99	0.54	0.43	0.00	0.00	19.0	18.8	0.0	0.0
	37.6	55.6	1.46	1.07	0.56	0.46	4.56	4.78	18.5	19.3	10.5	25053
	53.9	56.2	1.48	0.96	0.57	0.43	6.54	7.00	20.0	19.5	16.5	35959

Table 12. Occurrence of a hydraulic jump at the end of the test section with an initial super-critical flow.

y_0 (mm)	$\dot{V}_G$ (l/s)	$\dot{V}_L$ (l/min)	Fr_0	u_{G0} (m/s)	u_{GA} (m/s)	y_A (mm)	u_{L0} (m/s)	u_{LA} (m/s)	l/y_0 Exp	l/y_0 Stagnant	l/y_0 Blasius	l/y_0 Kim
4	0.0	14.0	2.7	0.0	0.00	8	0.53	0.27	117.5	116.1	115.8	116.0
4	64.4	16.1	3.0	6.5	7.14	8	0.61	0.31	117.5	153.2	136.7	102.7
8	0.0	29.0	1.9	0.0	0.00	13	0.55	0.34	58.8	67.8	67.6	67.7
8	65.0	29.9	2.0	6.6	7.68	13	0.57	0.35	58.8	73.7	65.6	48.2
8	84.4	35.3	2.4	8.5	10.09	14	0.67	0.38	58.8	113.8	97.0	63.4
12	0.0	45.4	1.6	0.0	0.00	17	0.57	0.40	39.2	44.6	44.4	44.5
12	65.2	46.0	1.7	6.6	8.35	19	0.58	0.37	39.2	47.2	41.2	28.7
12	79.2	56.9	2.0	8.0	10.59	22	0.72	0.39	39.2	93.7	77.9	47.4

Table 13. Experimental data employed in Fig. 4.7.

Q_L (l/min)		20	60	100	140	180	200
y_0/H	**y_0(mm)**	**Re_{L0}**					
0.022	2	1.7E+02	6.6E+03	1.3E+04	2.0E+04	2.6E+04	3.0E+04
0.044	4	1.6E+02	6.5E+03	1.3E+04	1.9E+04	2.6E+04	2.9E+04
0.067	6	1.6E+02	6.4E+03	1.3E+04	1.9E+04	2.6E+04	2.9E+04
0.089	8	1.6E+02	6.3E+03	1.3E+04	1.9E+04	2.5E+04	2.8E+04
0.111	10	1.5E+02	6.2E+03	1.2E+04	1.9E+04	2.5E+04	2.8E+04
0.133	12	1.5E+02	6.1E+03	1.2E+04	1.8E+04	2.4E+04	2.7E+04
0.156	14	1.5E+02	6.0E+03	1.2E+04	1.8E+04	2.4E+04	2.7E+04
0.178	16	1.5E+02	5.9E+03	1.2E+04	1.8E+04	2.4E+04	2.6E+04
0.200	18	1.4E+02	5.8E+03	1.2E+04	1.7E+04	2.3E+04	2.6E+04
0.222	20	1.4E+02	5.7E+03	1.1E+04	1.7E+04	2.3E+04	2.6E+04

Table 14. Liquid Reynolds numbers in WENKA.

		Q_L (l/min)									
		20	40	60	80	100	120	140	160	180	200
y_0/H	**y_0(mm)**	**Fr_0**									
0.022	2	***10.8***	***21.6***	***32.5***	43.3	54.1	64.9	75.7	86.5	97.4	108.2
0.044	4	3.8	***7.6***	***11.5***	***15.3***	***19.1***	***22.9***	26.8	30.6	34.4	38.2
0.067	6	2.1	4.2	***6.2***	***8.3***	***10.4***	***12.5***	***14.6***	***16.7***	***18.7***	***20.8***
0.089	8	1.4	2.7	4.1	***5.4***	***6.8***	***8.1***	***9.5***	***10.8***	***12.2***	***13.5***
0.111	10	1.0	1.9	2.9	3.9	4.8	***5.8***	***6.8***	***7.7***	***8.7***	***9.7***
0.133	12	0.7	1.5	2.2	2.9	3.7	4.4	***5.2***	***5.9***	***6.6***	***7.4***
0.156	14	0.6	1.2	1.8	2.3	2.9	3.5	4.1	4.7	***5.3***	***5.8***
0.178	16	0.5	1.0	1.4	1.9	2.4	2.9	3.3	3.8	4.3	4.8
0.200	18	0.4	0.8	1.2	1.6	2.0	2.4	2.8	3.2	3.6	4.0
0.222	20	0.3	0.7	1.0	1.4	1.7	2.1	2.4	2.7	3.1	3.4

Table 15. Froude numbers in the WENKA test facility.

u_{GS}(m/s)	**u_{L0}(m/s)**	$\sqrt{2}(u_{GS}/u_{L0})_{UPTF}$
8.4	11.82	1
8.4	4.43	2.7
33.7	11.82	4
33.7	4.43	10.7

Table 16. UPTF -velocity ratios for comparison with WENKA.

		u_{GS}(m/s)								
		5.05	7.07	9.09	11.11	13.13	15.15	17.17	19.19	20.20
y/H	0.133	**Q_G(l/s)**								
y_0(mm)	12.5	50	70	90	110	130	150	170	190	200
Q_L (l/min)	**u_{L0} (m/s)**	**$(u_{GS}/u_{L0})_{WENKA}$**								
0.5	0.01	800.0	1120.0	1440.0	1760.0	2080.0	2400.0	2720.0	3040.0	3200.0
10	0.13	40.0	56.0	72.0	88.0	104.0	120.0	136.0	152.0	160.0
20	0.25	20.0	28.0	36.0	44.0	52.0	60.0	68.0	76.0	80.0
40	0.51	**10.0**	14.0	18.0	22.0	26.0	30.0	34.0	38.0	40.0
60	0.76	**6.7**	**9.3**	12.0	14.7	17.3	20.0	22.7	25.3	26.7
80	1.01	**5.0**	**7.0**	**9.0**	11.0	13.0	15.0	17.0	19.0	20.0
100	1.26	**4.0**	**5.6**	**7.2**	**8.8**	**10.4**	12.0	13.6	15.2	16.0
120	1.52	**3.3**	**4.7**	**6.0**	**7.3**	**8.7**	**10.0**	11.3	12.7	13.3
140	1.77	**2.9**	**4.0**	**5.1**	**6.3**	**7.4**	**8.6**	**9.7**	10.9	11.4
160	2.02	**2.5**	**3.5**	**4.5**	**5.5**	**6.5**	**7.5**	**8.5**	**9.5**	**10.0**
180	2.27	**2.2**	**3.1**	**4.0**	**4.9**	**5.8**	**6.7**	**7.6**	**8.4**	**8.9**
200	2.53	**2.0**	**2.8**	**3.6**	**4.4**	**5.2**	**6.0**	**6.8**	**7.6**	**8.0**

Table 17. Velocity ratio in the WENKA experiments for a liquid height of 12.5 mm at the inlet.